Mineralogical, Textural, and Metal Residence Studies of Primary, Recrystallized, and Remobilized Ores of the Greens Creek Deposit

By Cliff D. Taylor, Steven J. Sutley, and Frederick E. Lichte

Chapter 9 of
Geology, Geochemistry, and Genesis of the Greens Creek Massive Sulfide Deposit, Admiralty Island, Southeastern Alaska
Edited by Cliff D. Taylor and Craig A. Johnson

Professional Paper 1763

U.S. Department of the Interior
U.S. Geological Survey

Contents

Figures

Tables

Mineralogical, Textural, and Metal Residence Studies of Primary, Recrystallized, and Remobilized Ores of the Greens Creek Deposit

By Cliff D. Taylor, Steven J. Sutley, and Frederick E. Lichte

Abstract

The Greens Creek deposit is a 24.2-million-ton polymetallic massive sulfide with a diverse base- and precious-metal-rich mineralogy, which has been subjected to regional lower greenschist facies metamorphism. Roughly 30 percent of the ores retain primary mineralogy and mineral textures as well as gross original ore stratigraphy. Ore lithologies fall into two groups: massive sulfide ores (greater than 50 percent sulfides) and semimassive or disseminated sulfide gangue-rich "white" ores (less than 50 percent sulfides). There are two types of massive ore: massive pyritic and massive base-metal-rich ore. The white ores are of three types: white carbonate and white siliceous ores (common), and white baritic ore. All the ore types can be further subdivided on the basis of modification by veins, breccias, and gouge or rubble zones produced during faulting or folding. Veining due to metamorphic remobilization and recrystallization can result in enrichment of free gold and a variety of silver-sulfosalt minerals. The ore stratigraphy at Greens Creek is characterized by proximal copper-arsenic-gold-enriched massive pyritic ores centered over white siliceous ores and silicified footwall. Laterally, the white siliceous ores grade outward into white carbonate and barite ores. White ores are overlain by massive pyritic ores that change upward and outward toward lower copper-gold grades. Proximal ores transition to increasingly higher grade zinc-lead-silver-(gold)-rich, massive, fine-grained, base-metal-rich ores toward the argillite hanging wall and the margins of the deposit. Distal ore commonly is characterized by carbonate- and barite-rich white ores against footwall phyllites, which grade into massive, fine-grained, base-metal-rich ores toward the hanging wall. This progression of ore types is the most common throughout the mine.

Primary mineral textures are characterized by framboidal, colloform, dendritic, and "spongy" pyrite intergrown with base-metal sulfides and sulfosalts. Primary assemblages also include sphalerite, galena, tetrahedrite, chalcopyrite, free gold, and a variety of lead-antimony-arsenic (-mercury-thallium) sulfosalts. The abundance of polyframboidal, colloform, and nodular pyrite textures coupled with their $\delta^{34}S$-depleted isotopic signature provides strong evidence that the main stage of massive sulfide mineralization at Greens Creek occurred primarily during early diagenesis, synchronous with accumulation of the hanging-wall sediments. The early development of framboid-derived, atoll-shaped textures in the ores may indicate that a zone-refinement process occurred in the presence of colloidal base-metal-sulfide gels. Metamorphic recrystallization produced advanced atoll-shaped structures in the ores and resulted in much coarser textures and the formation and(or) remobilization of secondary, precious-metal-enriched minerals. Secondary minerals are present as matrix to pyrite euhedra and in late fractures and veinlets. Secondary mineralogy includes chalcopyrite, sphalerite (low iron), galena, free gold, electrum, tetrahedrite (antimony-rich), pyrargyrite, and many other sulfosalt minerals. Metamorphism resulted in visible cleaning and coarsening of the ore mineralogy and caused local trace-element redistribution and upgrading of the ores.

Introduction

The Greens Creek deposit is a mineralogically diverse, polymetallic (zinc-lead-silver-gold-copper) massive sulfide of Late Triassic age and unusually high silver content. The global resource is currently 24.2 million tons at an average grade of 13.9 percent zinc, 5.1 percent lead, 0.15 troy ounces per ton gold, and 19.2 troy ounces per ton silver. Twenty-nine ore sulfide minerals have been reported, 18 of which are silver bearing (table 1). In addition to the metals of economic interest, the ores are enriched in trace elements such as As, Sb, Hg, Tl, Ni, Co, Cr, and Mo. These metals and minerals are contained in a suite of five ore types, which define an ore stratigraphy that progressed from early white ores to main-stage massive sulfide ores during the growth of the system. This progression (see chap. 15 for a more thorough description) is thought to have started at low temperature, at or very near the sediment/water interface in a basin containing oxygenated seawater, and then evolved to higher temperature within a growing sulfide blanket that formed in and beneath a progressively thickening layer of black shales. As deposition progressed, pore fluids in the shales and probably the overlying water column gradually became anoxic. These early and main-stage ore-forming

Table 1. Greens Creek ore mineralogy—minerals identified.

Mineral name	Mineral formula	How identified	Reference
silver	Ag	XRD, LA--ICP--MS	this study
acanthite	Ag_2S	electron microprobe, XRD	C.J. Carter (written commun., 1994)
proustite	Ag_3AsS_3	optical microscope, XRD, electron microprobe	this study
jalpaite	Ag_3CuS_2	electron microprobe	C.J. Carter (written commun., 1994); T.K. Bundtzen (written commun., 1996)
pyrargyrite	Ag_3SbS_3	optical microscope, electron microprobe	T.C. Crafford (written commun., 1989)
stephanite	Ag_5SbS_4	electron microprobe	T.C. Crafford (written commun., 1989)
argyrodite	Ag_8GeS_6	electron microprobe	K.G. Lear (oral commun., 2000)
stromeyerite	AgCuS	electron microprobe	E.U. Peterson (written commun., 1991)
realgar	AsS	optical microscope, XRD	this study
pearceite	$(Ag,Cu)_{16}As_2S_{11}$	electron microprobe	E.U. Peterson (written commun., 1991)
antimonpearceite	$(Ag,Cu)_{16}Sb_2S_{11}$	optical microscope, XRD, electron microprobe	K.G. Lear (oral commun., 2000)
polybasite	$(Ag,Cu)_{16}Sb_2S_{11}$	electron microprobe	T.C. Crafford (written commun., 1989)
mckinstryite	$(Ag,Cu)_2S$	electron microprobe	E.U. Peterson and D. Chirban (written commun., 1994)
freibergite	$(Ag,Cu,Fe)_{12}(Sb,As)_4S_{13}$	optical microscope, electron microprobe	T.C. Crafford (written commun., 1989)
gold	Au,(Ag)	optical microscope, LA–ICP–MS	T.C. Crafford (written commun., 1989); this study
electrum	Au,Ag,(Hg)	optical microscope, LA–ICP–MS	T.C. Crafford (written commun., 1989); E.U. Peterson (written commun., 1991); this study
chalcocite - Ag-bearing	Cu_2S +Ag	electron microprobe	E.U. Peterson (written commun., 1991)
bornite	Cu_5FeS_4	optical microscope	E.U. Peterson (written commun., 1991)
bornite - Ag-bearing	Cu_5FeS_4 +Ag	electron microprobe	E.U. Peterson (written commun., 1991)
chalcopyrite	$CuFeS_2$	optical microscope	T.C. Crafford (written commun., 1989); E.U. Peterson (written commun., 1991)
tennantite	$(Cu,Fe)_{12}As_4S_{13}$	optical microscope, XRD, electron microprobe	this study
tetrahedrite	$(Cu,Fe)_{12}Sb_4S_{13}$	optical microscope, electron microprobe, XRD	T.C. Crafford (written commun., 1989); E.U. Peterson (written commun., 1991)
covellite	CuS	optical microscope	E.U. Peterson (written commun., 1991)
covellite-acanthite mineral	CuS-Ag_2S	electron microprobe	E.U. Peterson (written commun., 1991)
unknown (possibly thalcusite)	CuTlS ($Tl_2(Cu,Fe)_4S_4$)	electron microprobe	K.G. Lear (oral commun., 2000)
arsenopyrite	FeAsS	electron microprobe, XRD	C.J. Carter (written commun., 1994)
marcasite	FeS_2	optical microscope	C.J. Carter (written commun., 1994)
pyrite	FeS_2	optical microscope	T.C. Crafford (written commun., 1989); E.U. Peterson (written commun., 1991)
geocronite	$Pb_{14}(As,Sb)_6S_{23}$	electron microprobe	K.G. Lear (oral commun., 2000)
jordanite	$Pb_{14}(As,Sb)_6S_{23}$	optical microscope, XRD, electron microprobe	this study
boulangerite	$Pb_5Sb_4S_{11}$	electron microprobe	K.G. Lear (oral commun., 2000)
galena	PbS	optical microscope	T.C. Crafford (written commun., 1989); E.U. Peterson (written commun., 1991)
cassiterite	SnO_2	electron microprobe	K.G. Lear (oral commun., 2000)
sphalerite	ZnS	optical microscope	T.C. Crafford (written commun., 1989); E.U. Peterson (written commun., 1991)

Spelling of mineral names and mineral formulas follows the usage of Blackburn and Dennen, 1997.

KGCMC, Kennecott Greens Creek Mining Company; XRD, X-ray diffraction; LA–ICP–MS, laser ablation–inductively coupled plasma–mass spectrometry.

processes produced a trace-element-rich orebody with a diverse silver- and base-metal-rich mineralogy, primarily by replacement of shale, early sulfides, and silica-barite gangue. Remnants of primary mineral textures are represented by fine- to very fine grained aggregates of framboidal, dendritic, and colloform or botryoidal pyrite intimately intergrown and banded with base-metal sulfides and the diverse suite of trace-element and silver-bearing sulfides.

Following the cessation of mineral deposition in latest Triassic time, the deposit was buried by continued shale sedimentation, which effectively prevented sea-floor oxidation of the newly formed sulfides. During the next 215 million years the deposit went through at least three phases of deformation (see chap. 7) and a regional subgreenschist to lower greenschist facies metamorphic event (see chap. 2) that reached temperatures of 275–350°C (see chap. 12) and buried host rocks in the Greens Creek area to a depth of about 17–18 kilometers (Himmelberg and others, 1995). Although the metamorphism and multiple deformation of the orebody resulted in pronounced structural dismemberment, folding, recrystallization, and remobilization of the ores, large areas of the deposit preserve primary mineralogy, textures, and chemistry. A range of preservation states exists, from pristine to completely modified. This fortuitous situation presents an opportunity to study the effects of deformation and metamorphism upon massive sulfide mineral textures and to understand the details of mineral residence of specific trace elements and their redistribution as a result of textural modification.

Most of the initial mineral identifications, descriptions of ore textures, and preliminary determinations of mineral chemistry are contained in unpublished mining company reports (see "Previous Mineralogical and Mineral Geochemical Studies" section). In particular, electron microprobe mineral-chemistry studies were conducted to improve the beneficiation of various mill products, and metal zonation studies of tetrahedrites were conducted in an attempt to obtain geochemical vectors within ore assemblages. We summarize these unpublished reports, compile their mineral identifications and textural observations, and significantly extend the petrographic descriptions and geochemistry of the various ores at Greens Creek.

Here we describe the five principal ore types in detail and the mineralogy and mineral textures present in these ores. We then discuss the paragenesis of the ores and the progressive modification of the mineralogy and mineral textures as a result of deformation and metamorphism. We follow the descriptive portion of the chapter with the presentation of preliminary Laser Ablation–Inductively Coupled Plasma–Mass Spectroscopy (LA–ICP–MS) mineral geochemical studies of the ores. The LA–ICP–MS studies provide mineral-specific geochemical data in support of the petrographic observations. These data demonstrate that the specific mineral residence and concentrations of trace elements in the ores change as a result of recrystallization and remobilization, in addition to the resulting mineralogical and textural modifications. Based on the petrographic observations and mineral chemistry presented, we propose a sequence of events that explain the formation and modification of the mineralogy, textures, metal endowments, and zonation of the ores throughout the deposit. The chapter concludes with a discussion of the mobility of metals in deformed massive sulfide deposits and a comparison of Greens Creek mineralogy and chemistry to modern and ancient analogs.

Mine Location, General Host Rocks, Metamorphic History, Deposit Morphology, and Structural History

The Greens Creek mine is 29 km south of Juneau, Alaska, near the northern end of Admiralty Island and within Admiralty Island National Monument (fig. 1). The deposit is located at the contact between a footwall sequence of predominantly phyllitic mafic volcanic rocks and mafic-ultramafic hypabyssal sills and intrusions, and a hanging wall of black argillites. Geochronologic studies (chap. 11) have established that the hanging-wall argillites have an age of 220 Ma and are thus part of the sedimentary portion of the regionally extensive Hyd Group of latest Triassic (Norian) age. Less precise age controls suggest strongly that the mafic-ultramafic intrusive suite in the footwall is also of Late Triassic age and are the parent rocks to the Hyd Group basalts that cap the argillites. Uncertainty remains as to the age and identity of the footwall phyllites. They are most likely either of middle Permian or of Late Triassic age.

Constraints on the metamorphic history of the host rocks and ore at Greens Creek are few. The Late Triassic and older rocks of most of Admiralty Island are within the Admiralty Island Metamorphic Belt of Brew and others (1992), which refers to most of the island west of the Glass Peninsula. Within this region, mineral assemblage data are limited, no isograds have been mapped, and no thermobarometric data are available. No clear trends in the metamorphic pattern are discernible, and rocks from subgreenschist through amphibolite facies are present, produced during post-Triassic metamorphism and deformation (Brew and others, 1992). Loney (1964) suggested there is a westward decrease in metamorphic grade present in correlative rocks on the southern portion of Admiralty Island. Regional mapping of metamorphic units (Dusel-Bacon, 1994) places the Admiralty Island Metamorphic Belt in the greenschist facies; descriptions of Late Triassic and younger rock units within this belt in the area around the mine (Lathram and others, 1965; S.M. Karl, written commun., 2003) suggest subgreenschist to lower greenschist facies metamorphic grade. Limited petrographic and electron microprobe work conducted during this study on Hyd Group basalt samples from the immediate vicinity of the mine suggest a dominantly chlorite-albite-epidote-quartz-sericite-calcite assemblage with occasional relict clinopyroxene and(or) hornblende phenocrysts. Tentative petrographic and electron microprobe identification of minor pumpellyite may indicate that the Late Triassic and younger rocks of the mine area are near the prehnite-pumpellyite to lower greenschist facies transition.

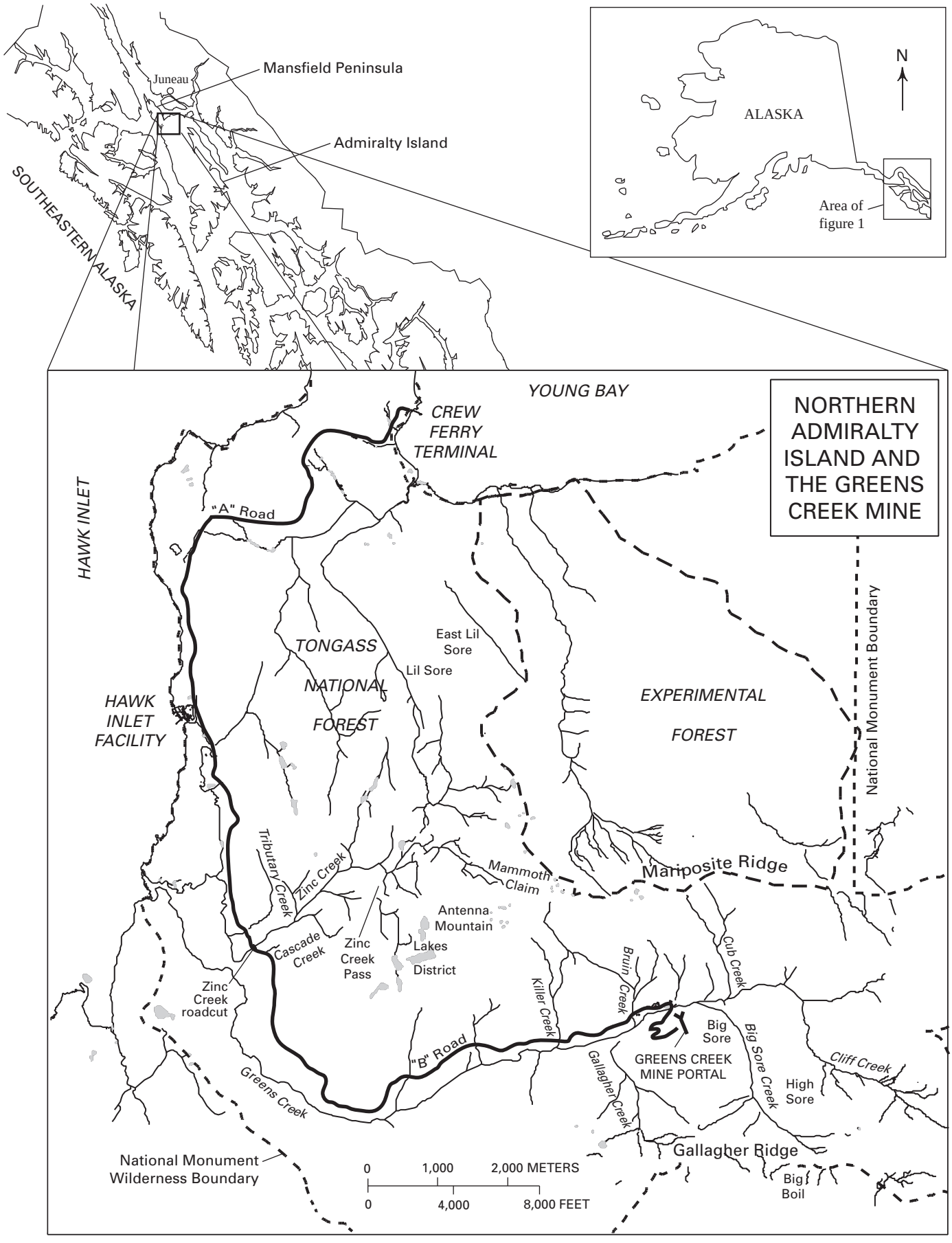
Juneau
Mansfield Peninsula
Admiralty Island
SOUTHEASTERN ALASKA
N
ALASKA
Area of figure 1
NORTHERN ADMIRALTY ISLAND AND THE GREENS CREEK MINE
YOUNG BAY
CREW FERRY TERMINAL
HAWK INLET
"A" Road
HAWK INLET FACILITY
TONGASS NATIONAL FOREST
East Lil Sore
Lil Sore
EXPERIMENTAL FOREST
National Monument Boundary
Tributary Creek
Zinc Creek
Mammoth Claim
Mariposite Ridge
Antenna Mountain
Cascade Creek
Zinc Creek Pass
Lakes District
Zinc Creek roadcut
Killer Creek
Bruin Creek
Cub Creek
Big Sore
GREENS CREEK MINE PORTAL
"B" Road
Gallagher Creek
Big Sore Creek
Cliff Creek
High Sore
Greens Creek
Gallagher Ridge
Big Boil
National Monument Wilderness Boundary
0 1,000 2,000 METERS
0 4,000 8,000 FEET

Figure 1 (facing page). Maps of northern Admiralty Island showing the location of the Greens Creek mine and other features mentioned in the text.

In general, the metamorphic history of Permian and younger rocks in the mine area is thought to be similar to the better-studied western metamorphic belt, the western edge of which is located several kilometers northeast of the mine. The western metamorphic belt is part of the Coast plutonic-metamorphic complex (Brew and others, 1989) of western Canada and southeastern Alaska that developed during the collision of the Alexander terrane and Gravina overlap assemblage with the Stikine terrane (Brew and others, 1989, 1992; Himmelberg and others, 1994, 1995). The western metamorphic belt is about 30 kilometers wide in the vicinity of Juneau and is characterized by Barrovian metamorphism. Multiple periods of deformation, metamorphism, and plutonism occurred from about 120 to 50 Ma, with the earliest, a regional dynamothermal event termed M_1, constrained by fabrics that predate intrusion of 110-Ma mafic-ultramafic rocks (Brew and others, 1989, 1992; Himmelberg and others, 1994, 1995). Himmelberg and others (1995) conducted a mineral chemistry and phase equilibria study of the M_1 event in subgreenschist to lower greenschist facies Douglas Island volcanics along the western edge of the western metamorphic belt. They concluded that thermal peak metamorphism of pumpellyite-bearing assemblages occurred at about 325°C and 2 to 4.8 kbar, equal to a maximum burial depth, assuming a normal geothermal gradient, of about 17–18 kilometers (Himmelberg and others, 1995). They also argued that in order to preserve the M_1 mineral assemblage observed at the western edge of the belt given a structurally and metamorphically continuous 120- to 50-Ma event, that rapid burial, a limited extent of thermal pulse (from the 70-Ma intrusive event along the Coast batholith), and rapid uplift must have occurred. They suggest that uplift rates of 6 km/10^6 years are required, which implies exhumation of the western edge of the belt in as little as several hundred thousand years.

A variety of indirect constraints on temperature ($^{40}Ar/^{39}Ar$ closure temperature of $2M_1$ muscovite, conodont color alteration indices of 5 to 5.5, lack of carbonate and organic carbon isotopic reequilibration, sphalerite-galena sulfur isotope pairs; chaps. 8, 10, 11) at Greens Creek suggest that maximum temperature during either the mineralizing event or Cretaceous regional metamorphism was no greater than about 275–350°C. These various lines of evidence coupled with the limited petrographic and microprobe data previously described are consistent with metamorphic conditions near the prehnite-pumpellyite to lower greenschist transition in the Greens Creek area. The preservation of primary isotopic and geochemical features of the deposit as well as the primary textural features of the ores described in this chapter further suggest that the M_1 metamorphic event was neither pervasive nor long lived.

Ore is nearly continuous along the phyllite/argillite contact and consists of three main orebodies—the East, West, and Southwest—and three extensions (fig. 2). The East orebody outcrops near the northeastern edge of the property, plunges shallowly to the southwest, and dips steeply west, flattening out gradually into the West orebody. The Klaus thrust fault separates the East and West orebodies approximately halfway through the flat. West of the flat, the West orebody continues beneath the Klaus fault as a thin horizontal layer, which dips to near vertical and then swells into a multiply folded and thickened mass that occupies a trough-shaped depression in the phyllite/argillite contact. A southward extension of the West orebody is hosted entirely within the hanging-wall argillites. The Northwest extension is a dextral fault translation of the western portion of the West orebody along the Maki fault, a major, near-vertical, strike-slip fault that cuts the property in two.

The Southwest orebody extends from the West/Northwest orebody in a complex helical fold that plunges shallowly to the southwest. Like the southward extension of the West orebody, the upper portion of the Southwest orebody transgresses the phyllite/argillite contact into the argillites. Maximum separation is about 35 m. The 200 South orebody is a southward extension of the Southwest orebody.

Deformation at Greens Creek is extremely complex and involves at least four periods of folding, one period of semiductile shearing, and two periods of faulting (see chap. 7). Continuity of the orebodies is interrupted by numerous thrusts and strike-slip faults on and parallel to the Klaus and Maki faults. The four phases of folding have further modified the deposit morphology. However, with few exceptions the ore horizon is traceable along the phyllite/argillite contact throughout the mine. Restoration of 600 m of movement along the Maki fault and 200 m of movement along the Klaus fault (P.A. Lindberg, written commun., 1994) results in a single orebody with a thickened central core in the West/Northwest orebody, which thins to the north, east, and south. The only indication that stacked orebodies may be present is the separate occurrence of ore above and south of the main ore concentration in the 5250 orebody (fig. 2).

Previous Mineralogical and Mineral Geochemical Studies

The earliest report on the mineralogy of Greens Creek ores of which we are aware consists of a brief summary and petrographic descriptions of six samples from the East orebody (George Alorno, written commun., 1987). Two samples of phyllite, one argillite, one white ore that probably would be currently classified as a white carbonate ore type, and two massive sulfide ores are described in detail. The major conclusions were that (1) variable deformation and degree of recrystallization between the phyllites and argillites indicate that the ore horizon is a tectonic contact, (2) massive sulfides

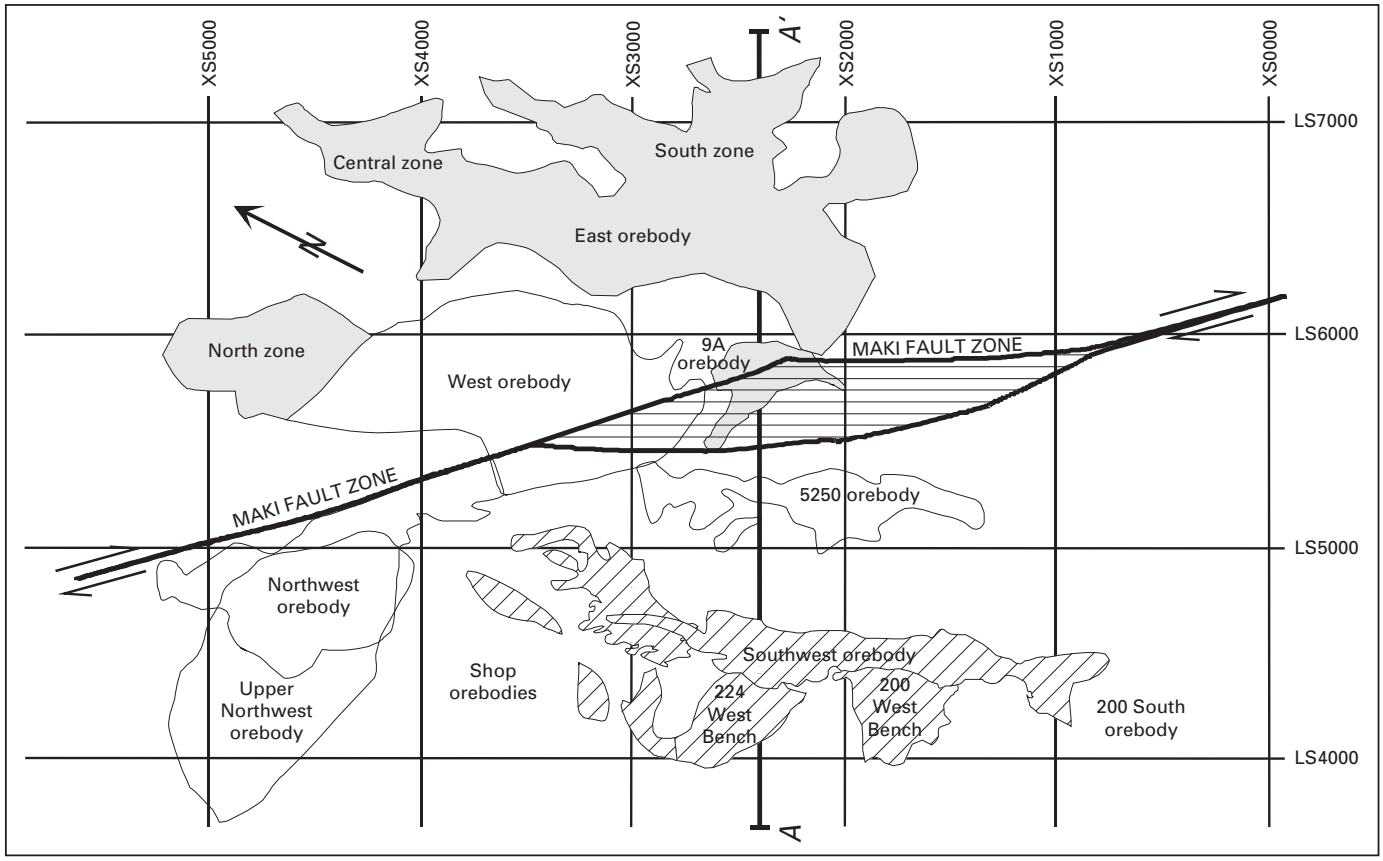

PLAN VIEW OF THE GREENS CREEK DEPOSIT.

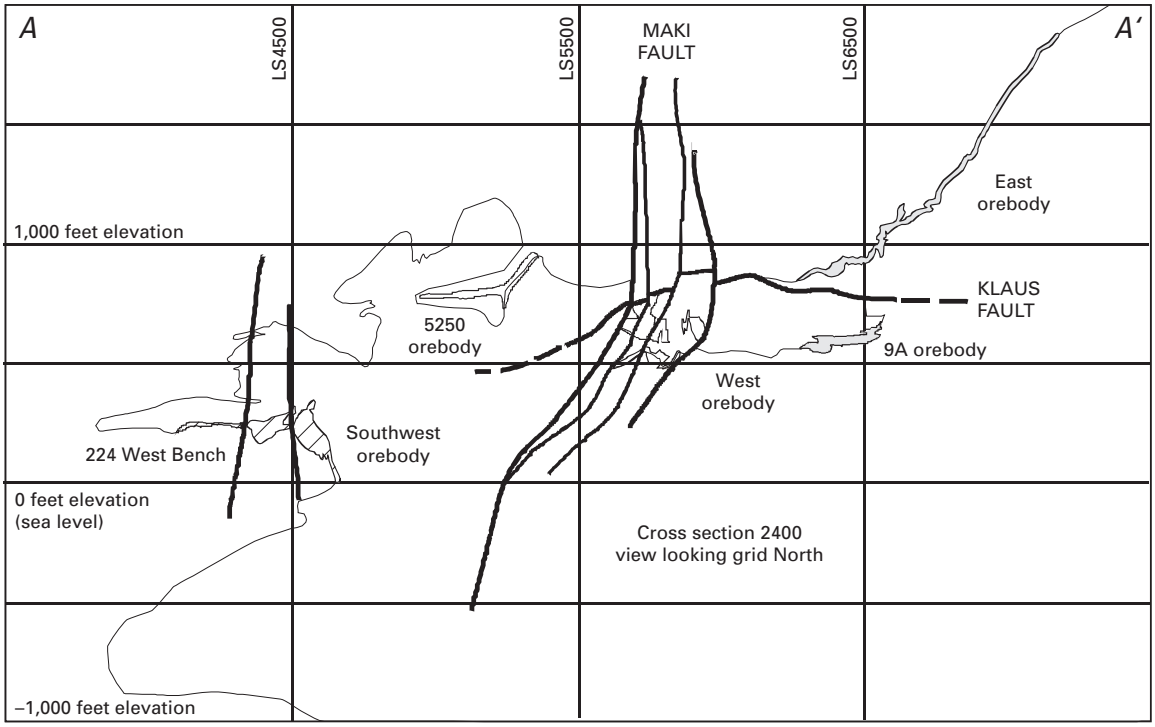

CROSS-SECTIONAL VIEW OF THE GREENS CREEK DEPOSIT.

Figure 2. Plan and cross-sectional views of the Greens Creek deposit showing features described in the text.

show a mix of primary and intensely granulated textures but no evidence for ductile deformation, and (3) the white ore sample contains abundant cymrite (hydrous barium aluminosilicate) and probably barian muscovite. Importantly, Alorno (written commun., 1987) also noted that the ore sulfides, particularly tetrahedrite, were confined to veinlets in the white ore and were not part of the "early assemblage." Both polycrystalline quartz and rotated dolomite porphyroblasts were observed in the phyllites, establishing a predeformation age of silica-carbonate alteration, similar to the findings of this study (V.M. Anderson and C.D. Taylor, unpub. data, 2000), and compositional layering in the phyllite occasionally was truncated against pyrite bands. If so, this observation suggests the presence of a premineralization fabric in the phyllites that is probably equivalent to the S_1 foliation of current usage (see chap. 7). Alorno's report documents the occurrence of all of the currently known major sulfide minerals as well as gangue graphite, rutile, ilmenite, "green mica," and the postulated barian muscovite. Although cymrite may be present, it has not been documented in any of the later studies. He notes the presence of delicate botryoidal features in pyrite-tetrahedrite-sphalerite bands, describes either cataclasis or the lack of deformation features in pyrite, and "granoblastic," "annealed," and "flame" textures in galena and sphalerite. Parageneticaly, Alorno (George Alorno, written commun., 1987) notes the remobilization of tetrahedrite and galena into fractures in, and as matrix to, pyrite and refers to "pseudoframboidal" pyrite features produced by replacement of base-metal sulfides by pyrite. Additionally, he makes the important observation that early primary textured pyrite is commonly overgrown by euhedral pyrite.

The next and most significant effort at understanding the mineralogy and mineral chemistry of the ores at Greens Creek is contained in a series of internal mining company reports. These reports detail the results of three major phases of work. The first phase consists of three reports that describe the mineralogy and mineral chemistry, as determined by electron microprobe analysis, on a variety of mill products drawn from East orebody ore: mill head; lead (Pb), zinc (Zn), and bulk concentrates; tails; and final tails (E.U. Petersen, written commun., 1991, 1992a, b). These early studies recognized the complexity of the silver (Ag) mineralogy at Greens Creek (see table 1) and placed some preliminary constraints on the mineral chemistry of a few of the major phases. East orebody sphalerite was shown to have fairly homogeneous low iron (Fe) content (less than 1.0 percent) and measurable cadmium (Cd), mercury (Hg), copper (Cu), and manganese (Mn) (less than 1.0 percent combined). Analyses of tetrahedrite showed them to be the zinc-antimony-rich, iron-arsenic-poor end member, with measurable cadmium. Silver in tetrahedrite ranged from about 0.5 to 6.5 percent with several exceptionally silver-rich analyses up to 15.9 percent. E.U. Petersen (written commun., 1992) also noted the common occurrence of an unknown silver-rich mineral (up to 44 percent silver), previously identified as covellite, which plots along the covellite (CuS) – acanthite (Ag_2S) join.

Results of the second phase of mineralogical research at Greens Creek are contained in a series of memorandums from Chris J. Carter to the Greens Creek mine staff (C.J. Carter, written commun., 1994a, b, c, d). In these memorandums, Carter presents a reevaluation of Petersen's concentrate microprobe data and a preliminary evaluation of microprobe data from a set of 12 samples collected from the Southwest orebody. A report containing detailed descriptions and assay data provides context for the 12 hand samples (Debora Apel, written commun., 1993). Carter's evaluation of Petersen's data focuses on the variation of silver content in tetrahedrite and the possible utility of using silver as a vector for exploration. He suggests that the broad range of silver/copper values determined for tetrahedrites from East orebody concentrates indicates that original metal zoning features have probably been preserved and thus might provide a useful exploration criterion.

Petrographic and geochemical studies of mineralogy in the Southwest orebody samples noted a broad range of sulfide textures and grain sizes. Four distinct textural varieties of pyrite were observed: euhedral, spongy, colloform, and framboidal. Minor to moderate amounts of arsenopyrite also were observed, and microprobe data on pyrite, arsenian pyrite, and arsenopyrite indicated measurable gold and nickel (Ni). Galena was noted to be weakly argentiferous and thus not a significant contributor to the silver budget. The antimony content of tetrahedrite was shown to vary greatly from about 13 percent (expressed as the molar ratio Sb/[Sb+As]) to about 81 percent, demonstrating that a series of tetrahedrite-tennantite minerals are present in the Southwest orebody. These tetrahedrites also have three times the average silver content (expressed as the molar ratio Ag/[Ag+Cu]) than those in the East orebody (17.6 versus 5.2 percent), lower zinc content, and higher iron and cadmium content. They also report silver-rich minerals belonging to the proustite-pyrargyrite series, jalpaite, and an unidentified mineral with 86 weight percent silver (C.J. Carter, written commun., 1994). Ag/Ag+Cu versus Sb/Sb+As plots of tetrahedrite analyses were interpreted as having three distinct trends, indicating three distinct starting fluid compositions may have contributed to the ore-forming process (C.J. Carter, written commun., 1994). Sphalerite iron content was observed to be as homogeneous as in East orebody sphalerites with perhaps a slightly higher average value (0.9 weight percent).

The potential use of iron in sphalerite and Ag-Cu versus Sb-As trends in tetrahedrites as exploration tools led to a third phase of mineralogical research. E.U. Petersen and D. Chirban (written commun., 1994) conducted a study aimed at characterizing the mineralogical and chemical zoning of the Greens Creek deposit based on tetrahedrite chemistry. Tetrahedrites in 44 samples primarily from drill holes on the 2400 cross section of the Lower Southwest orebody, representing four major ore types, were analyzed by electron microprobe (Denise Chirban, written commun., 1995; Denise Chirban and E.U. Petersen, written commun., 1996).

The concentration of silver in tetrahedrite was found to vary from 2.45 to 20.95 weight percent and was accompanied by large variations in all three solid solutions as expressed by

X_{Ag} (Ag atoms/[Ag+Cu]), X_{Sb} (100 × Sb atoms/[Sb+As+Bi]), and X_{Zn} (100 × Zn atoms/[Zn+Fe]). The silver index, X_{Ag}, ranged from 0 to 0.4, the antimony index, X_{Sb}, ranged from 0.1 to 1, and the zinc index, X_{Zn}, ranged from 0.1 to 1. They determined that the chemical variation within a sample was much less than the variation between samples, indicating that the average of several spot analyses of a sample is a good representation of the tetrahedrite composition for that location. This also implies that zoning patterns, if present, should be discernible between samples. They applied this to cross-stratigraphic variations in ore types on the 2400 cross section and concluded that each ore type has its own "mini-stratigraphy" with all of the above index ratios increasing stratigraphically upward. Each ore type was found to have characteristic tetrahedrite compositions, which define a trend. However, these trends were not sufficient to identify an ore type based on inspection of single spot analyses (Denise Chirban and E.U. Petersen, written commun., 1996). Their work on the high-silver sulfosalt minerals demonstrated that tetrahedrite could coexist with, or occur independently of, the covellite-acanthite solid solution, mckinstryite, or jalpaite. Data from one pulp sample also indicates that these silver-rich minerals may occur independently from tetrahedrite.

Finally, electron microprobe results were reported for a single sample of native-silver-bearing, high-grade white siliceous ore from the 764N1 stope of the Upper Southwest orebody (T.K. Bundtzen, written commun., 1996). The data indicate the presence of coarse grains of jalpaite occurring as bluish rims around native silver and that the silver contains less than 0.1 percent gold. The sample also contained euhedral crystals of gangue celsian or harmotome.

Ore Types

Ore lithologies at Greens Creek are broken into two main groups of massive sulfide ores and semimassive or disseminated sulfide gangue-rich "white" ores. The group of massive ores contain greater than 50 percent sulfides and consist of two types: (1) massive fine- to very fine grained ore in which base-metal sulfides are greater than pyrite (hereinafter referred to by the ore lithology code MFB, for Massive, Fine-grained, Base-metal-rich, and MVB, for Massive, Very fine grained, Base-metal-rich ores, respectively), and (2) massive medium- to very fine grained pyrite-rich ore in which pyrite predominates (hereinafter referred to as MFP and MVP, respectively). The distinction between the fine- and very fine grained ore types is subjective and based on the visual appearance of grain sizes in drill core. In general, the very fine grained ore types are so designated when individual sulfide grains cannot be seen with the naked eye. The MFBs are a medium to dark metallic gray to blue-gray (fig. 3*A*); the MFPs are bronze to metallic brown (fig. 3*B*). The MVBs and MVPs are similar in color to the coarser grained ore types with two notable variations. MVBs occasionally take on a distinct yellow-orange hue due to high concentrations of low-iron sphalerite (fig. 3*C*), and MVPs take on a light creamy bronze color due to increased content of arsenian pyrite. All the massive ores have variable subordinate gangue of quartz, dolomite, sericite, barite, and fuchsite. Graphite is a less ubiquitous but locally abundant gangue mineral. The massive sulfide ores constitute the main stage of ore formation.

The white ores are a group of mineralized lithologies that contain less than 50 percent sulfides and are defined by their principal gangue mineral. They commonly contain base- and precious-metal enrichments and are usually, but for core logging purposes are not required to be, of ore grade. The three types are (1) white carbonate ore (WCA) and (2) white siliceous ore (WSI), which are most common, and (3) white baritic ore (WBA). The WCAs are characterized by granular textured, medium- to coarse-grained dolomite (fig. 3*D*). Accessory gangue minerals are present but less abundant than in WSIs. WSIs are dominated by massive cryptocrystalline aggregates of hydrothermal quartz or chert and regularly contain significant dolomite, sericite, fuchsite, and barite (fig. 3*E*). WBAs are characterized by coarse, sugary, massive barite and other gangue (as above) (fig. 3*F*). They commanly are not ore grade despite their inclusion as an ore lithology. The white ores constitute the early stage of ore formation and precede the main stage of massive sulfide ores.

All the ore types previously mentioned include subtypes that are modifications resulting from veins, breccias, and gouge or rubble zones produced during faulting or folding. Veining due to secondary metamorphic remobilization and accompanying recrystallization can result in spectacular enrichments of free gold and a variety of silver-sulfosalt minerals, which are described herein. Ore breccias appear to be both primary sedimentary breccias produced by slumping of the massive sulfides and inclusion of clasts of the underlying as well as overlying host rocks, and tectonic breccias produced during deformation. Solution brecciation may also be present, particularly in the WCAs.

Figure 3 (facing page). Photographs of hand samples illustrating the various massive sulfide and white ore types: (*A*) typical MFB with primary-textured pyrite (py) in a matrix of sphalerite (sph) and galena (gn) (drill-core sample GC127-18, 1007′, ST–2 84 crosscut East orebody; (*B*) typical MFP (drill-core sample GC1136–05, 602′, Lower Southwest orebody), note the breccia texture caused by the brittle failure of massive pyrite; (*C*) typical MVB (drill-core sample GC1643–10, 272′, 200 South orebody), the orange color is due to the very high proportion of sphalerite in the sample and the low iron content of the sphalerite; (*D*) typical WCA (rib sample 164 crosscut, 82′, Lower Southwest orebody); (*E*) typical WSI (rib sample from East orebody); (*F*) typical WBA (rib sample from the 164 crosscut, 164N1 stope, Lower Southwest orebody.

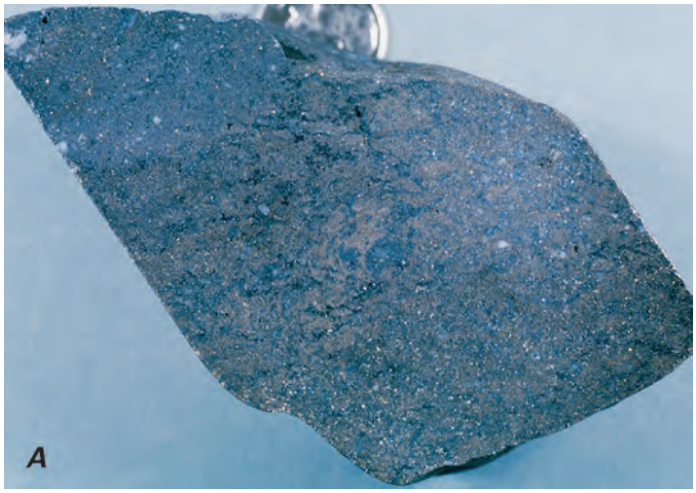
A


B

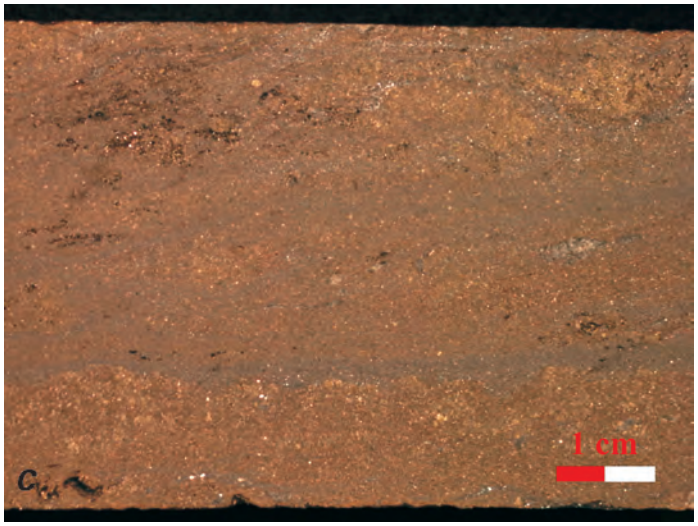
1 cm
C

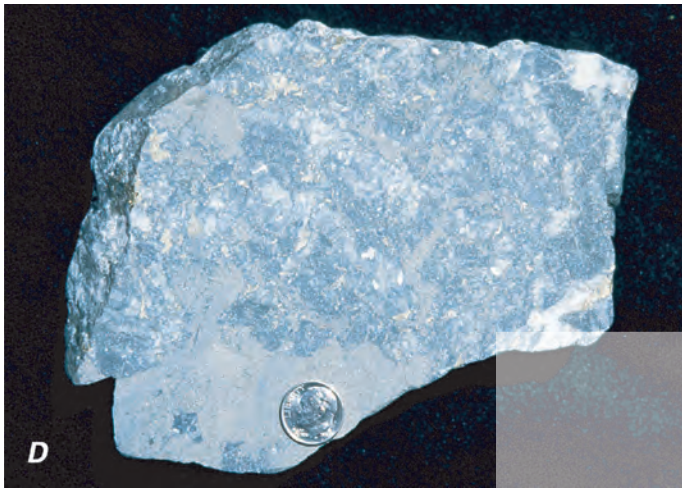
D

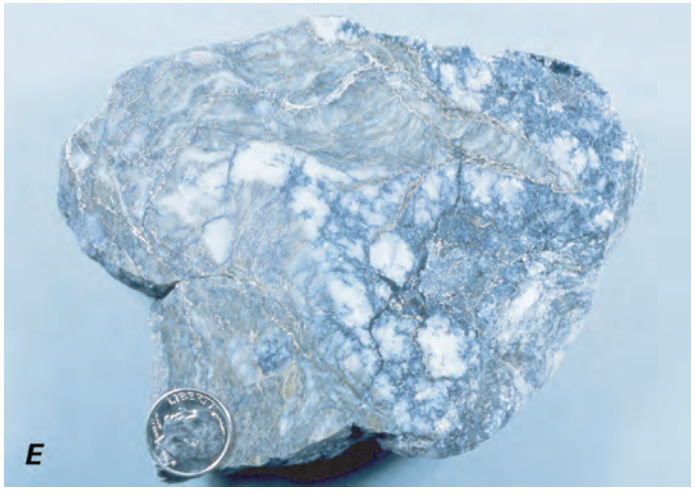
E

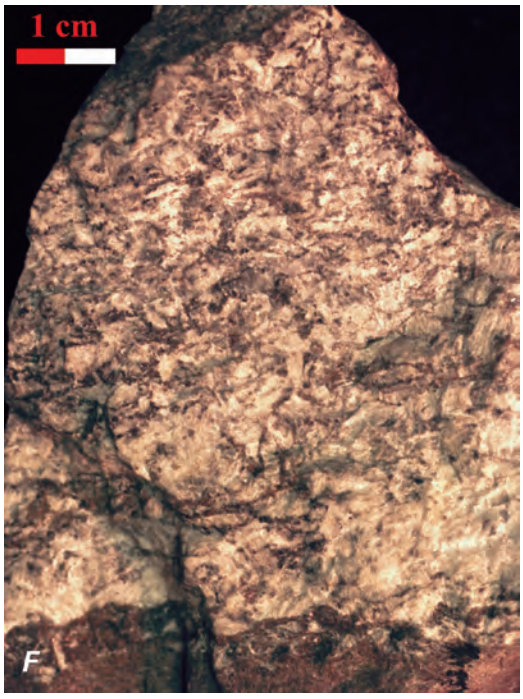
1 cm
F

Primary Ore Mineralogy and Textures

Roughly 30 percent of the Greens Creek ores retain primary mineralogy and textures. With one notable exception, primary features are present in massive, homogeneous, fine-grained MFPs that usually contain a high percentage of silica gangue. Apparently, large, cohesive blocks of pyritic ore have acted as undeformed nuclei around which the more ductile MFBs have flowed during deformation. Brecciation of the MFPs is a common feature within these cohesive blocks, resulting in angular to subangular, tectonically milled clasts of primary-textured MFP in a sheared sulfide matrix consisting mostly of more ductile and recrystallized base-metal sulfides (fig. 4*A*). Clear evidence for primary depositional layering of sulfides is lacking. However, mineralogically banded massive ores are common and are composed of entirely recrystallized sulfides (fig. 4*B*).

Within primary-textured MFPs, framboidal, colloform, and dendritic-textured pyrite is common and is intimately intergrown with a variety of base-metal sulfides and sulfosalts. Framboids are commonly in the 1–5 micrometer (μm) size range and are as large as 30 μm (figs. 5*A*–*C*). Colloform-textured areas can be millimeters in size (fig. 5*D*), with individual mineral bands ranging from less than 1 to 10 μm in width (fig. 5*E*). Mineral bands are most commonly composed of pyrite interbanded with sphalerite, galena, tetrahedrite, and a lead-antimony sulfosalt mineral (fig. 5*F*). Rarely, chalcopyrite replaces pyrite or infills bands between pyrite layers in the more copper-rich orebodies (fig. 5*G*). Dendritic-textured areas of pyrite are less common, only occur in MFP, and can have individual dendrites in the 100–200 μm size range (fig. 5*H*). Common accessory mineralogy in the primary textured ores includes sphalerite, galena, tetrahedrite, chalcopyrite, free gold, and a variety of Pb-Sb-As (-Hg-Tl) sulfosalts.

Primary-textured sulfides are also present in WCAs. Rounded grains of pyrite up to a centimeter in diameter with radial growth textures occur in a matrix of massive, coarse crystalline dolostone. These features produce a “pudding stone” texture and are reminiscent of diagenetic pyrite nodules (fig. 4*C*). Similar nodular pyrite textures, fragments of nodules, pyrite rinds, and concentrations of framboidal and colloform pyrite intergrown with base-metal sulfides also occur in association with concentrations of white, hydrothermal dolomite that typically cuts more massive, coarse crystalline dolostone. These textures are clearly linked to hydrothermal veining and in some cases may be produced by solution brecciation of footwall dolostones and WCAs followed by precipitation of dolomite and quartz cements in the resulting cavities (fig. 4*D*).

Recrystallized and Remobilized Ore Mineralogy and Textures

Recrystallization of the primary textures in individual hand samples ranges from 20 percent to 100 percent and results in a range of textures. Incipient recrystallization results in the formation of polyframboidal aggregates (rogenpyrite; fig. 6*A*), “spongy” textured pyrite, and atoll-shaped pyrite. Spongy texture is most common in the massive ores in millimeter- to centimeter-scale areas of massive and aggregated pyrite. These areas often show relict framboidal and colloform textures. The pyrite itself commonly appears quite “clean” or monomineralic. However, the spongy areas are full of micrometer-scale inclusions of other sulfides, sulfosalts, and gangue minerals (fig. 6*B*). The centers of euhedral pyrite crystals larger than about 100 mm also tend to have spongy texture. As recrystallization progresses, atoll-shaped pyrite forms at the expense of framboids and colloform pyrite (fig. 6*C*). The larger aggregates of polyframboids and spongy textures coalesce further into large areas of inclusion-rich anhedral to subhedral pyrite (fig. 6*D*).

The major effects of more advanced recrystallization is much coarser grain sizes and the formation and(or) remobilization of secondary, precious-metal-enriched minerals (fig. 6*E*). Pyrite recrystallization is characterized by development of euhedral crystals and polygonal textured masses that appear to be unzoned and free of mineral inclusions (fig. 6*F*). Recrystallization of pyrite tends to roughly double the grain size; for example, pyrite euhedra in areas of 1–5-μm framboids are 5–10 μm in size. In recrystallized aggregates or massive areas of pyrite with development of polygonal texture, individual grains are commonly in the 50–100-μm range. In MFPs that have been entirely recrystallized, pyrite euhedra are commonly in the 0.1- to 1-mm size range or larger (fig. 6*G*). Secondary minerals occur as discrete rounded inclusions within pyrite grains (figs. 6*H* and *I*), as growth zones within, and as margins to, pyrite (figs. 6*J* and *K*), and as matrix to pyrite euhedra. Subhedral to euhedral sphalerite occurs in recrystallized MFB, usually in a matrix of anhedral galena (figs. 6*L* and *M*). Secondary mineralogy includes chalcopyrite, sphalerite (low iron), galena, free gold, electrum, tetrahedrite (antimony-rich), bornite, covellite, pyrargyrite, and a host of other sulfosalt minerals. Rare realgar has been identified (by X-ray diffraction) in the WBAs of the 200 South orebody. Base-metal sulfides in recrystallized ores most commonly occur as anhedral intercrystalline masses of secondary sphalerite, galena, chalcopyrite, tetrahedrite, and pyrargyrite. Individual anhedral crystals are commonly 50–200 mm in size (fig. 6*N*). Secondary sulfides also commonly occur in late fractures and veinlets millimeters wide and centimeters long (figs. 6*O* and *P*).

An interesting and potentially genetically important modification that affects MFPs in proximal, copper-arsenic-gold-rich areas of the deposit is the occurrence of subhedral to euhedral, light creamy yellow to white, arsenian pyrite (FeS_2 with variable substitution of arsenic for iron) and arsenopyrite (FeAsS, 46 percent arsenic). These phases appear to replace primary pyrite (figs. 7*A*–*C*) or form as overgrowths on primary-textured pyrite masses (figs. 7*D* and *E*). They are present in trace amounts to as much as 50 percent of a sample. Powder X-ray diffraction analyses of two MFP ores, each with approximately 50 percent of this sulfide visible in polished thin section, confirmed the presence of arsenopyrite, but only in trace to minor amounts. In both cases the major

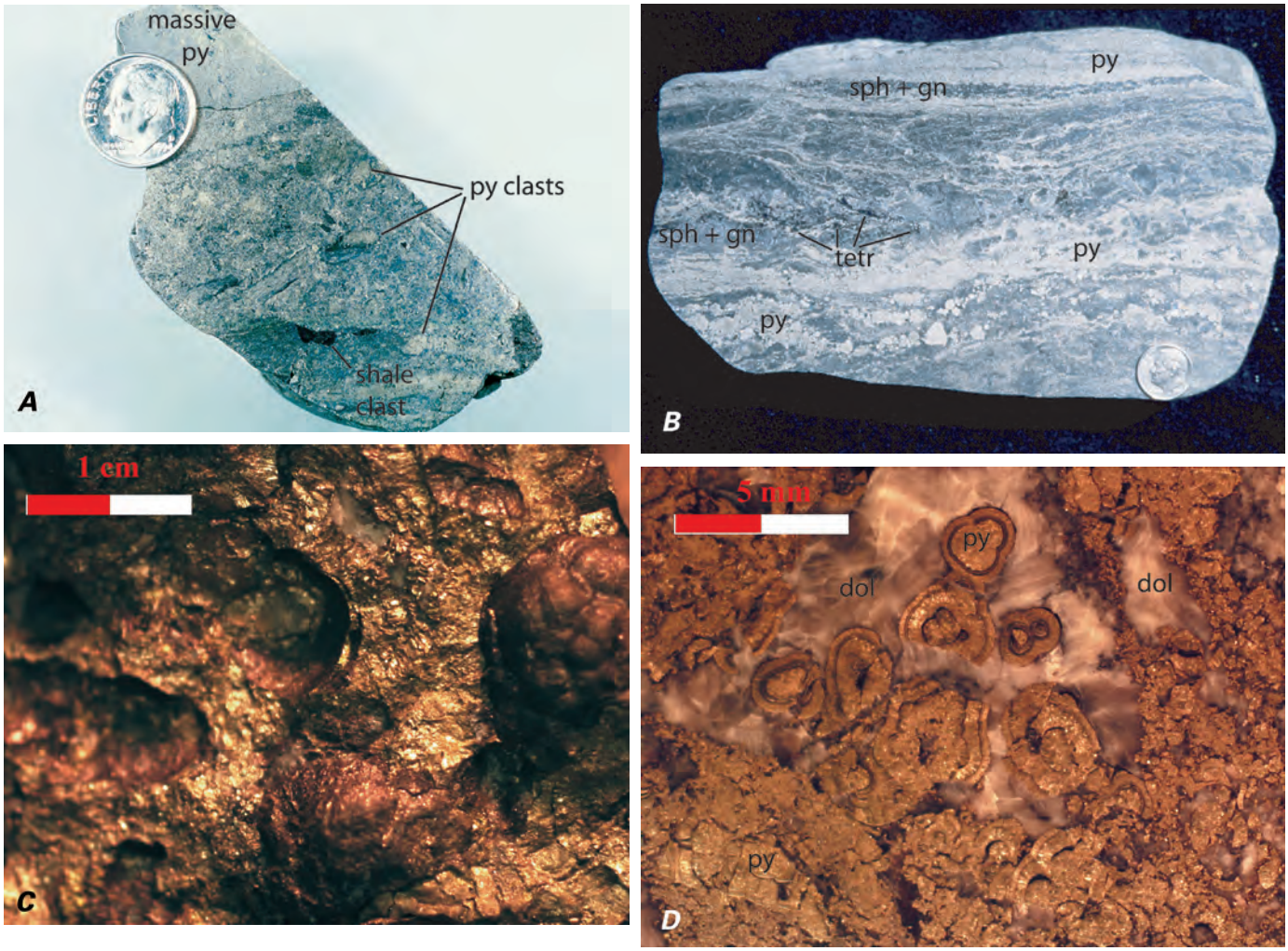

Figure 4. Photographs of hand samples illustrating textures present in various ore types: (*A*) brecciated MFP consisting of angular to subangular, tectonically milled clasts of siliceous, primary-textured, fine-grained, pyritic massive ore in a sheared sulfide matrix consisting mostly of more ductile and recrystallized base-metal sulfides (drill-core sample GC1136-04, 594.5′, Lower Southwest orebody); (*B*) tectonically banded MFB (rib sample from the 764 crosscut, 764N1 stope, Upper Southwest orebody); (*C*) nodular diagenetic pyrite texture in MFP (rib sample from the 2250 crosscut, 215 stope, Lower Southwest orebody); and (*D*) closeup photograph of WCA showing nodular pyrite textures, fragments of nodules, pyrite rinds, and concentrations of framboidal and colloform pyrite intergrown with base-metal sulfides in association with concentrations of white, hydrothermal dolomite usually cutting more massive, coarse crystalline dolostone (drill-core sample GC1092-02, 711′, Lower Southwest orebody). py, pyrite; sph, sphalerite; gn, galena; dol, dolomite; tetr, tetrahedrite.

phase identified was pyrite, indicating that the majority of the creamy white mineral observed must be arsenian pyrite. Rarely, euhedral arsenopyrite has been observed in a silica-dolomite matrix (fig. 7*F*).

Physical remobilization of the more ductile base-metal sulfides is indicated by fractured masses of pyrite filled with flow-textured anhedral chalcopyrite, galena, and tetrahedrite (fig. 6*E*). Flow-textured galena is characterized by the near total absence of the triangular pits usually observed in unstrained galena (fig. 6*L*). Physical remobilization and recrystallization in tectonized ores is probably responsible for creating the mineralogically segregated layers in banded ores. Creation of base-metal-rich veinlets and infilling of fractures by physical remobilization is an important process of metals redistribution in ores on a hand-sample scale and is ubiquitous in the more thoroughly recrystallized and tectonized ores. It is distinguished from the process of chemical remobilization by the lack of associated gangue minerals in the base-metal-rich fractures, veinlets, and piercement structures.

Chemical remobilization and reprecipitation of base-metal sulfides is also a locally important process and is characterized by the formation of paragenetically late veinlets and veins of chalcopyrite, sphalerite, galena, tetrahedrite, and pyrargyrite usually in association with quartz and dolomite (figs. 6*Q* and *R*). Occasionally, sericite and fuchsite gangue are present as well. Yellow and silvery-white gold is present

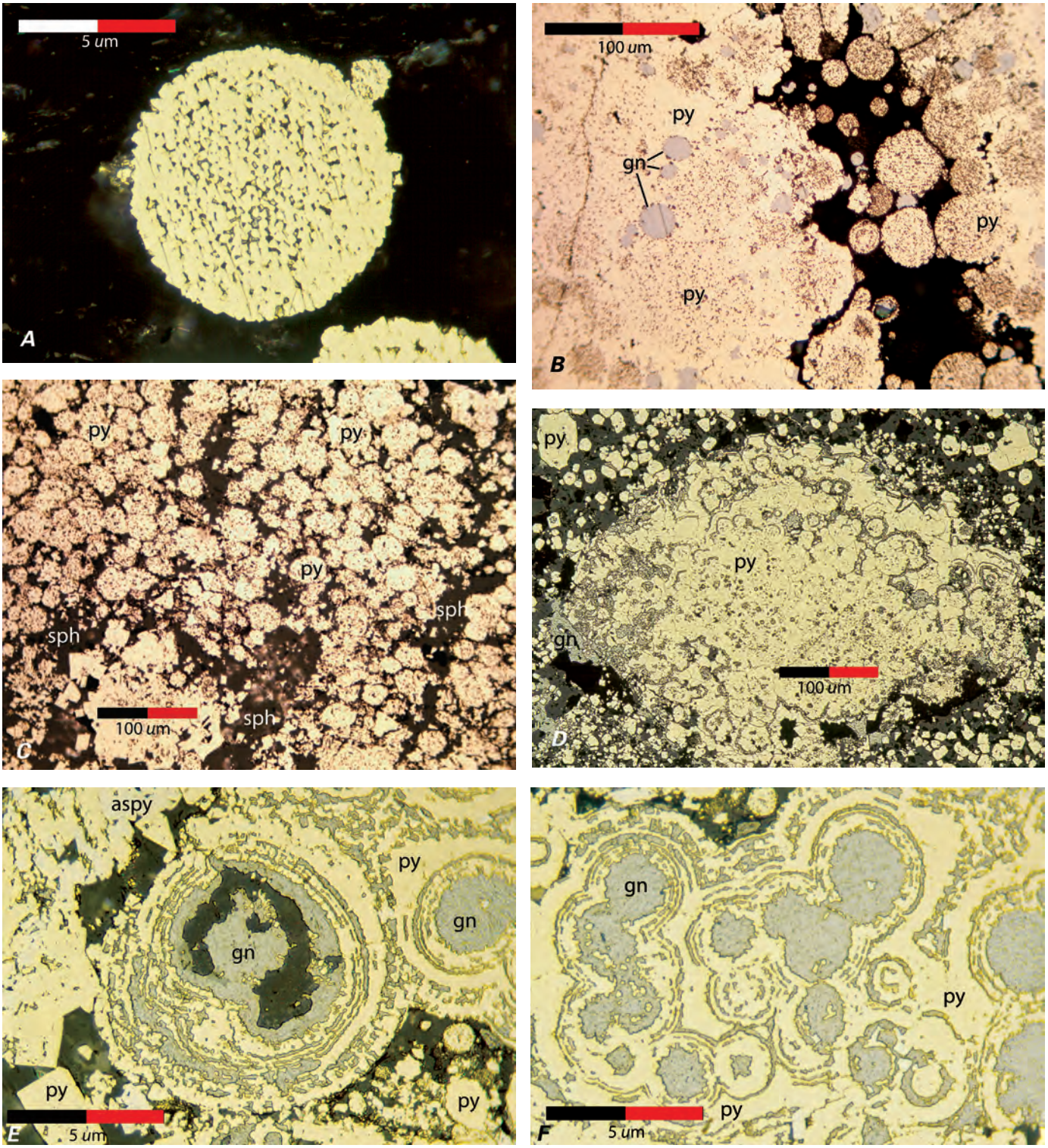

Figure 5 (above and facing page). Photomicrographs of polished thin sections showing primary mineral textures: (*A*) framboidal pyrite (rib sample 96GC–14, 31', 344 crosscut, Lower Southwest orebody); (*B*) pyrite (py) framboids and galena (gn) spheres in spongy-textured to massive pyrite (drill-core sample GC1643–04, 75' 200 South orebody); (*C*) aggregated pyrite framboids in a matrix of sphalerite (sph) (drill-core sample GC1643–03, 54', 200 South orebody); (*D*) colloform-textured aggregate of pyrite with a spongy-textured interior and growth zones composed of sphalerite, galena, and tetrahedrite (rib sample 96GC–12, 21.5', 344 crosscut, Lower Southwest orebody);

in chemically remobilized veins and is particularly abundant in association with late quartz-carbonate-pyrargyrite veins. Concentrations of these precious metal enriched veins usually occur in or within close proximity to areas of primary-textured ore and account for the highest grade ores in the mine, with total metal values reaching $10,000/ton.

Free Gold—Mineralogy and Textures

Free gold is a relatively common feature at Greens Creek and has been found in a wide variety of both ore and host-rock lithologies. Two types are visually distinguishable, and a third was identified during LA–ICP–MS analysis. Bright yellow gold of high fineness occurs in thin section as rounded blebs and inclusions from 5 to 100 µm in size, although the most common size is about 5 to 20 µm (fig. 8*A*). Most of the grains are in cracks in pyrite and in the matrix to pyrite grains in association with secondary chalcopyrite, sphalerite, galena, tetrahedrite, and pyrargyrite (figs. 8*B* and *C*). Most gold grains are in contact with either pyrite or arsenian pyrite (fig. 8*D*); however, a few grains were observed included within coarse-grained subhedral to euhedral pyrite (fig. 8*E*). Yellow gold is most commonly seen in the large blocks of MFP ore but also has been observed in all of the ore types at the mine and in both hanging-wall and footwall rocks, usually in association with quartz-carbonate veins.

The second type of free gold is silvery white and occurs predominantly as a thin foil coating late fractures and shear planes in underground exposures and hand samples (figs. 8*F* and *G*). In thin section, white gold appears as thin veinlets and spaced sheets that occupy fractures up to 0.5 millimeter wide. These fractures are paragenetically late and appear to be tension gashes and piercement structures that occur at high angles to S_2 foliation (fig. 8*H*). Geochemical data suggest this is a gold-silver electrum.

Free gold occurs in ores that exhibit a high degree of recrystallization and remobilization of the more ductile sulfides and are usually in close proximity to areas of primary-textured ores. Exceptions include yellow gold that occurs in quartz-carbonate veins in the host rock and rare instances of white gold foil in highly sheared and fractured argillites in the immediate hanging wall. These electrum-bearing quartz-carbonate veins typically are within 1–2 m of high-grade primary ores. Yellow gold has also been observed in association with chalcopyrite and tetrahedrite in hairline fractures cutting late diabase dikes in the 200 South portion of the Lower Southwest orebody. This relationship thus requires remobilization of gold at some time after emplacement of the dikes.

The two types of gold, as well as native silver, are easily distinguished based upon LA–ICP–MS geochemical studies of free gold separates recovered from the mill (figs. 9*A–I*). Laser traverses across 0.5- to 1.0-mm-sized grains recovered from heavy concentrates, represented as time versus elemental intensity plots, clearly indicate the presence of nearly pure gold grains with a high ratio of gold to silver (figs. 9*A*, *D–F*). Other grains that appear silvery-white on polished surfaces show lower gold-to-silver ratios and consistently elevated mercury, demonstrating that the silvery white gold is actually a

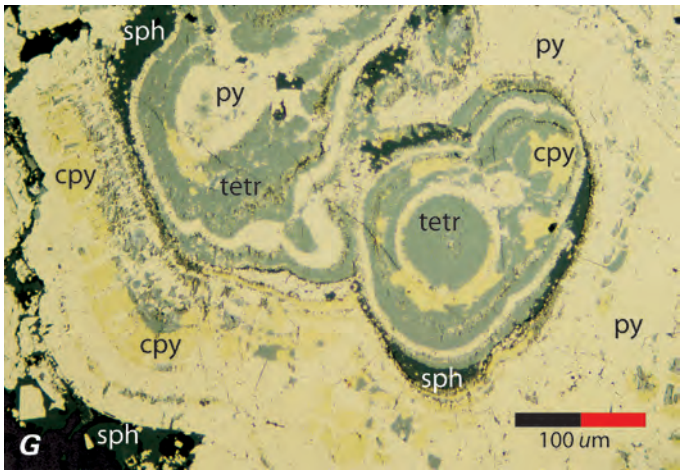

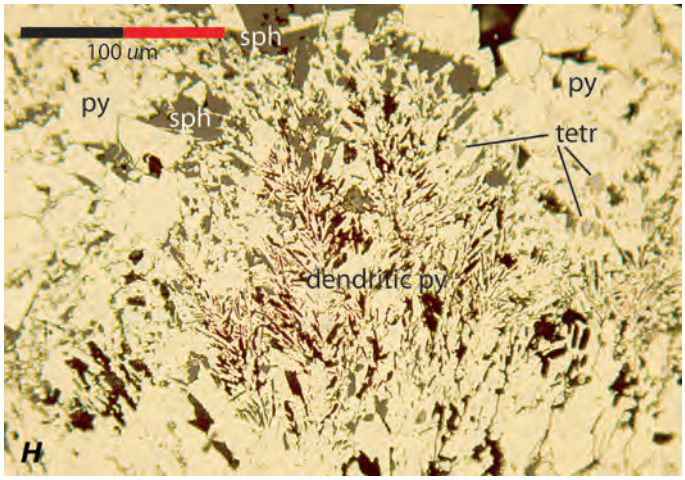

(*E*) colloform banded spheres in pyrite with growth bands filled with galena or perhaps lead-antimony sulfosalt minerals (rib sample 96GC-13, 25.5′, 344 crosscut, Lower Southwest orebody); (*F*) aggregate of colloform shapes in pyrite (rib sample 96GC–13, 25.5′, 344 crosscut, Lower Southwest orebody); (*G*) chalcopyrite (cpy) infilling or replacing bands between pyrite layers in colloform-textured MFP (drill-core sample GC1527–09, 402.5′, Northwest orebody); and (*H*) dendritic-textured pyrite fronds in massive pyrite (rib sample 96GC–16, 43.5′, 344 crosscut, Lower Southwest orebody).

gold-silver-mercury amalgam (figs. 9*B* and *C*). A few traverses suggest that some of the gold grains may also incorporate significant copper (fig. 9*G*). Silver grains either contain irregular inclusions of gold or are relatively pure (figs. 9*H* and *I*). The silver quickly tarnishes to a dirty, bluish-gray color, enabling visual identification in slides of the mill separates.

Paragenetic Relationships—Physical and Chemical Modification of Ores

Two major processes govern paragenetic relationships in Greens Creek ores. Primary ores are dominated by textures indicative of rapid crystallization, very early infilling of void spaces, and replacement of one sulfide by another during growth of the massive sulfide body, whereas the secondary ores are the product of recrystallization and remobilization of primary ores during zone refinement and metamorphism. In primary ores, framboidal and colloform pyrite are the earliest formed sulfides. Sphalerite, galena, tetrahedrite, and lead-antimony sulfosalts appear to be coeval and form the matrix of framboidal aggregates (figs. 10*A*; 3*A*; 5*C*; 6*A*) as well as the intervening bands in colloform-textured pyrite (figs. 5*D–F*). Bands of pyrite are nearly always present in colloform-textured ores; in the few cases where successive bands of base-metal sulfides without intervening pyrite bands occur, they are present as colloform growths within predominantly pyritic primary-textured masses (figs. 10*B*; 5*G*). These primary-textured, pyrite- and base-metal-sulfide-rich masses appear to undergo modification early in the growth of the massive sulfide bodies by a process of zone refinement. Early, porous masses, composed of framboidal and colloform pyrite with a high percentage of sphalerite, galena, and lead-antimony sulfides (figs. 5*A*, *D–F*; 6*A*), progress into more densely packed pyrite-chalcopyrite-arsenopyrite-rich masses through a combined process of pyrite coalescence and replacement of the base-metal sulfides. The resulting ores exhibit a progression of textures characterized by the destruction of discrete framboids (figs. 5*B*; 6*B*) and the formation of polyframboidal (figs. 6*A*; 10*A*) and spongy-textured (figs. 5*D*; 6*C*, *I*) pyrite aggregates, atoll-shaped and subhedral pyrite grains (figs. 6*J*, *K*), and subhedral to euhedral arsenian pyrite and arsenopyrite (figs. 7*A–F*). Chalcopyrite generally occurs as matrix in the resulting pyritic masses along with a much lower percentage of sphalerite, galena, and tetrahedrite (figs. 6*E*, *G*). Replacement of the base-metal sulfides presumably results in expulsion of lead, zinc, and other trace elements upward and outward to form the MFBs. Rarely, in copper-rich primary-textured MFPs, chalcopyrite has been observed, partially replacing bands of other base-metal sulfides in colloform ores (fig. 5*G*). Several examples of framboids composed of chalcopyrite crystallites in a matrix of pyrite have been observed; however, it is questionable whether such examples indicate a paragenetically early position of chalcopyrite relative to pyrite (fig. 10*C*). Framboids composed of sphalerite or other base-metal sulfides have not been observed in this study. Graphite is a ubiquitous feature of primary ores and occurs as fine disseminations in the matrix between framboids and colloform-textured masses (fig. 5*C*) and in association with dendritic and spongy-textured pyrite (fig. 5*H*).

The formation of light creamy yellow to white, arsenian pyrite and arsenopyrite (figs. 7*A–F*) is a paragenetically important feature of the primary-textured ores and is of uncertain origin. It is most commonly observed in association with primary ores that have undergone incipient to moderate recrystallization. As the "dirty" trace-element-rich primary-textured pyrites undergo recrystallization, the stoichiometric reorganization of the pyrite mineral structure expels excess trace elements from its structure, including arsenic. Liberated arsenic is then available to form new arsenian pyrite or arsenopyrite. However, both arsenian pyrite and arsenopyrite are concentrated in areas of primary-textured ores where permeability is greater, either due to presence of abundant spongy-textured pyrite, loose packing of framboidal aggregates, or the presence of veining. This relationship suggests that arsenian pyrite and arsenopyrite may have formed early in the paragenesis, after the formation of primary-textured sulfides but prior to advanced recrystallization of the ores. A possible explanation is that these minerals represent a hotter, more reducing period of fluid circulation and mineral formation by replacement of earlier formed minerals during a zone-refining stage of sulfide mound growth.

Nonprimary-textured ores exhibit a range of features that suggest a progression from incipient through complete recrystallization and physical as well as chemical remobilization as a result of metamorphism. Incipient recrystallization causes individual framboids to coalesce into atoll-shaped grains, with centers filled with base-metal sulfides and rims of clean, bright pyrite (figs. 10*D*; 5*E–G*; 6*C*, *J*). Aggregates of framboids develop into large spongy-textured masses with numerous discrete inclusions of base-metal sulfides and graphite (figs. 10*E*; 6*D*, *H*, *I*). Graphite tends to recrystallize into felty concentrations of needle- or lath-shaped crystals that are aligned subparallel to S2 foliation (fig. 10*F*). As recrystallization progresses, large areas of inclusion-free pyrite form with relict framboidal shapes preserved in the interiors of the masses. Euhedral-shaped growth zones are defined by thin bands of sphalerite or galena (figs. 10*G*; 6*J*). Fully recrystallized pyritic ores are characterized by very large areas of inclusion-free, monomineralic pyrite with polygonal grain boundaries (figs. 10*H*; 6*F*). Matrix between the large areas of pyrite is filled with anhedral masses of sphalerite, galena, and tetrahedrite, which are generally also inclusion free (fig. 6*G*). Bright yellow free gold is most commonly seen in partially to fully recrystallized MFPs as inclusions within recrystallized pyrite grains (fig. 8*E*) and in matrix with base-metal sulfides (figs. 8*A–D*). In recrystallized MFBs, clean, euhedral pyrite and euhedral to subhedral sphalerite are contained in a matrix of anhedral galena and tetrahedrite (figs. 6*L–N*). Areas of macroscopically banded ore in thin section alternate between pyrite-rich and base-metal-sulfide-rich layers that are texturally as previously described (fig. 4*B*). Recrystallization of chalcopyrite-rich MFPs generally

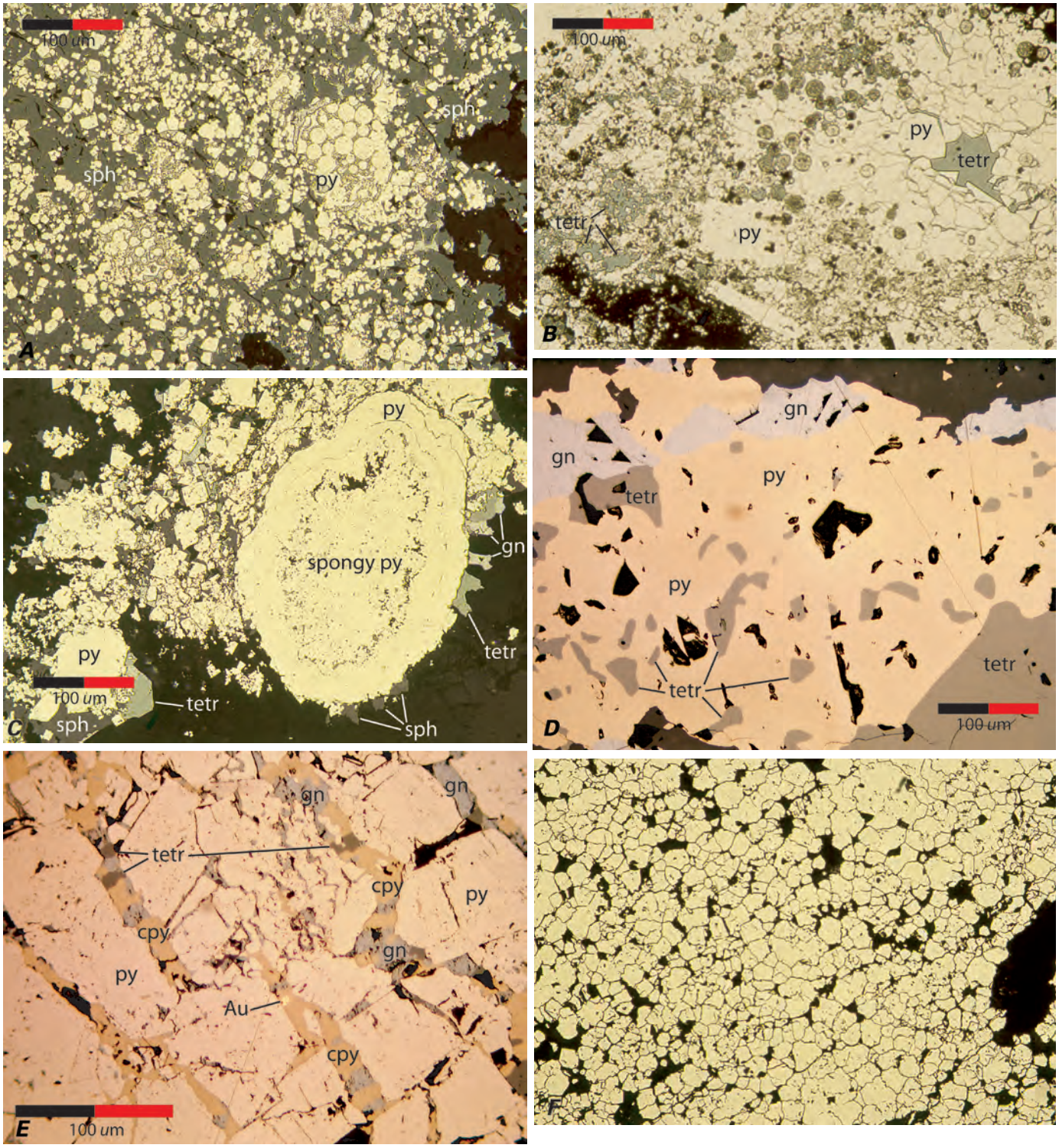

Figure 6 (pages 15–17). Photomicrographs of polished thin sections showing recrystallized ore textures: (*A*) growth of polyframboidal clusters in a matrix of sphalerite (sph) (rib sample 96GC–12, 21.5′, 344 crosscut, Lower Southwest orebody); (*B*) spongy-textured pyrite (py) with relict framboidal and colloform shapes, and numerous inclusions of sulfides, sulfosalts, and gangue (rib sample 96GC–18, 51′, 344 crosscut, Lower Southwest orebody); (*C*) atoll structure of clean recrystallized pyrite forming around a grain of spongy-textured pyrite (rib sample 96GC–13, 25.5′, 344 crosscut, Lower Southwest orebody); (*D*) clean anhedral pyrite with numerous rounded inclusions of tetrahedrite (tetr) and galena (gn) (drill-core sample GC1643–06, 119.5′, 200 South orebody); (*E*) veinlets of chalcopyrite (cpy), tetrahedrite (tetr), galena (gn), and yellow gold (Au) cutting recrystallized pyrite (drill-core sample GC1643–05, 100.5′, 200 South orebody); (*F*) clean, completely recrystallized, polygonal-textured pyrite (rib sample 96GC–14, 31′, 344 crosscut, Lower Southwest

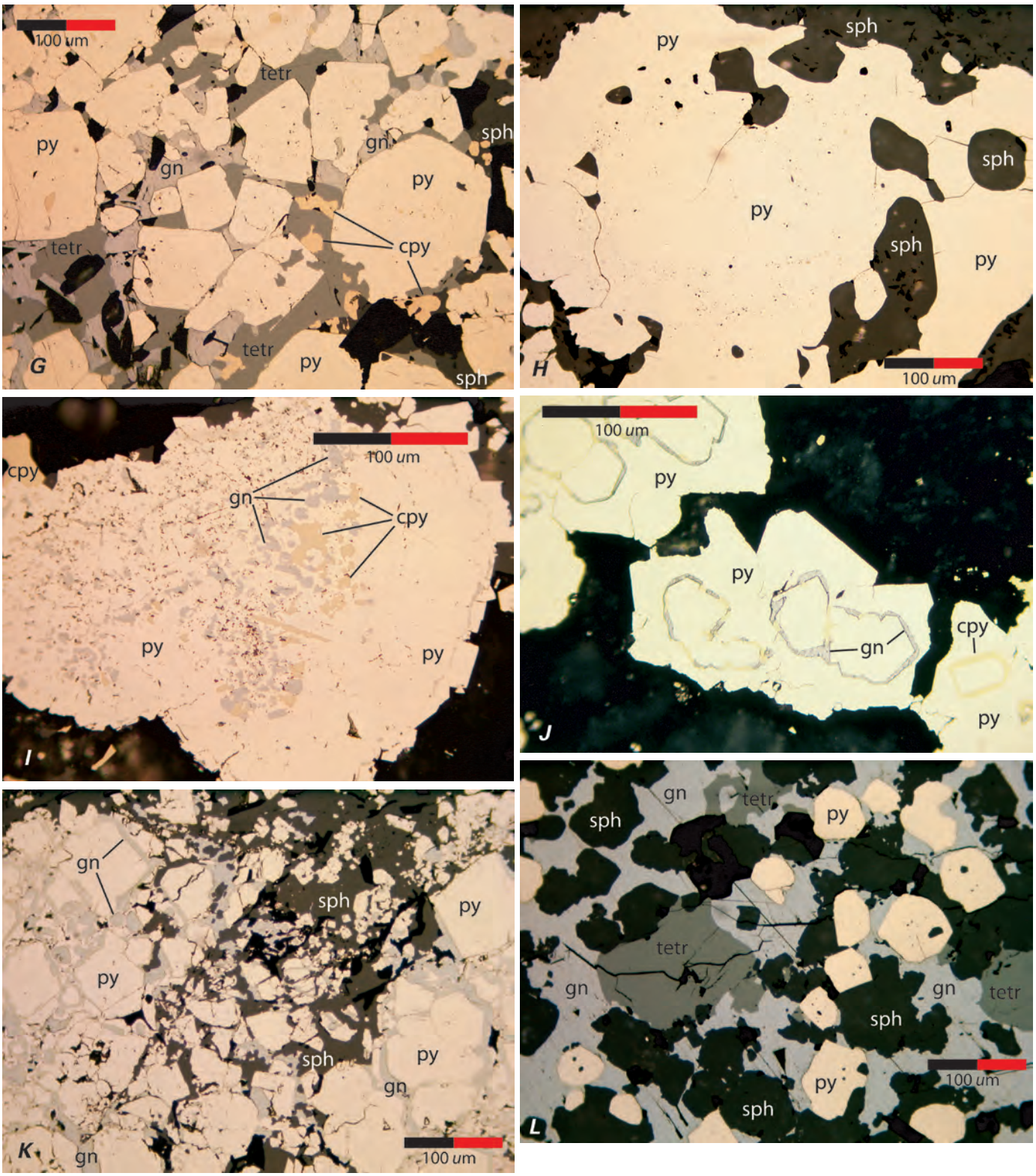

orebody); (*G*) recrystallized pyrite euhedra in a matrix of chalcopyrite, galena, tetrahedrite, and sphalerite (drill-core sample GC1643–08, 147.5′, 200 South orebody); (*H*) clean, recrystallized anhedral pyrite with rounded inclusions of sphalerite (drill-core sample GC1643–08, 147.5′, 200 South orebody); (*I*) partially recrystallized spongy pyrite with rounded inclusions of chalcopyrite and galena (drill-core sample GC1643–07, 143.5′, 200 South orebody); (*J*) clean, recrystallized pyrite with discrete, atoll-shaped growth zones of chalcopyrite and galena GC1527–08, 397.5′, Northwest orebody); (*K*) recrystallized pyrite with rims of galena (drill-core sample GC1643–11, 438′, 200 South orebody); (*L*) recrystallized euhedral pyrite and sphalerite in a matrix of anhedral tetrahedrite and galena (drill-core sample

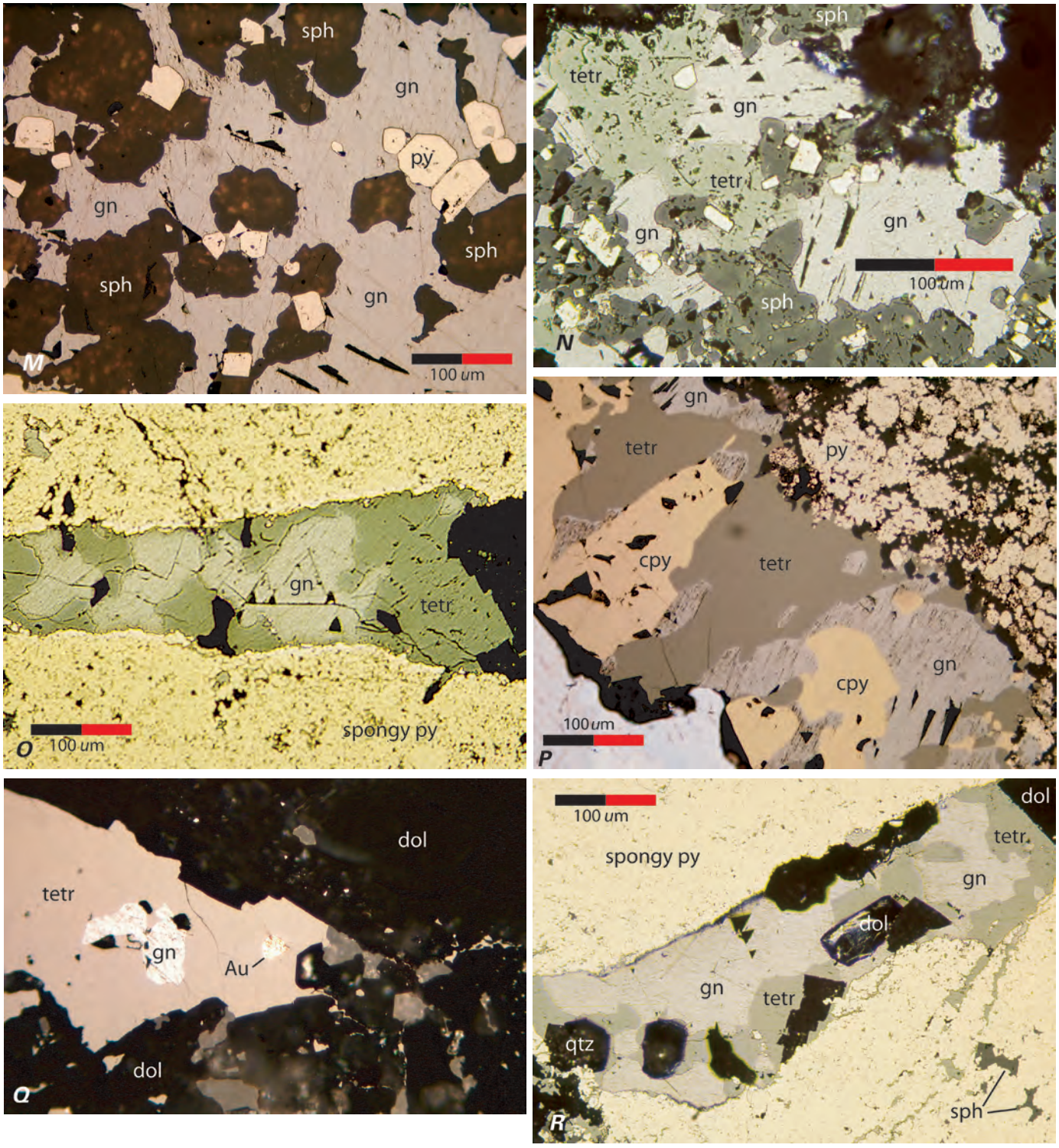

GC1643–01, 11.7′, 200 South orebody); (*M*) recrystallized euhedral sphalerite in galena matrix (drill-core sample GC1643–10, 272′, 200 South orebody); (*N*) inclusion-free, euhedral pyrite with anhedral sphalerite, galena, and tetrahedrite as matrix (rib sample 96GC–10, 18.5′, 344 crosscut, Lower Southwest orebody); (*O*) late galena and tetrahedrite veinlet cutting spongy-textured pyrite (rib sample 96GC–15, 39′, 344 crosscut, Lower Southwest orebody); (*P*) late chalcopyrite, galena, and tetrahedrite veinlet cutting framboidal pyrite (drill-core sample GC1643–03, 54′, 200 South orebody); (*Q*) remobilized veinlet of tetrahedrite, galena, and yellow gold in dolomite (drill-core sample GC1643–06, 119.5′, 200 South orebody); and (*R*) veinlet of anhedral sphalerite, galena, chalcopyrite, and tetrahedrite, and pyrargyrite cutting recrystallized pyrite (rib sample 96GC–17, 49′, 344 crosscut, Lower Southwest orebody).

progresses from spongy-textured masses of pyrite with chalcopyrite in the matrix and numerous small chalcopyrite inclusions to clean, monomineralic, polygonal-textured masses of pyrite with grain boundaries and intercrystal spaces filled with anhedral, monomineralic chalcopyrite (fig. 10*I*).

Physical remobilization of the ductile sulfides and electrum is a feature of the ores that is clearly related to Cretaceous deformation (figs. 6*E, O, P*; 8*B, C*). Evidence for flow-textured sulfides is most pronounced in areas of well-developed fabric where F2 and F3 folding can be discerned, as described by Proffett (chap. 7). Chemical remobilization and reprecipitation of sulfides is also a paragenetically late feature as indicated by the formation of veinlets and veins that cross-cut the metamorphic fabric (figs. 6*Q, R*).

LA–ICP–MS Mineral Chemistry Studies

Methods

The LA–ICP–MS analytical technique is a relatively new and rapidly evolving method of solid sample microanalysis that holds great promise for the study of ore mineral chemistry. A focused laser beam directed onto the surface of a mineral grain is used to excavate, or "ablate," a small volume of sample. The ablated material, in the form of micrometer-size fragments and condensed droplets, is transported by a carrier gas into the induction port of an ICP where the solids are melted, dissociated, and ionized. The ions are then focused into a quadrupole mass spectrometer where detection of a broad range of elemental masses occurs. The technique offers a wide dynamic range with trace and ultratrace detection limits coupled with simultaneous major-element determinations. However, the introduction of solid sample material to the instrument as opposed to the usual solution creates a new set of complexities. The mechanical, chemical, and physical factors involved in laser ablation and transport of the sample to the instrument result in a variety of fractionation effects (Ludden and others, 1995). Elemental fractionation occurs primarily because of secondary heating of the sample crater following the laser shot and thus, consequently, is of particular concern in infrared laser determinations. Elements more volatile than the host material can be volatilized from the area surrounding the crater and carried to the plasma, resulting in erroneously high element concentrations. For an element such as mercury this can be as much as 30-percent error in a poorly designed experiment. For this study, we used the Q-switched mode of an Nd/YAG laser with a shot duration of approximately 4 nanoseconds. Most sulfide minerals measured for this study have similar melting and boiling points, which should also minimize the fractionation effects reported in the literature. A second constraint on the accuracy of LA–ICP–MS analyses is the paucity of well-characterized reference materials for use in calibration and as secondary standards (Ridley, 2000). To date, only a handful of studies report quantitative analyses of solid mineral species (Norman and others, 1996). The only previous study of trace-element content in sulfides, using the LA–ICP–MS system in the Denver laboratory under operating conditions using a free-running laser with a 100-msec pulse duration, reported semiquantitative elemental concentrations (Viets and others, 1996). For the purposes of this study, a brief description of the Denver LA–ICP–MS system is given below and followed by a rough estimation of the accuracy and precision of the resulting analyses. For an in-depth review of the method, the instrumentation involved, and a detailed evaluation of the various fractionation factors, development of solid standards, and sources of analytical error, see Ridley and Lichte (1998), Ridley (2000), and references therein.

At the time the analyses of the Greens Creek ores were made, instrumentation in the Denver laboratory consisted of a CETAC laser, controlled by CETAC computer software, coupled to an ELAN 5000 ICP–MS. The Nd/YAG laser was operated in the Q-switched mode at a quadrupled frequency resulting in an ultraviolet wavelength of 266 nanometers, with a maximum energy output of about 3 millijoules. Analyses were performed on minerals previously identified by optical methods in standard (30 mm) polished thin sections. Thin sections were placed in a cylindrical Plexiglas sample cell driven by computer-controlled x-y-z stepper motors capable of movement in 0.05-mm steps. Laser spot selection was provided by a zoomable color video camera with 15–1500X magnification. After some experimentation to optimize the instrument response to the amount of sample ablated and the delivery to the ICP–MS, a beam diameter of 50 mm was selected. Individual mineral grains were sampled with two laser pulses per spot spaced by one second to allow the crater to cool and to offer a wider window for the analysis of the vapor cloud by the ICP–MS.

Calibration was performed using a combination of external standards. The ICP–MS was initially calibrated using in-house solution standards that use lutetium as an internal standard. The LA–ICP–MS system was then calibrated against an external glass standard (either NIST612 or GSE, an in-house standard) and checked against an experimental natural sulfide before, during, and after sample analyses. The natural sulfide standard used was a centimeter-sized crystal of pyrite from the Groundhog mine in southwest New Mexico (Hawksworth and Meinert, 1990). This pyrite was selected due to its large range of measurable trace elements and its relative homogeneity based on rastered laser analysis as compared to the solution ICP–MS method. By conducting routine analysis of the Groundhog pyrite during a session, instrument performance and major variations in transport efficiency were monitored.

All reduction of raw ICP–MS data was performed in a spreadsheet using linear relationships. The instrument mass counts for a given element were converted to an absolute concentration by normalization to an "ablation efficiency factor." The ablation efficiency factor was calculated for each analysis by ratio of the measured sum of all concentrations to 100 percent or in some cases by ratio of the measured concentration of a single major element (such as iron) based on the assumption

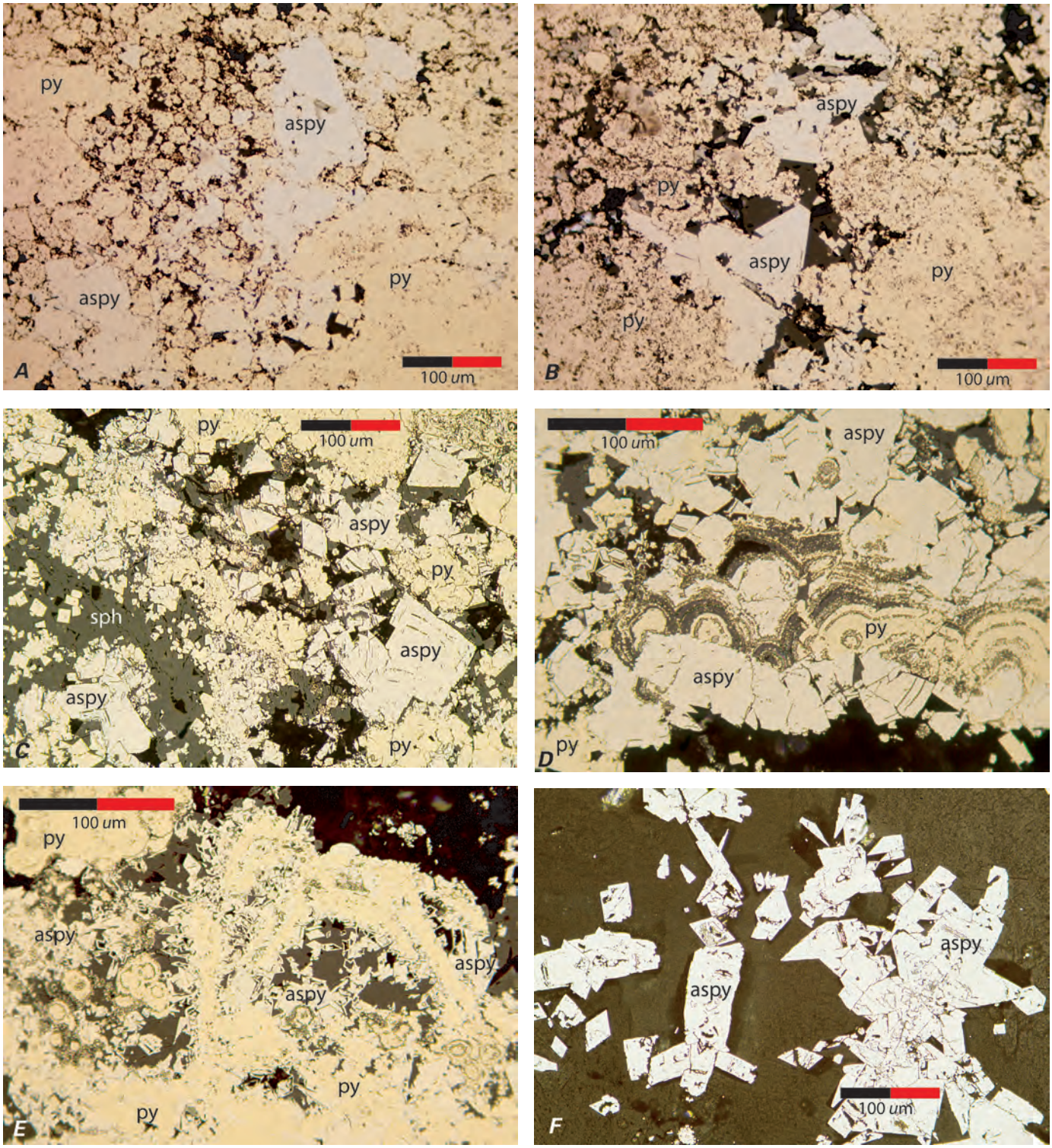

Figure 7. Photomicrographs of arsenian pyrite and arsenopyrite in polished thin sections: (*A*–*C*) euhedral arsenian pyrite and arsenopyrite (aspy) replacing framboidal and spongy-textured pyrite (*A* and *B*: drill-core sample GC1643–03, 119.5′, 200 South orebody, *C*: rib sample 96GC–17, 49′, 344 crosscut, Lower Southwest orebody); (*D*) subhedral to euhedral crystals of arsenian pyrite and arsenopyrite overgrowing colloform pyrite (rib sample 96GC–17, 49′, 344 crosscut, Lower Southwest orebody); (*E*) euhedral arsenian pyrite and arsenopyrite overgrowing and replacing framboidal and atoll-shaped pyrite (rib sample 96GC–17, 49′, 344 crosscut, Lower Southwest orebody); and (*F*) euhedral arsenopyrite in silica and dolomite matrix (rib sample 96GC–18, 51′, 344 crosscut, Lower Southwest orebody).

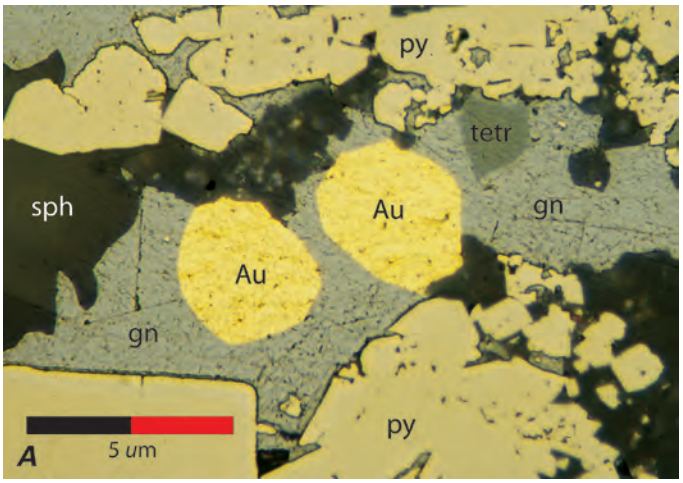
py
tetr
sph
Au
gn
Au
gn
py
5 um
A

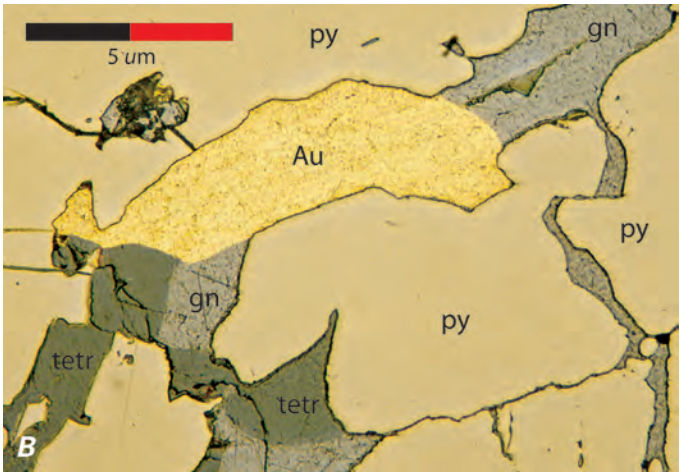
5 um
py
gn
Au
py
gn
py
tetr
tetr
B

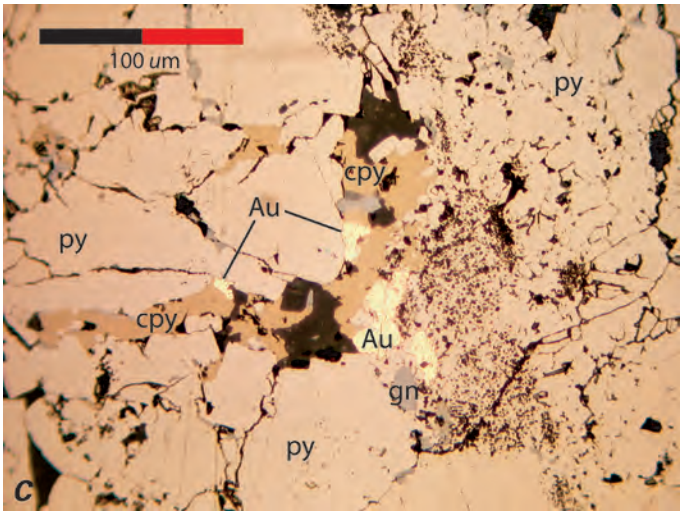
100 um
py
cpy
Au
py
cpy
Au
gn
py
C

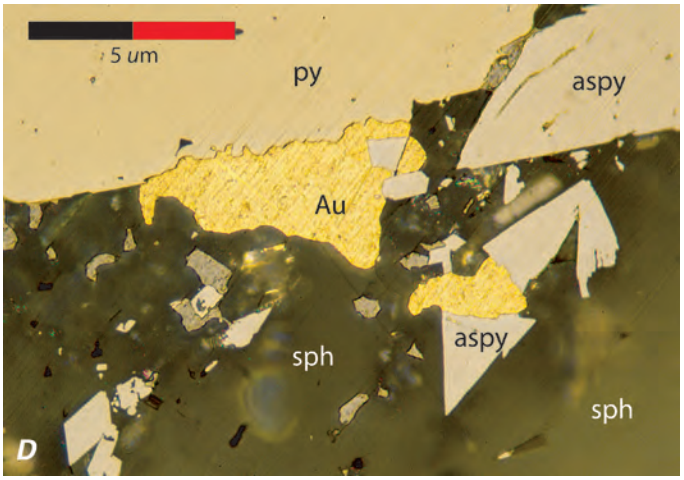
5 um
py
aspy
Au
sph
aspy
sph
D

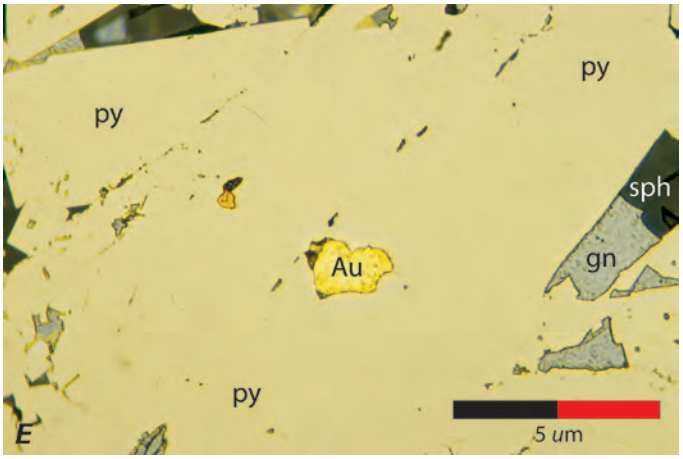
py
py
sph
Au
gn
py
5 um
E

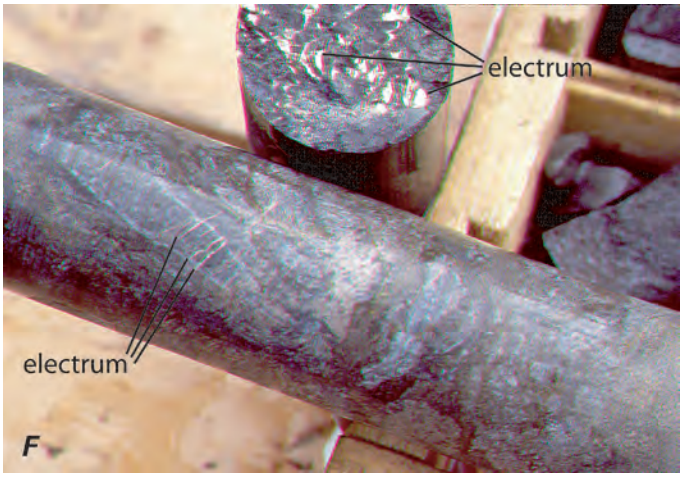
electrum
electrum
F

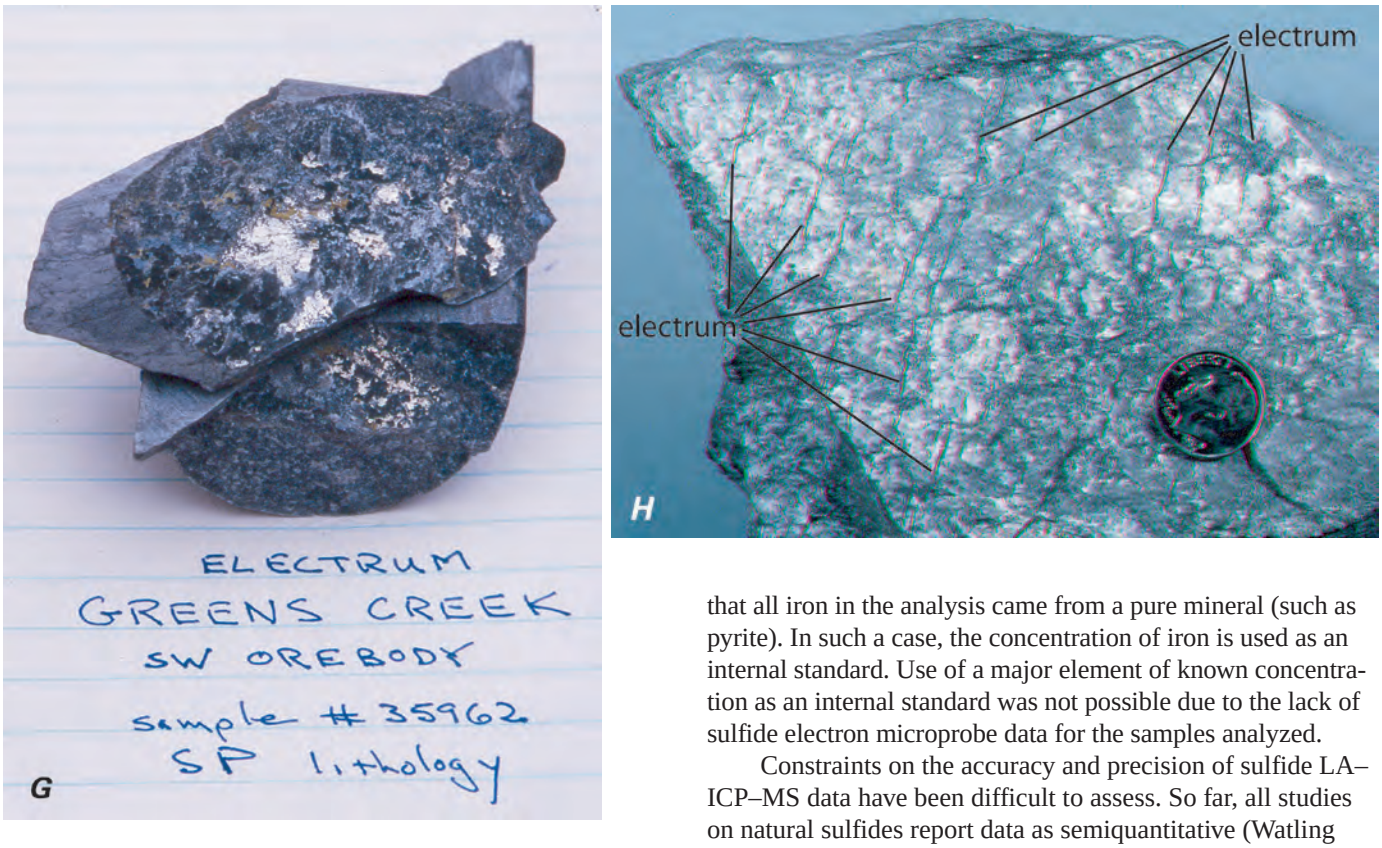

Figure 8 (above and facing page). Photographs and photomicrographs of free gold (Au) in hand samples and polished sections: (*A*) rounded grains of yellow gold in matrix of sphalerite (sph), galena (gn), and tetrahedrite (tetr) (rib sample 96GC–13, 25.5′, 344 crosscut, Lower Southwest orebody); (*B*) large grain of yellow gold, and galena and tetrahedrite filling crack in massive recrystallized pyrite (rib sample 96GC–16, 43.5′, 344 crosscut, Lower Southwest orebody); (*C*) bright yellow gold, chalcopyrite, sphalerite, and galena in a veinlet cutting recrystallized pyrite (drill-core sample GC1643–06, 119.5′, 200 South orebody); (*D*) grains of yellow gold in contact with pyrite and arsenopyrite (aspy) (rib sample 96GC–19, 53′, 344 crosscut, Lower Southwest orebody); (*E*) yellow gold included within clean, recrystallized pyrite (rib sample 96GC–13, 25.5′, 344 crosscut, Lower Southwest orebody); (*F* and *G*) silver-white electrum filling fractures and coating fracture surfaces in drill core (GC1155, 319.5′, Lower Southwest orebody); and (*H*) hand sample showing electrum in thin veinlets and spaced sheets that occupy fractures up to 0.5 millimeter wide (rib sample, 30 East decline, 650′ level, East orebody). These fractures are paragenetically late and appear to be tension gashes and piercement structures that occur at high angles to S2 foliation.

that all iron in the analysis came from a pure mineral (such as pyrite). In such a case, the concentration of iron is used as an internal standard. Use of a major element of known concentration as an internal standard was not possible due to the lack of sulfide electron microprobe data for the samples analyzed.

Constraints on the accuracy and precision of sulfide LA–ICP–MS data have been difficult to assess. So far, all studies on natural sulfides report data as semiquantitative (Watling and others, 1995; Viets and others, 1996; Butler and Nesbitt, 1999; J.L. Houghton, W.C. Shanks, and W.E. Seyfried, written commun., 2003). Major reasons for this include poorly quantified differences in ablation efficiency of different sulfides, a near universal lack of appropriate natural or synthetic sulfide calibration standards, and poorly characterized matrix effects that arise as a result of using glass or pressed powder standards. Careful work on glass standards using microprobe data to provide internal standard elemental concentrations has demonstrated that current LA–ICP–MS instrumentation is capable of 2–5 percent accuracy and precision (Norman and others, 1996). Similar careful studies of trace elements in NiS beads, a matrix similar to natural sulfides, document much wider error limits; Shibuya and others (1998) report better than 17 percent accuracy for platinum-group elements and gold, and Guo and Lichte (1995) report between 2 and 12 percent accuracy for chalcophile elements. For an excellent discussion of error analysis of LA–ICP–MS data, see Norman and others (1996).

The data in this study are preliminary and, although absolute concentrations are presented, the results should be evaluated semiquantitatively. Major sources of uncertainty in these data include the lack of independently determined internal element concentrations, thus requiring the assumption of pure mineral species, the reliance on glass standards for calibration, the unknown volume of ablated material, the various differences in elemental fractionations and mineral ablation efficiencies, and finally, the uncertainty of target mineral purity due to the relatively large size of the ablation crater compared with the size of many of the mineral grains. This last feature is perhaps the largest of all the uncertainty factors.

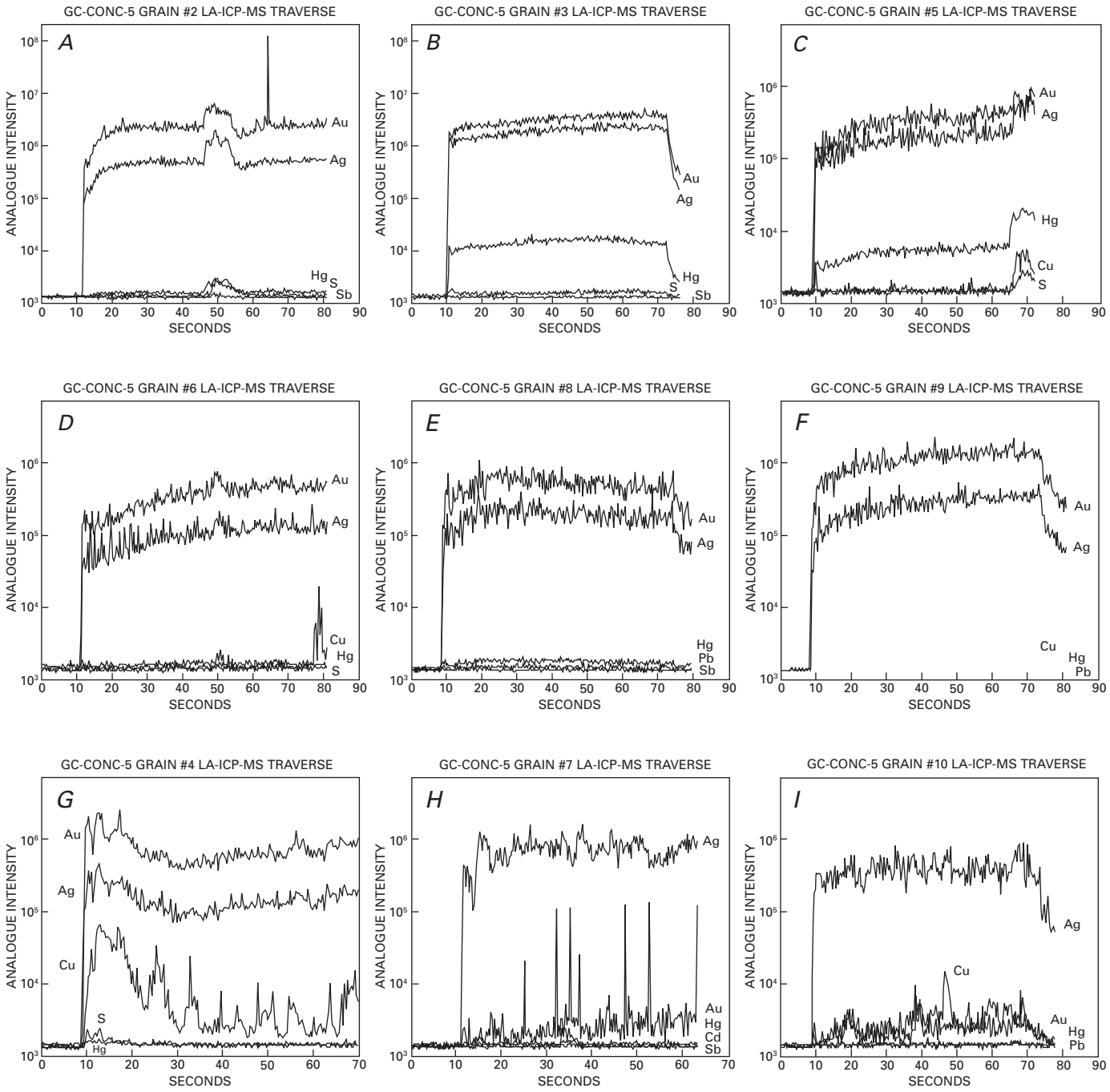

Figure 9. LA–ICP–MS traverses across heavy concentrate grains recovered from the Greens Creek mill. All grains analyzed are from the coarsest fraction of sample GC–CONC–5. Each profile was obtained by operating the laser in continuous mode across a traverse of approximately 100 micrometers with the ICP–MS detectors set to record the relative abundances, measured as the $\log_{10}$ of analogue intensity, of five selected elements. Each plot exhibits the relative abundances of the elements selected and shows the variation in relative concentration with time (distance along the traverse). Note that plots *A* and *B* have a greater y-axis range than plots *C–I*. Plots a and b exhibit the two types of gold identified at Greens Creek: yellow gold of high fineness and silver-white electrum composed of an amalgam of gold, silver, and mercury. Plot *C* is an example of electrum, plots *D–F* are analyses of yellow gold grains, plot g represents a possible copper-rich variant of yellow gold, and plots h and i are examples of nearly pure native silver grains. (*A*) grain #2, Au and Ag only, high Au/Ag; (*B*) grain #3, Au, Ag, and Hg, lower Au/Ag; (*C*) grain #5, Au, Ag, and Hg, lower Au/Ag; (*D*) grain #6, Au and Ag, high Au/Ag; (*E*) grain #8, Au and Ag, high Au/Ag; (*F*) grain #9, Au and Ag, high Au/Ag; (*G*) grain #4, Au, Ag, and Cu, high Au/Ag; (*H*) grain #7, nearly pure Ag; and (*I*) grain #10, nearly pure Ag.

Results

Progressive recrystallization of the primary-textured ores and the remobilization of base-metal sulfides have had a profound effect on the siting of trace elements in the ores. LA–ICP–MS studies indicate that a wide range of trace elements is present in the major primary-textured sulfide minerals at relatively high concentrations (fig. 11). As the recrystallization process progresses, trace-element abundances decrease in later formed pyrites and increase predictably in recrystallized and remobilized base-metal sulfides. A second result of the metamorphic refining process is a decrease in the variety of intermediate solid solution sulfosalt minerals and the formation of a less diverse mineral assemblage with a greater proportion of the trace elements contained in discrete end-member mineral phases such as sphalerite and tetrahedrite.

The data from the LA–ICP–MS analyses are presented in tables 2–7. These tables contain data on selected trace-element abundances in primary-textured pyrite, recrystallized pyrite, arsenian pyrite, galena, sphalerite, and tetrahedrite. Plots showing the changes in major- and trace-element concentrations in pyrite, sphalerite, and galena with modification from primary to recrystallized and remobilized textures are shown in figures 12a–ay. Tables 8–10 contain data on primary-textured, recrystallized, and remobilized mixed mineral aggregates. Even though these data are considered semiquantitative for the reasons discussed, the order of magnitude differences in trace-element concentrations within these data reflects usable information on the relative abundances and siting of trace elements in minerals and on the range of trace-element abundances in the various major types of ores present at Greens Creek. These data are discussed below.

Typical trace-element abundances in primary-textured ores as determined by LA–ICP–MS are difficult to interpret due to the fine-scale banding and grain sizes present in the framboidal aggregates and colloform textures. In most cases, the 50-mm beam size of the instrument is incapable of acquiring data from single phases within these ores. Smaller beam size would result in higher limits of detection because the amount of material sampled varies with the square of the crater diameter. Thus, there is a tradeoff between detectability and sampling integrity for these fine-grained minerals. However, data from a limited number of analyses of primary-textured pyrite (mostly spongy pyrite; table 2) and primary-textured ores of mixed mineralogy (table 8) provide a baseline against which to compare analyses of discrete recrystallized or remobilized grains. Typical trace-element abundances in primary-textured pyrite and mixed primary-textured ores are: gold at <240 parts per billion (ppb), silver commonly in the hundreds of parts per million (ppm) and as high as 19,400 ppm, and arsenic at 0.1–4.8 percent. Antimony is clearly the dominant trace element present ubiquitously in the primary-textured pyritic ores near the 1 percent level, and rises to the 9 percent level. Thallium is present in primary ores in the hundreds of parts per million and rises as high as 2,300 ppm. Molybdenum is present from the hundreds to several thousand parts per million and rises as high as 11,930 ppm.

LA–ICP–MS analyses of recrystallized and remobilized phases demonstrate that trace elements are predictably concentrated in fewer, more stoichiometrically ordered minerals. After free gold, the next consistently high concentrations of gold, up to 2,613 ppb, occur in arsenian pyrite (table 4). Gold is inhomogeneously distributed, tends to be concentrated near the edges of euhedral grains, and is probably present as discrete, submicrometer inclusions within the recrystallized pyrite/arsenopyrite. The next most obvious residence of gold, at the 0–700-ppb range with a high of 5,401 ppb, is in the secondary masses of sphalerite and tetrahedrite (table 9). The relatively uniform distribution of gold in these phases suggests that it forms a solid solution rather than occurring as inclusions (fig. 12y). Silver is present in pyrargyrite and in secondary tetrahedrite at 2.9 to 6.7 percent (table 7). Grains of other secondary silver-bearing minerals known to be present at Greens Creek of a size large enough to analyze were not found. Other silver-bearing minerals are recrystallized and remobilized "clean" crystals of pyrite, arsenian pyrite/arsenopyrite, and galena that typically contain hundreds of parts per million and as high as 3,740 ppm (table 5; fig. 12ao). The silver content of sphalerite is extremely variable but generally low. Copper is present in chalcopyrite and in tetrahedrite up to 47 percent, and zinc is present in tetrahedrite at 2.4–7.7 percent (table 7). Arsenic is present in arsenian pyrite/arsenopyrite at the 19–24 percent level (table 4), and in late tetrahedrite in the 2.4–10.2 percent range. Recrystallized pyrite and large secondary anhedral grains of sphalerite and galena typically have less than 0.5 percent arsenic, with maximum values of 1.9 percent. Antimony is a major component of tetrahedrite, is present at 7.6–28 percent and is clearly the dominant and ubiquitous trace element present in Greens Creek ores. It is present at more than 1,000 ppm in every mineral examined with the exceptions of recrystallized pyrite and secondary sphalerite (figs. 12f, w, and aj). Mercury is present at the 58–2,390-ppm level in secondary sphalerite and tetrahedrite and is lowest in secondary galena and arsenian pyrite (figs. 12i, z, and aq). Thallium is present in secondary galena to just less than 1.2 percent (table 5, fig. 12ar). Cadmium is present in sphalerite up to 2,731 ppm. Chromium, cobalt, and nickel are ubiquitous and appear to be associated. These elements occur routinely at levels of tens to hundreds of parts per million in all minerals and ore types. Note that their concentrations are very similar in primary and recrystallized phases but tend to drop to low abundances in the remobilized phases (figs. 12n, o, p, ae, af, ag, av, aw, and ax; tables 8–10). Bismuth, a trace element that is commonly enriched in sulfosalt-bearing massive sulfide deposits, occurs in notably low concentrations in Greens Creek ores. Selenium occurs in all ore types up to 6,000 ppm and is present at 1.1 percent and 1.8 percent in recrystallized pyrite and sphalerite, respectively. Interestingly, the distribution of selenium is generally antithetic to that of antimony, which is notably low in recrystallized pyrite and sphalerite. Selenium shares a distribution similar to chromium, cobalt, and nickel.

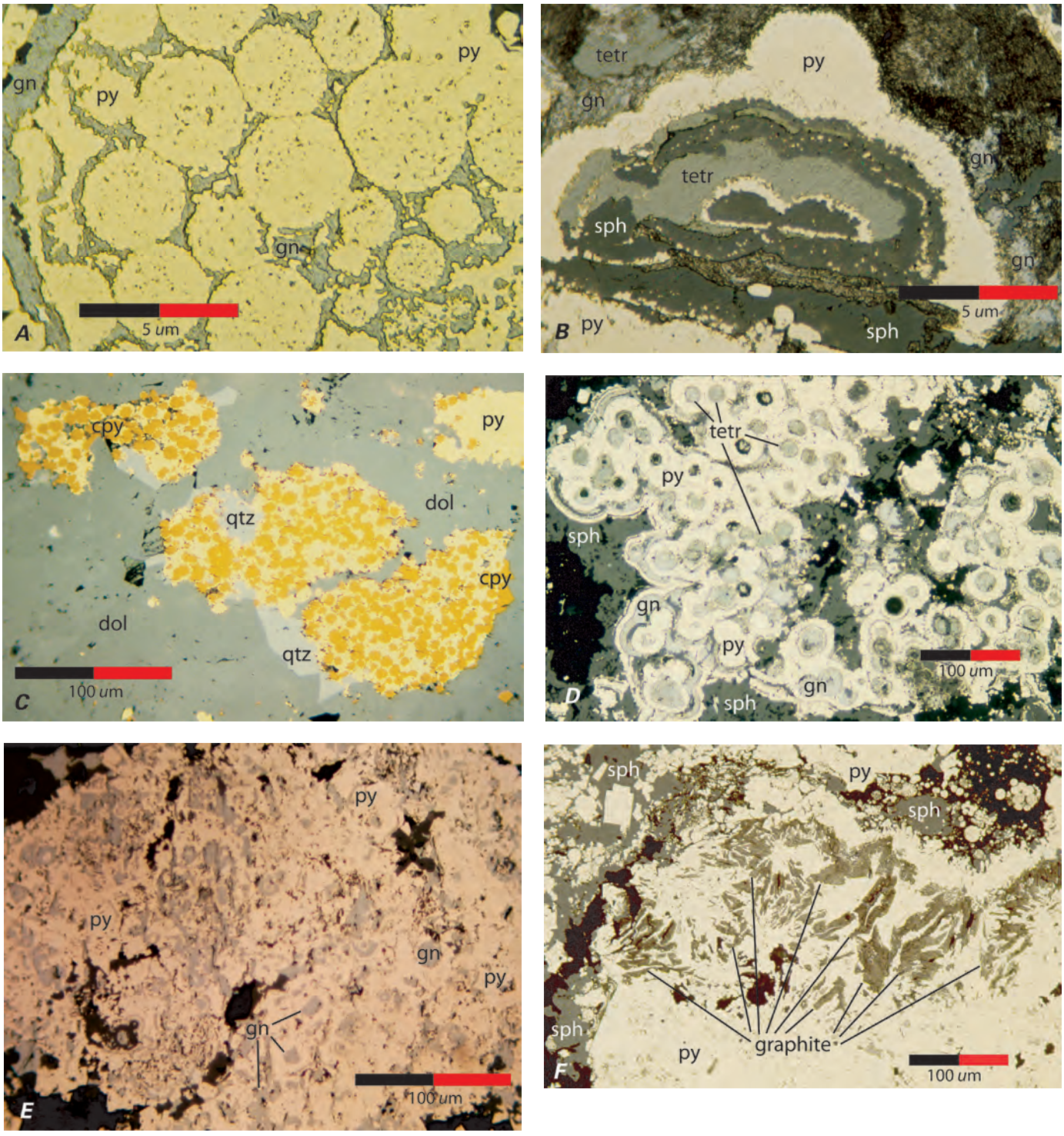

Figure 10 (above and facing page). Photographs and photomicrographs showing textural relationships in Greens Creek ores: (*A*) polyframboidal pyrite aggregate in galena or lead-antimony sulfosalt matrix (rib sample 96GC–12, 21.5′, 344 crosscut, Lower Southwest orebody); (*B*) successive bands of colloform-textured base-metal sulfides without intervening pyrite bands, within predominantly pyritic primary textured masses (rib sample 96GC–16, 43.5′, 344 crosscut, Lower Southwest orebody); (*C*) framboids composed of chalcopyrite crystallites in a matrix of pyrite, quartz, and dolomite (drill-core sample GC1527–15, 454.2′, Northwest orebody); (*D*) incipient recrystallization of individual framboids resulting in atoll-shaped grains, with centers filled with base-metal sulfides and rims of clean, bright pyrite (drill-core sample GC1527–09, 402.5′, Northwest orebody); (*E*) an aggregate of framboids developed into a large, spongy-textured mass with numerous discrete inclusions of base-metal sulfides and graphite (drill-core sample GC1643–05, 100.5′, 200 South orebody); (*F*) a felty concentration of

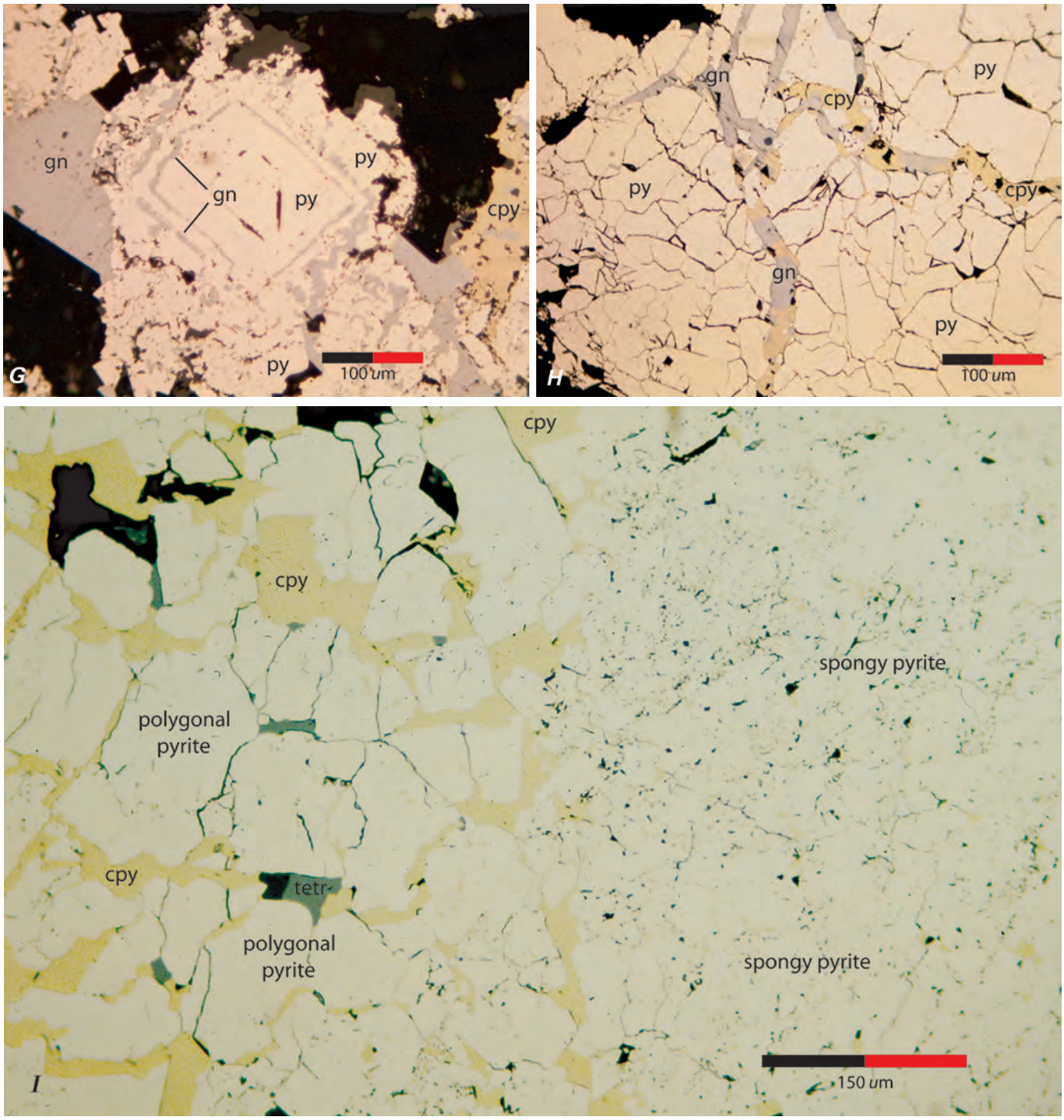

needle- or lath-shaped crystals of recrystallized graphite that are aligned subparallel to S2 foliation (rib sample 96GC–16, 43.5′, 344 crosscut, Lower Southwest orebody); (*G*) progressive recrystallization showing a large area of inclusion-free pyrite with relict framboidal shapes preserved in the interior of the mass and euhedral-shaped growth zones defined by thin bands of galena (drill-core sample GC1643–07, 143.5′, 200 South orebody); (*H*) fully recrystallized pyritic ore showing very large areas of inclusion-free, monomineralic pyrite with polygonal grain boundaries cut by chalcopyrite-galena-tetrahedrite veinlets (drill-core sample GC1643–04, 75′, 200 South orebody); and (*I*) chalcopyrite-rich MFP showing the progression from spongy-textured masses with chalcopyrite matrix and numerous small chalcopyrite inclusions on the right, to clean, monomineralic, polygonal-textured masses of pyrite with grain boundaries and intercrystal spaces filled with anhedral, monomineralic chalcopyrite on the left (drill-core sample GC1527–14, 447.2′, Northwest orebody).

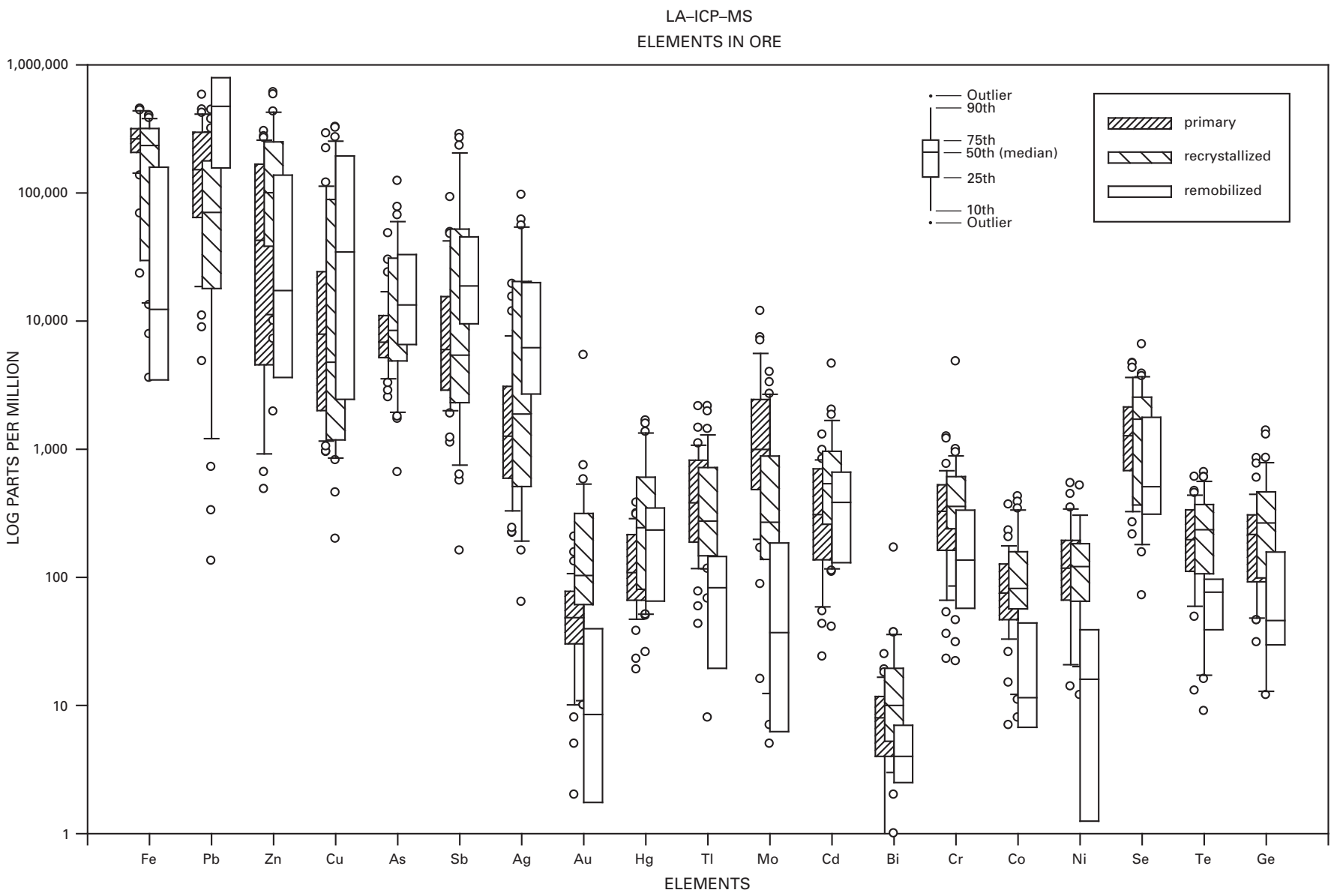

Figure 11. Summary LA–ICP–MS data on sulfide ore minerals in the Greens Creek deposit. Box plots of percentiles shows the $\log_{10}$ concentration range for primary, recrystallized, and remobilized ore textures for each of 19 elements. All elements measured in parts per million, except gold, which is in parts per billion. Horizontal lines within each box show the geometric mean (median value). Each box extends from the 25th to the 75th percentile, whiskers extend out to the 5th and 95th percentiles, and the open or closed circles show individual outlier values. Data plotted from data in tables 2–10.

Table 2. Trace-element composition of primary pyrite as determined by Laser Ablation–Inductively Coupled Plasma–Mass Spectroscopy analyses.

Sample #	Fe %	Pb %	As %	Sb %	Zn ppm	Cu ppm	Ag ppm	Au ppb	Hg ppm	Tl ppm	Mo ppm	Cd ppm	Bi ppm	Cr ppm	Co ppm	Ni ppm	Se ppm
96GC-25	34.8	16.9	0.6	0.2	25,166	4,400	765	49	66	591	2,585	77	6	81	101	280	670
96GC-25	44.1	1.1	0.7	0.6	1,484	13,826	1,929	45	85	107	48	31	3	146	0	119	1,081
96GC-25	35.4	19.9	0.3	0.1	538	683	2,400	39	65	2,304	524	26	1	181	39	221	127
96GC-25	30.9	17.8	0.8	1.1	46,813	23,025	3,217	74	123	1,067	2,703	167	9	96	78	216	0
96GC-25	32.3	16.3	1.1	0.4	56,832	7,009	1,302	47	129	1,072	2,284	196	2	199	102	387	0
96GC-25	44.8	1.3	0.1	0.1	12,694	1,193	338	240	71	37	235	49	12	137	71	123	1,157
96GC-25	24.8	35.0	0.6	0.5	15,711	12,122	2,101	55	45	535	2,562	80	15	411	262	251	3,565
96GC-25	36.6	10.6	1.3	0.8	17,645	22,264	4,027	82	123	1,433	1,747	136	8	848	185	240	446
96GC-25	35.7	17.4	0.6	0.3	3,201	6,242	1,310	124	37	1,270	2,396	146	20	566	248	369	3,411
96GC-25	42.9	4.1	1.5	0.3	862	223	291	31	30	690	115	118	3	598	125	256	1,662
mean	36.2	14.1	0.8	0.4	18,095	9,099	1,768	79	77	911	1,520	103	8	326	121	246	1,212
std. deviation	6.3	10.3	0.4	0.3	19,758	8,469	1,220	63	36	675	1,145	59	6	264	86	88	1,316
maximum	44.8	35.0	1.5	1.1	56,832	23,025	4,027	240	129	2,304	2,703	196	20	848	262	387	3,565
minimum	24.8	1.1	0.1	0.1	538	223	291	31	30	37	48	26	1	81	0	119	0

Table 3. Trace-element composition of recrystallized pyrite as determined by Laser Ablation–Inductively Coupled Plasma–Mass Spectroscopy analyses.

	Fe	As	Pb	Zn	Cu	Sb	Ag	Au	Hg	Tl	Mo	Cd	Bi	Cr	Co	Ni	Se
Sample #	%	%	ppm	ppm	ppm	ppm	ppm	ppb	ppm	ppm	ppm	ppm	ppm	ppm	ppm	ppm	ppm
96GC-18	45.8	0.4	1,076	2,031	541	948	307	33	42	109	78	78	14	476	60		2,438
96GC-18	45.7	0.1	53	1,513	2,003	228	518	0	25	30	235	52	15	610	467		9,864
96GC-18	43.4	1.5	2,230	6,211	553	9,743	850	222	190	1,109	194	228	0	990	181		11,136
96GC-18	46.1	0.2	708	1,239	902	435	76	50	24	37	155	49	14	340	0		1,783
96GC-18	45.3	0.3	2,292	521	399	8,945	126	20	212	1,080	120	70	5	484	212		4,855
96GC-18	44.8	0.3	744	2,790	700	6,995	687	103	146	912	253	223	29	912	447		10,589
96GC-18	45.7	0.5	95	0	224	229	360	66	0	36	41	119	39	326	330		6,427
96GC-19	44.0	1.7	11,570	9,812	55	330	100	54	23	123	62	51	9	195	10		890
96GC-19	46.3	0.1	786	1,474	446	0	80	20	32	50	170	114	5	255	118		1,350
96GC-19	45.5	0.6	7,563	1,141	349	49	110	45	31	91	84	44	12	392	96		3,108
96GC-19	46.3	0.1	1,430	0	721	94	123	0	23	68	38	45	2	416	115		2,378
96GC-19	46.3	0.3	584	1,121	153	60	78	16	32	26	40	487	18	466	48		342
96GC-19	43.9	0.4	4,704	28,550	2,578	156	66	56	47	0	0	270	12	549	105		350
mean	45.3	0.5	2,603	4,339	740	2,170	268	53	64	282	113	141	13	493	169	0	4,270
std. deviation	1.0	0.5	3,423	7,778	737	3,697	263	58	70	432	82	130	11	233	155	0	3,964
maximum	46.3	1.7	11,570	28,550	2,578	9,743	850	222	212	1,109	253	487	39	990	467	0	11,136
minimum	43.4	0.1	53	0	55	0	66	0	0	0	0	44	0	195	0	0	342

Table 4. Trace-element composition of arsenian pyrite as determined by Laser Ablation–Inductively Coupled Plasma–Mass Spectroscopy analyses.

Sample #	Mineral texture	Fe %	Zn %	As %	Sb %	Pb ppm	Cu ppm	Ag ppm	Au ppb	Hg ppm	Tl ppm	Mo ppm	Cd ppm	Bi ppm	Cr ppm
96GC-18	recrystallized	25.0	3.3	24.1	0.5	4,285	1,258	361	95	59	24	4,061	233	7	296
96GC-19	recrystallized	30.9	0.8	18.9	0.2	647	349	2,478	2,613	9	32	158	71	9	571
96GC-19	recrystallized	26.8	2.3	23.0	0.3	620	577	225	1,172	14	48	1,566	256	10	564
mean		27.6	2.1	22.0	0.4	1,851	728	1,021	1,294	27	35	1,928	187	9	477
std. deviation		3.0	1.3	2.7	0.2	2,109	473	1,264	1,263	28	12	1,977	101	2	157
maximum		30.9	3.3	24.1	0.5	4,285	1,258	2,478	2,613	59	48	4,061	256	10	571
minimum		25.0	0.8	18.9	0.2	620	349	225	95	9	24	158	71	7	296

Table 5. Trace-element composition of galena as determined by Laser Ablation–Inductively Coupled Plasma–Mass Spectroscopy analyses.

Sample #	Mineral texture	Pb %	Sb %	Fe ppm	Zn ppm	Cu ppm	As ppm	Ag ppm	Au ppb	Hg ppm	Tl ppm	Mo ppm	Cd ppm	Bi ppm	Cr ppm	Co ppm	Ni ppm	Se ppm
96GC-26b	primary	75.7	3.2	3,513	36,069	176	14,015	234	12	56	124	27	47	3	143	38	20	894
96GC-26b	primary	78.3	3.0	2,767	619	4,810	6,435	37	11	22	327	35	24	3	103	47	56	495
96GC-19	recrystallized	84.1	0.3	4,557	845	79	114	891	19	16	11,724	30	12	4	269	91		2,364
96GC-19	recrystallized	84.8	0.3	687	888	117	135	773	10	16	11,558	19	31	2	244	90		2,047
96GC-19	recrystallized	85.5	0.2	153	420	76	331	518	5	11	8,515	28	29	3	166	52		1,263
96GC-19	recrystallized	85.5	0.3	0	271	122	232	749	8	11	8,275	31	24	4	174	57		1,419
96GC-19	recrystallized	85.4	0.3	97	512	137	266	761	3	14	8,654	46	26	4	257	45		1,412
96GC-19	recrystallized	85.4	0.3	418	271	114	498	640	22	15	8,597	18	0	2	175	44		920
96GC-19	recrystallized	85.2	0.3	903	480	62	556	791	2	14	8,655	36	35	2	177	63		1,508
96GC-26b	remobilized	86.5	0.2	196	84	154	728	222	1	60	11	3	13	2	41	7	15	282
96GC-26b	remobilized	79.4	4.1	270	75	83	18,801	97	9	49	237	5	52	1	5	4	2	345
96GC-26b	remobilized	79.9	3.6	3,102	1,252	95	14,793	85	3	23	152	27	14	1	19	6	6	157
96GC-26b	remobilized	82.9	0.7	2,151	3,012	10,970	5,118	3,740	6	88	11	17	55	1	40	6	18	191
mean		83.0	1.3	1,447	3,446	1,307	4,771	734	9	30	5,142	25	28	2	139	42	20	1,023
std. deviation		3.5	1.5	1,565	9,832	3,181	6,719	955	6	25	4,935	12	16	1	91	30	19	719
maximum		86.5	4.1	4,557	36,069	10,970	18,801	3,740	22	88	11,724	46	55	4	269	91	56	2,364
minimum		75.7	0.2	0	75	62	114	37	1	11	11	3	0	1	5	4	2	157

Table 6. Trace-element composition of sphalerite as determined by Laser Ablation–Inductively Coupled Plasma–Mass Spectroscopy analyses.

Sample #	Mineral texture	Zn %	Fe ppm	Pb ppm	Cu ppm	As ppm	Sb ppm	Ag ppm	Au ppb	Hg ppm	Tl ppm	Mo ppm	Cd ppm	Bi ppm	Cr ppm	Co ppm	Ni ppm	Se ppm
96GC-25	primary	35.4	159,769	98,166	3,170	4,939	1,813	650	41	58	161	1,899	376	5	163	66	34	661
96GC-25	primary	35.1	155,144	68,913	30,489	5,855	8,637	2,637	50	742	42	368	396	6	671	51	33	1,031
96GC-19	recrystallized	62.6	7,064	18,788	100	843	314	588	375	371	314	247	2,729	41	2,021	556		13,751
96GC-19	recrystallized	62.7	7,673	12,170	454	404	474	645	365	401	245	154	2,570	9	1,629	571		16,271
96GC-19	recrystallized	65.8	4,780	152	822	219	270	98	601	1,115	277	119	2,707	27	543	151		0
96GC-19	recrystallized	62.0	9,138	16,250	589	779	392	821	448	521	342	346	2,731	23	1,692	745		18,277
96GC-19	recrystallized	63.4	2,702	5,517	4,100	5,199	9,766	1,256	644	1,142	361	133	2,438	20	603	246		5,615
96GC-19	recrystallized	65.3	5,546	169	556	272	179	262	697	1,301	347	224	2,227	24	805	144		4,674
96GC-19	recrystallized	65.5	5,420	78	0	0	99	187	717	1,184	350	175	2,292	15	1,366	127		3,199
96GC-19	recrystallized	57.1	19,407	128	646	504	176	78,422	772	1,351	304	117	1,301	4	706	198		2,106
96GC-25	recrystallized	62.4	12,227	15,494	4,968	1,320	7,562	1,734	55	1,581	36	57	625	10	225	101	126	885
96GC-26b	recrystallized	64.6	1,589	17,558	962	685	558	86	94	2,390	58	87	1,045	22	593	165	97	2,383
mean		58.5	32,538	21,115	3,905	1,752	2,520	7,282	405	1,013	236	327	1,786	17	918	260	72	5,738
std. deviation		11.1	58,545	30,718	8,534	2,194	3,756	22,416	285	639	128	504	962	11	606	230	46	6,529
maximum		65.8	159,769	98,166	30,489	5,855	9,766	78,422	772	2,390	361	1,899	2,731	41	2,021	745	126	18,277
minimum		35.1	1,589	78	0	0	99	86	41	58	36	57	376	4	163	51	33	0

Table 7. Trace-element composition of tetrahedrite as determined by Laser Ablation–Inductively Coupled Plasma–Mass Spectroscopy analyses.

Sample #	Mineral texture	Fe %	Zn %	Cu %	As %	Sb %	Ag %	Pb ppm	Au ppb	Hg ppm	Tl ppm	Mo ppm	Cd ppm	Bi ppm	Cr ppm	Co ppm	Ni ppm	Se ppm
96GC-18	recrystallized	3.9	2.4	37.5	2.9	21.1	6.2	270	429	804	141	35	805	2	71	52		1,382
96GC-19	recrystallized	1.5	4.0	33.4	2.7	27.5	5.9	226	311	485	92	48	990	5	167	83		831
96GC-19	recrystallized	5.3	3.7	32.9	4.1	21.2	4.6	145	474	566	152	67	931	11	546	136		5,174
96GC-19	recrystallized	1.8	3.3	34.3	2.9	27.1	5.5	892	291	513	132	16	981	3	344	43		1,261
96GC-19	recrystallized	1.4	4.9	33.9	2.4	27.2	5.3	183	243	416	123	80	954	4	282	23		1,081
96GC-19	recrystallized	1.6	3.7	34.0	2.5	27.8	5.5	162	301	545	95	22	984	8	286	57		854
96GC-19	recrystallized	2.0	3.6	36.5	4.1	22.9	5.0	98	409	506	163	111	730	11	606	164		6,009
96GC-19	recrystallized	1.9	3.8	35.8	4.2	23.4	5.1	146	472	600	223	127	838	5	811	220		3,703
96GC-25	recrystallized	3.1	4.1	38.3	7.7	13.0	6.7	6,741	58	879	67	71	808	3	32	18	9	114
96GC-25	recrystallized	3.1	4.2	40.5	9.7	10.7	4.4	3,542	16	775	51	391	980	4	0	28	50	480
96GC-25	recrystallized	3.6	4.6	38.5	10.2	8.9	4.2	28,714	32	781	47	164	903	2	119	17	68	494
96GC-25	recrystallized	1.7	7.7	47.1	6.5	7.6	2.9	10,519	97	1,273	93	66	210	5	79	67	68	207
96GC-25	remobilized	2.8	4.0	38.1	7.0	12.9	5.7	34,783	20	894	24	40	1,144	0	370	40	103	2,565
mean		2.6	4.2	37.0	5.2	19.3	5.2	6,648	242	695	108	95	866	5	286	73	60	1,858
std. deviation		1.2	1.2	3.8	2.8	7.6	1.0	11,653	178	237	55	99	224	3	247	63	34	1,935
maximum		5.3	7.7	47.1	10.2	27.8	6.7	34,783	474	1,273	223	391	1,144	11	811	220	103	6,009
minimum		1.4	2.4	32.9	2.4	7.6	2.9	98	16	416	24	16	210	0	0	17	9	114

Table 8. Trace-element composition of mixed primary-textured mineral aggregates as determined by Laser Ablation–Inductively Coupled Plasma–Mass Spectroscopy analyses.

Sample #	Mineralogy	Fe %	Pb %	Zn %	Cu %	As %	Sb %	Ag ppm	Au ppb	Hg ppm	Tl ppm	Mo ppm	Cd ppm	Bi ppm	Cr ppm	Co ppm	Ni ppm	Se ppm
96GC-25	?	31.6	20.1	0.4	1.1	1.0	4.0	1,203	60	38	399	4,973	43	1	139	62	174	677
96GC-25	?	22.6	33.8	2.5	3.0	1.3	1.6	5,871	47	86	768	11,930	223	6	195	42	130	782
96GC-25	?	29.1	28.2	0.4	1.2	0.9	0.4	2,097	55	105	979	7,026	143	19	764	368	541	4,295
96GC-25	gn-gcr	22.0	42.0	1.2	0.7	0.5	0.3	1,425	91	23	633	3,533	54	10	246	131	128	2,058
96GC-26b	gn-py-tetr-sph	14.6	41.0	6.4	6.2	1.4	0.9	3,125	5	88	157	169	417	8	383	38	34	1,719
96GC-25	gn-tetr	2.3	58.0	0.9	12.0	3.0	3.7	15,427	11	314	77	16	218	0	23	7	14	446
96GC-25	gn-tetr	27.0	20.1	1.7	11.0	0.6	0.8	3,605	78	66	324	3,704	163	8	419	70	288	694
96GC-25	py-gn	34.3	17.5	0.5	1.9	0.8	0.8	5,224	32	56	1,059	898	62	3	53	106	445	351
96GC-25	py-gn	31.3	16.2	3.6	0.9	0.7	4.8	1,764	70	86	693	2,092	158	8	105	36	60	267
96GC-25	py-gn	26.0	36.6	0.1	0.5	0.5	0.2	936	64	19	174	210	61	3	287	81	78	555
96GC-25	py-gn-qtz	27.2	35.0	0.0	0.1	0.6	0.1	644	81	53	839	618	75	7	159	46	118	215
96GC-26b	py-gn-sph	20.3	36.2	7.7	0.2	0.6	1.4	670	28	81	240	1,248	250	2	238	46	0	843
96GC-26b	py-gn-sph	16.5	30.3	17.5	1.2	0.5	0.7	2,371	41	189	612	492	731	7	534	52	78	912
96GC-26b	py-gn-tetr-sph	19.4	28.0	12.4	2.2	1.1	1.7	2,663	2	250	232	458	617	12	594	82	67	2,889
96GC-26b	py-gn-tetr-sph	22.1	13.6	20.0	2.5	0.8	1.1	2,999	16	215	270	990	834	10	1,250	108	81	4,695
96GC-25	py-qtz	31.8	18.2	0.4	4.3	1.3	1.3	5,271	156	85	2,155	804	135	6	285	156	204	729
96GC-25	py-sph	31.1	7.9	14.5	0.6	0.5	0.3	998	49	121	312	4,293	387	10	1,202	127	331	2,703
96GC-25	py-sph-gn	28.2	14.1	14.4	0.5	0.4	0.2	846	43	164	429	1,736	347	6	160	42	153	669
96GC-26b	py-sph-gn	14.8	44.6	8.8	0.3	0.5	1.8	690	15	165	312	435	370	8	369	58	66	996
96GC-26b	py-sph-gn	34.9	5.9	11.4	0.2	0.3	0.3	487	32	113	134	606	392	11	381	51	190	1,569
96GC-26b	py-sph-gn	27.3	11.3	17.8	0.2	0.4	0.5	578	39	206	301	1,037	817	4	482	53	199	1,289
96GC-26b	py-sph-gn	22.8	7.1	26.7	0.3	0.7	0.6	834	32	381	995	2,562	980	13	642	49	141	1,886
96GC-26b	py-sph-gn	26.4	12.0	18.5	0.1	0.3	0.4	518	48	163	364	1,530	746	1	463	15	184	2,340
96GC-26b	py-sph-gn	22.5	7.6	27.6	0.2	0.4	0.5	723	8	263	159	1,003	754	15	446	231	105	1,691
96GC-26b	py-sph-gn	26.4	5.1	24.0	0.1	0.6	0.4	501	30	216	169	674	589	16	555	136	112	2,725
96GC-26b	py-sph-gn	24.9	6.2	25.4	0.1	0.3	0.3	457	77	265	1,106	821	740	16	170	69	94	1,881
96GC-26b	py-sph-gn	18.1	11.3	30.3	0.2	0.7	0.7	368	22	278	153	221	1,295	25	599	127	31	3,345
96GC-25	py-tetr	38.7	4.9	4.9	1.4	0.8	0.4	1,322	63	72	1,461	7,427	820	0	156	107	349	388
96GC-25	py-tetr	41.2	1.1	3.5	2.2	0.7	0.6	2,639	62	66	43	88	215	6	380	119	97	1,212
96GC-18	py-tetr-gn	45.1	0.9	0.1	0.2	0.7	0.3	224	132	84	913	3,553	128	4	281	151		1,260
96GC-18	py-tetr-gn	43.7	2.9	0.2	0.2	1.2	0.2	221	96	67	729	1,914	24	18	200	164		2,160
96GC-18	py-tetr-gn	45.1	0.5	0.0	0.1	1.1	0.1	242	96	51	268	756	177	16	508	205		4,652
96GC-25	py-tetr-gn	13.6	27.1	1.4	22.2	2.4	3.2	11,825	96	309	719	1,230	270	1	72	26	62	769
96GC-25	py-tetr-gn-sph	24.3	14.2	6.6	5.1	1.4	9.2	5,350	31	158	636	1,831	417	6	217	109	230	0
96GC-25	py-tetr-qtz	43.9	2.2	0.1	1.1	0.7	0.3	1,438	66	53	891	332	106	11	590	82	168	1,307
96GC-25	tetr-gn	6.9	25.9	1.3	29.0	4.8	4.9	19,399	207	237	59	481	418	10	36	63	0	1,577
mean		26.6	19.1	8.7	3.1	1.0	1.4	2,915	58	144	549	1,991	394	9	377	95	150	1,571
std. deviation		10.2	14.7	9.6	6.2	0.9	1.9	4,274	43	95	451	2,510	319	6	283	70	124	1,228
maximum		45.1	58.0	30.3	29.0	4.8	9.2	19,399	207	381	2,155	11,930	1,295	25	1,250	368	541	4,695
minimum		2.3	0.5	0.0	0.1	0.3	0.1	221	2	19	43	16	24	0	23	7	0	0

Table 9. Trace-element composition of recrystallized mixed mineral aggregates as determined by Laser Ablation–Inductively Coupled Plasma– Mass Spectroscopy analyses.

Sample #	Mineralogy	Fe %	Pb %	Zn %	Cu %	As %	Sb %	Ag ppm	Au ppb	Hg ppm	Tl ppm	Mo ppm	Cd ppm	Bi ppm	Cr ppm	Co ppm	Ni ppm	Se ppm
96GC-18	aspy-gn	21.0	25.8	0.7	1.5	12.3	0.5	494	196	79	2158	1601	1191	37	420	150		6571
96GC-25	gn-sph-dolo	29.9	2.3	10.6	0.3	0.6	0.2	23952	164	109	651	2680	546	33	722	278	518	2016
96GC-25	gn-tetr	1.3	44.3	1.4	21.5	4.3	5.3	23107	10	306	8	7	321	1	31	11	12	366
96GC-19	py-gn	33.0	12.6	1.0	0.1	7.7	0.3	861	76	26	743	538	41	3	259	112		290
96GC-19	py-gn	37.5	11.4	2.8	0.0	1.1	0.1	64	32	51	756	194	182	14	312	161		2384
96GC-26b	py-gn-sph	13.4	31.6	19.9	0.9	0.8	1.6	1749	13	247	290	574	464	11	178	86	66	1999
96GC-26b	py-gn-sph	31.2	18.8	5.3	0.1	0.9	1.3	532	88	76	122	168	225	13	275	52	213	1038
96GC-26b	py-gn-sph	27.3	14.8	14.0	0.3	0.9	1.0	887	136	209	360	1695	709	170	365	56	131	2041
96GC-25	py-qtz	24.4	37.5	0.2	1.4	0.7	0.5	2013	86	60	1960	231	110	10	233	59	112	916
96GC-18	py-sph	32.1	0.3	19.8	0.2	0.2	0.1	374	411	173	68	341	657	9	218	251		3,867
96GC-19	py-sph	38.0	3.6	9.5	0.0	0.1	0.0	0	34	50	230	135	515	21	419	43		1,690
96GC-19	py-sph-gn	39.7	2.9	3.4	0.6	3.2	0.2	505	65	53	160	253	437	20	671	20		1,736
96GC-19	py-sph-gn	38.1	2.1	6.1	0.1	3.9	0.1	263	10	66	165	285	450	18	630	101		72
96GC-26b	py-sph-gn	29.1	20.5	8.5	0.1	0.2	0.4	3,126	10	86	895	516	179	4	46	15	62	293
96GC-26b	py-sph-gn	13.7	24.8	26.5	0.3	0.6	0.6	4,075	43	133	316	597	623	7	350	77	146	443
96GC-26b	py-sph-gn	23.6	7.4	26.4	0.1	0.3	0.5	487	87	241	305	3,316	874	15	277	-12	51	993
96GC-26b	py-sph-gn	23.3	14.2	20.9	0.4	0.5	0.5	1,166	72	248	158	1,334	968	7	228	76	282	1,246
96GC-26b	py-sph-gn	40.2	4.2	4.6	0.2	0.5	0.2	2,781	176	264	203	382	112	16	995	197	170	2,755
96GC-26b	py-sph-gn	34.3	6.8	11.6	0.1	0.2	0.4	161	118	655	164	217	127	37	942	71	145	1,753
96GC-18	py-sph-gn-tetr	29.5	7.3	8.1	5.1	0.6	5.0	10,149	70	158	764	3,989	531	23	289	387		2,466
96GC-25	py-tetr	31.0	6.3	4.9	7.0	3.9	1.0	17,964	119	284	970	2,688	239	5	427	128	279	678
96GC-26b	sph-dolo	2.8	1.0	60.8	0.2	0.3	0.2	557	89	1,667	116	180	1,843	9	223	125	73	3,590
96GC-26b	sph-py-gn	20.1	9.0	30.4	0.1	0.3	0.4	636	60	357	401	870	491	10	403	78	73	0
96GC-18	sph-tetr	1.9	0.0	43.0	8.1	0.7	14.0	1,422	579	1,359	260	147	4,631	4	438	319		3,696
96GC-19	sph-tetr	0.8	0.0	41.8	12.7	1.0	11.6	21,153	353	549	117	25	1,283	8	648	103		237
96GC-19	sph-tetr	0.4	1.4	58.5	2.2	0.8	3.4	4,566	745	1,283	396	0	2,022	28	757	342		3,631
96GC-19	tetr-gn	1.8	0.2	3.6	32.1	2.8	28.5	55,492	428	698	140	60	947	10	380	71		1,911
96GC-19	tetr-gn	1.5	13.7	3.2	27.1	2.5	23.3	51,249	307	566	1,431	56	864	5	289	72		2,570
96GC-19	tetr-gn	1.7	0.1	4.6	32.6	2.8	26.7	61,569	346	618	144	5	1,060	3	551	65		2,986
96GC-25	tetr-sph	3.6	1.7	27.7	16.2	4.2	7.2	96,112	169	1,573	124	117	501	6	294	97	173	269
96GC-25	tetr-sph	8.1	6.0	16.5	18.1	6.7	9.5	34,892	318	942	303	889	1,133	13	4,826	427	86	372
96GC-26b	tetr-sph-gn	9.4	24.4	20.5	9.1	1.0	4.4	13,988	5,401	128	193	178	710	2	22	8	21	156
mean		20.1	11.2	16.1	6.2	2.1	4.6	13,636	338	416	471	758	781	18	535	126	145	1,720
std. deviation		14.2	11.8	16.3	9.9	2.7	7.9	22,893	941	466	525	1,041	849	30	819	114	122	1,488
maximum		40.2	44.3	60.8	32.6	12.3	28.5	96,112	5,401	1,667	2,158	3,989	4,631	170	4,826	427	518	6,571
minimum		0.4	0.0	0.2	0.0	0.1	0.0	0	10	26	8	0	41	1	22	-12	12	0

Table 10. Trace-element composition of remobilized mixed mineral aggregates as determined by Laser Ablation–Inductively Coupled Plasma–Mass Spectroscopy analyses.

Sample #	Mineralogy	Fe %	Pb %	Zn %	Cu %	As %	Sb %	Ag ppm	Au ppb	Hg ppm	Tl ppm	Mo ppm	Cd ppm	Bi ppm	Cr ppm	Co ppm	Ni ppm	Se ppm
96GC-26b	gn-tetr	0.2	81.2	0.3	2.2	0.7	0.8	4,483	1	111	10	6	104	4	97	9	6	532
96GC-26b	gn-tetr	0.0	81.1	0.0	0.0	1.3	3.4	77	1	21	157	5	7	2	82	6	0	202
96GC-26b	gn-tetr	0.7	74.4	0.6	4.7	1.4	2.1	7,903	10	209	10	7	208	4	32	6	26	339
96GC-26b	gn-tetr	0.9	58.8	1.3	11.5	2.9	4.9	20,229	7	310	48	21	468	4	176	13	5	1,054
96GC-26b	py-gn-sph	16.6	32.0	16.3	0.6	0.6	0.6	3,307	46	50	597	206	301	1	49	10	45	302
96GC-26b	sph-py-gn	13.7	10.2	37.4	0.1	0.1	1.7	2,497	21	920	71	365	606	10	763	41	17	2,016
96GC-26b	tetr-gn	1.6	36.1	2.2	22.1	4.4	8.9	37,439	4	360	95	53	680	4	260	45	27	2,064
96GC-26b	tetr-py-sph-gn	18.0	4.6	6.1	29.4	3.4	1.5	19,174	79	259	110	123	2,095	8	359	254	43	487
mean		6.5	47.3	8.0	8.8	1.9	3.0	11,889	21	280	137	98	558	5	227	48	21	874
std. deviation		8.1	31.0	13.1	11.2	1.5	2.8	12,804	28	286	192	129	664	3	244	85	17	764
maximum		18.0	81.2	37.4	29.4	4.4	8.9	37,439	79	920	597	365	2,095	10	763	254	45	2,064
minimum		0.0	4.6	0.0	0.0	0.1	0.6	77	1	21	10	5	7	1	32	6	0	202

Figure 12. Single element plots of LA–ICP–MS data showing the range of elemental abundances of metals in primary and recrystallized pyrite (a–q) and sphalerite (r–ah), and in primary, recrystallized, and remobilized galena (ai–ay). (a) Fe in pyrite, (b) Pb in pyrite, (c) Zn in pyrite, (d) Cu in pyrite, (e) As in pyrite, (f) Sb in pyrite, (g) Ag in pyrite, (h) Au in pyrite, (i) Hg in pyrite, (j) Tl in pyrite, (k) Mo in pyrite, (l) Cd in pyrite, (m) Bi in pyrite, (n) Cr in pyrite, (o) Co in pyrite, (p) Ni in pyrite, (q) Se in pyrite, (r) Fe in sphalerite, (s) Pb in sphalerite, (t) Zn in sphalerite, (u) Cu in sphalerite, (v) As in sphalerite, (w) Sb in sphalerite, (x) Ag in sphalerite, (y) Au in sphalerite, (z) Hg in sphalerite, (aa) Tl in sphalerite, (ab) Mo in sphalerite, (ac) Cd in sphalerite, (ad) Bi in sphalerite, (ae) Cr in sphalerite, (af) Co in sphalerite, (ag) Ni in sphalerite, (ah) Se in sphalerite, (ai) Pb in galena, (aj) Sb in galena, (ak) Fe in galena, (al) Zn in galena, (am) Cu in galena, (an) As in galena, (ao) Ag in galena, (ap) Au in galena, (aq) Hg in galena, (ar) Tl in galena, (as) Mo in galena, (at) Cd in galena, (au) Bi in galena, (av) Cr in galena, (aw) Co in galena, (ax) Ni in galena, (ay) Se in galena. Pyrite data plotted from tables 2 and 3. Galena data plotted from table 5. Sphalerite data plotted from table 6.

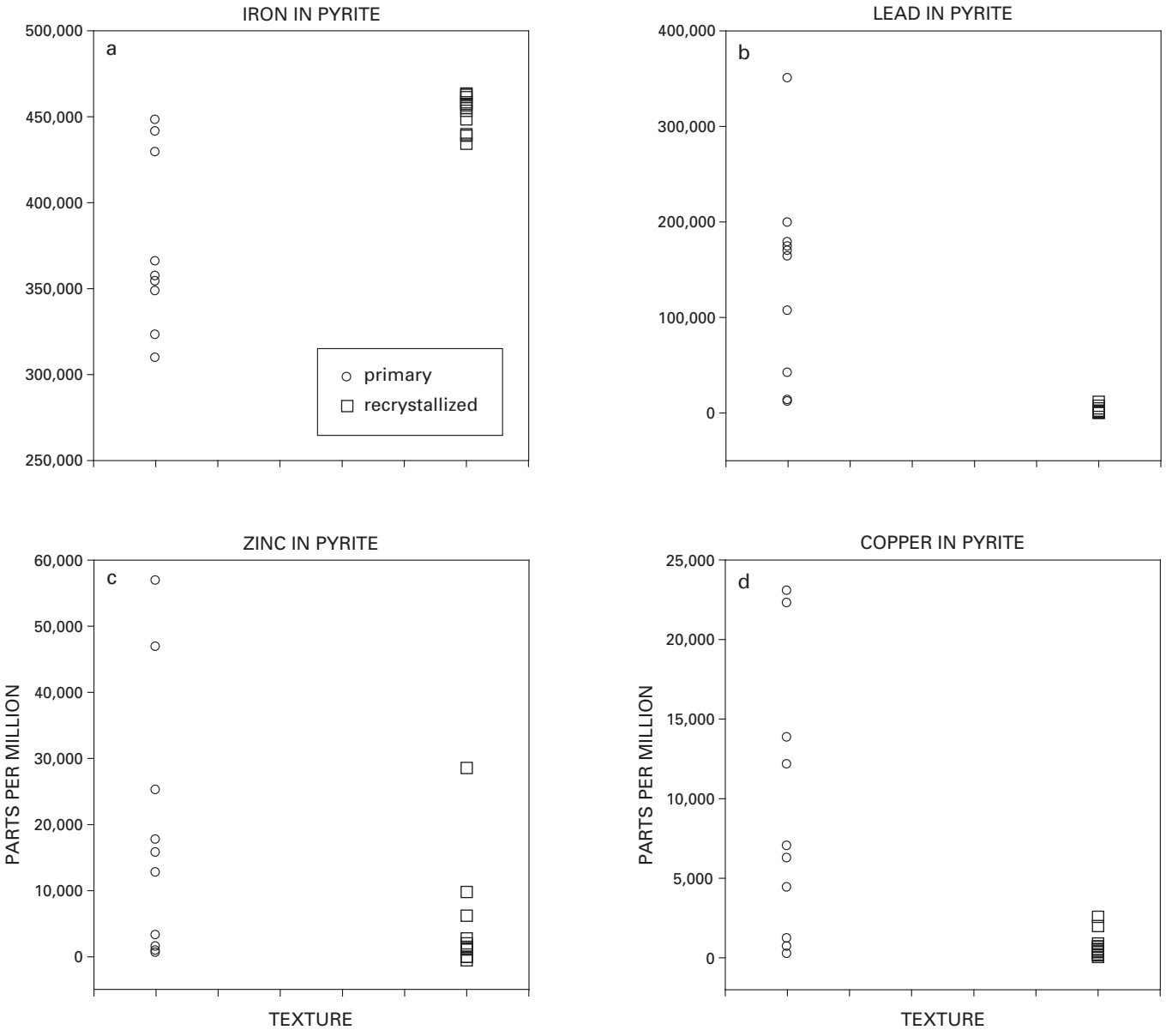

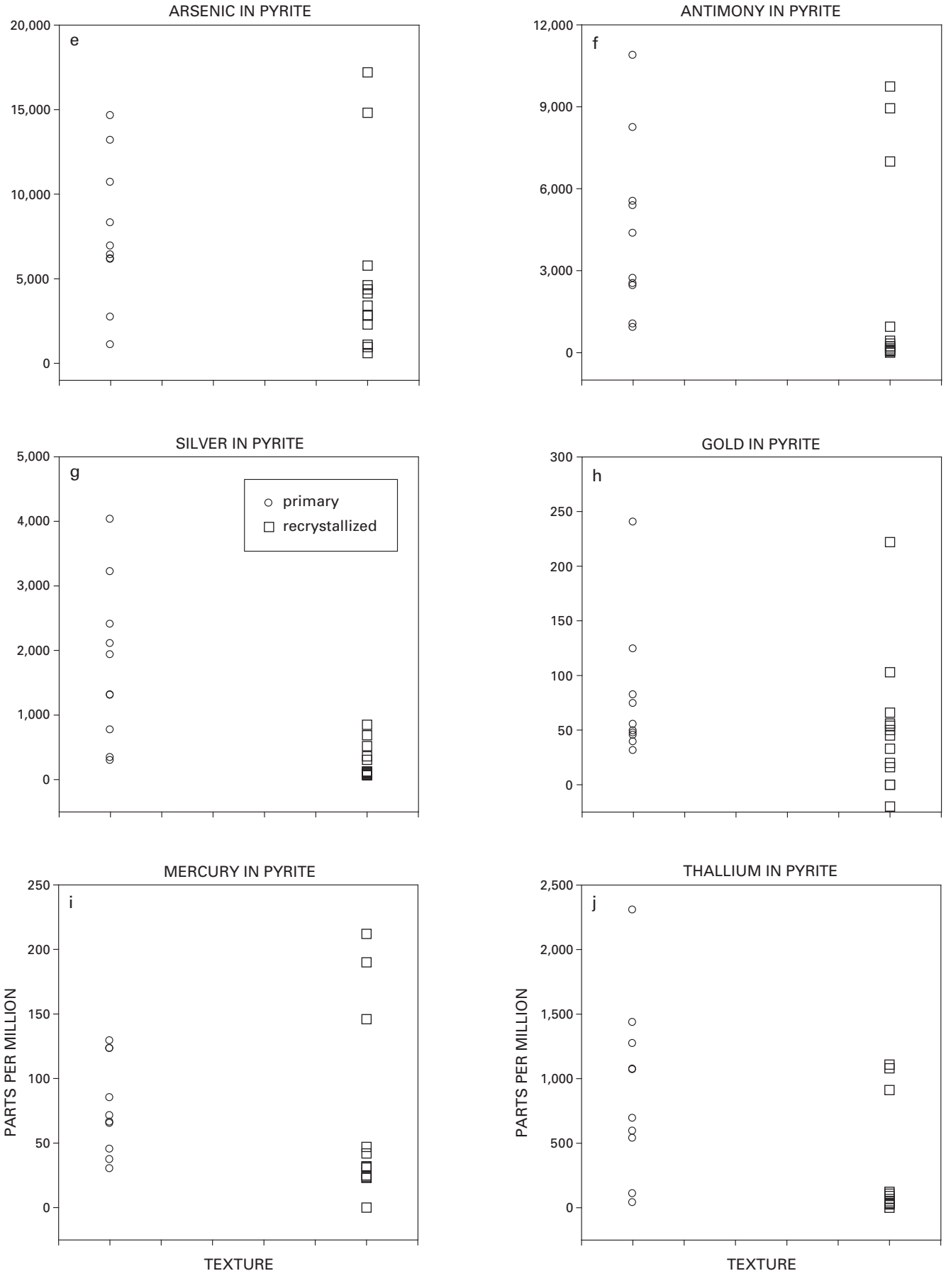
ARSENIC IN PYRITE
e
20,000
15,000
10,000
5,000
0
ANTIMONY IN PYRITE
f
12,000
9,000
6,000
3,000
0
SILVER IN PYRITE
g
5,000
4,000
3,000
2,000
1,000
0
primary
recrystallized
GOLD IN PYRITE
h
300
250
200
150
100
50
0
MERCURY IN PYRITE
i
250
200
150
100
50
0
PARTS PER MILLION
TEXTURE
THALLIUM IN PYRITE
j
2,500
2,000
1,500
1,000
500
0
PARTS PER MILLION
TEXTURE

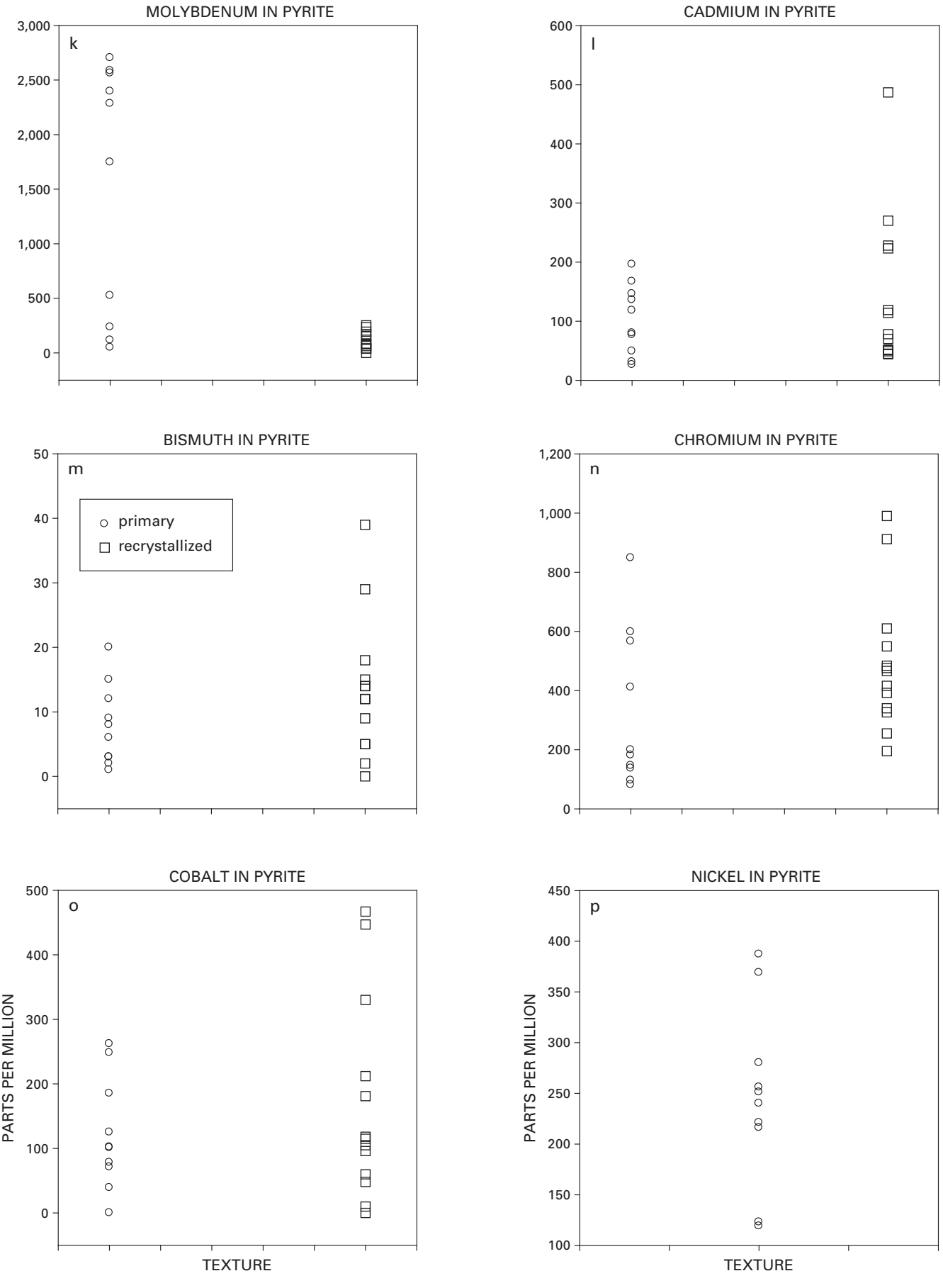
MOLYBDENUM IN PYRITE
k
3,000
2,500
2,000
1,500
1,000
500
0
CADMIUM IN PYRITE
l
600
500
400
300
200
100
0
BISMUTH IN PYRITE
m
primary
recrystallized
50
40
30
20
10
0
CHROMIUM IN PYRITE
n
1,200
1,000
800
600
400
200
0
COBALT IN PYRITE
o
500
400
300
200
100
0
NICKEL IN PYRITE
p
450
400
350
300
250
200
150
100
PARTS PER MILLION
TEXTURE

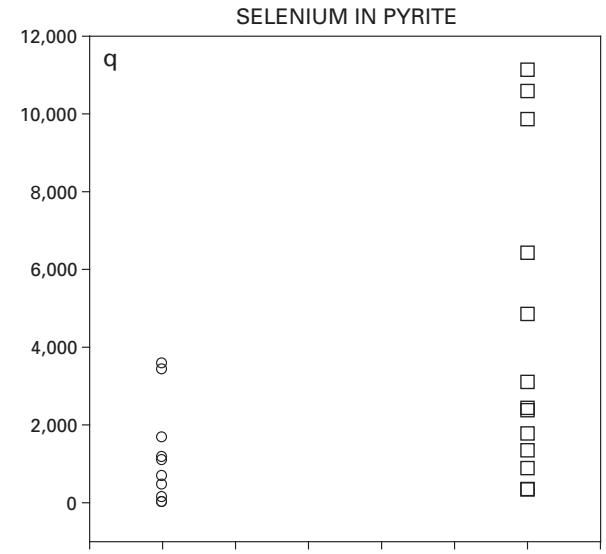
SELENIUM IN PYRITE
q
12,000
10,000
8,000
6,000
4,000
2,000
0

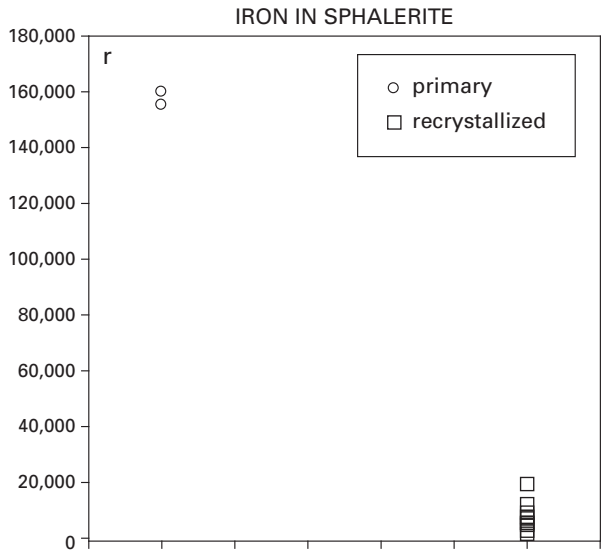
IRON IN SPHALERITE
r
primary
recrystallized
180,000
160,000
140,000
120,000
100,000
80,000
60,000
40,000
20,000
0

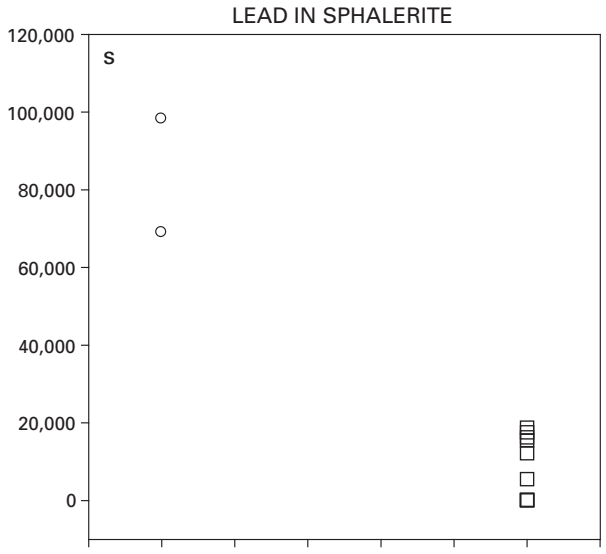
LEAD IN SPHALERITE
s
120,000
100,000
80,000
60,000
40,000
20,000
0

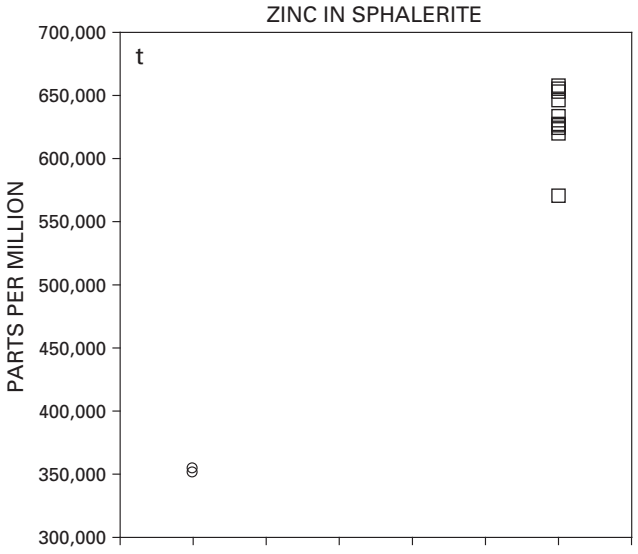
ZINC IN SPHALERITE
t
PARTS PER MILLION
700,000
650,000
600,000
550,000
500,000
450,000
400,000
350,000
300,000

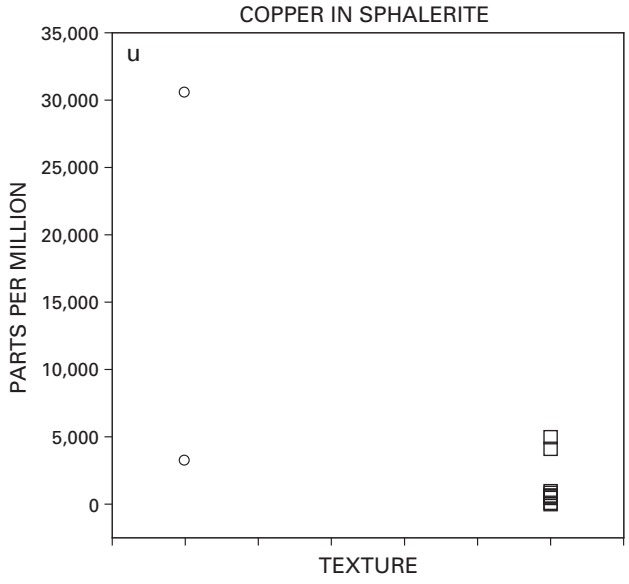
COPPER IN SPHALERITE
u
PARTS PER MILLION
35,000
30,000
25,000
20,000
15,000
10,000
5,000
0
TEXTURE

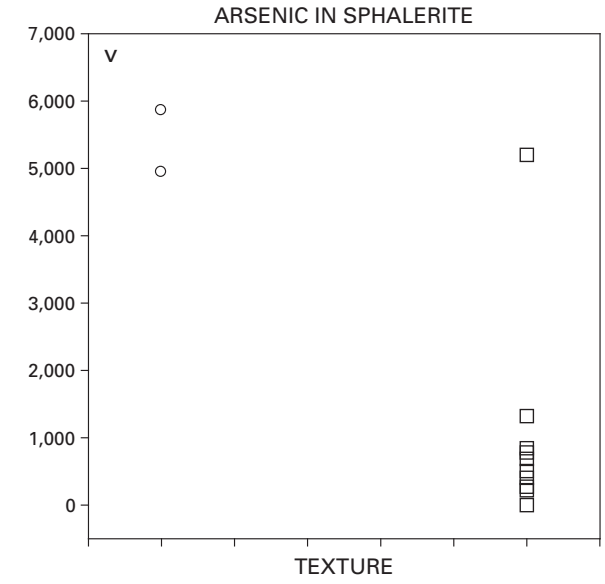
ARSENIC IN SPHALERITE
v
7,000
6,000
5,000
4,000
3,000
2,000
1,000
0
TEXTURE

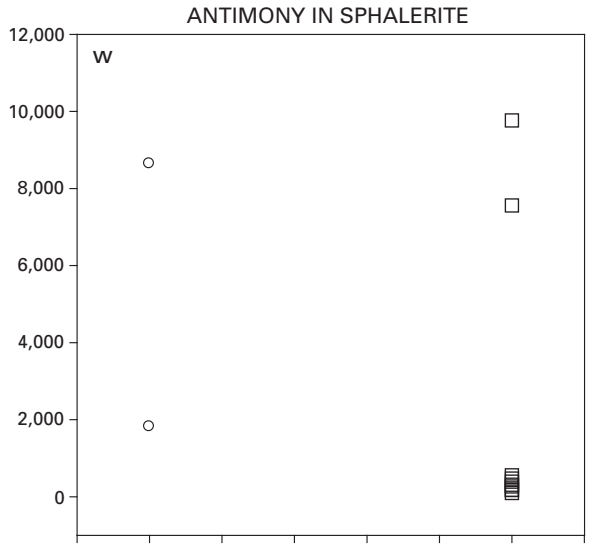
ANTIMONY IN SPHALERITE
w
12,000
10,000
8,000
6,000
4,000
2,000
0

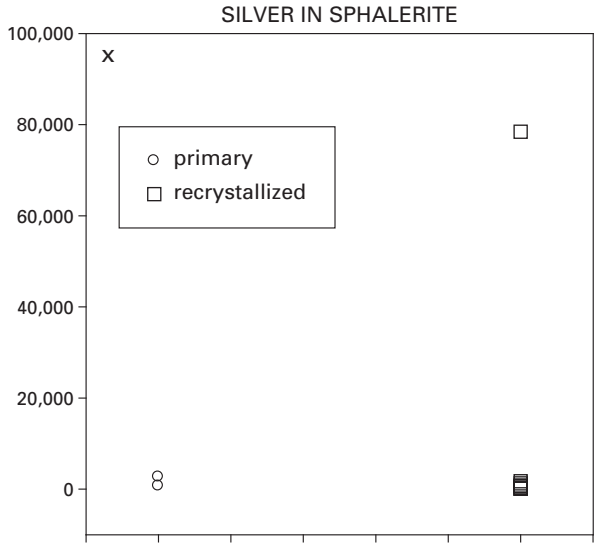
SILVER IN SPHALERITE
x
100,000
80,000
60,000
40,000
20,000
0
primary
recrystallized

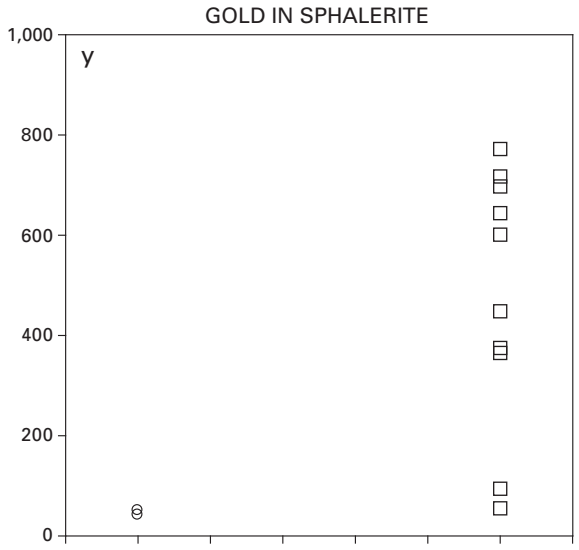
GOLD IN SPHALERITE
y
1,000
800
600
400
200
0

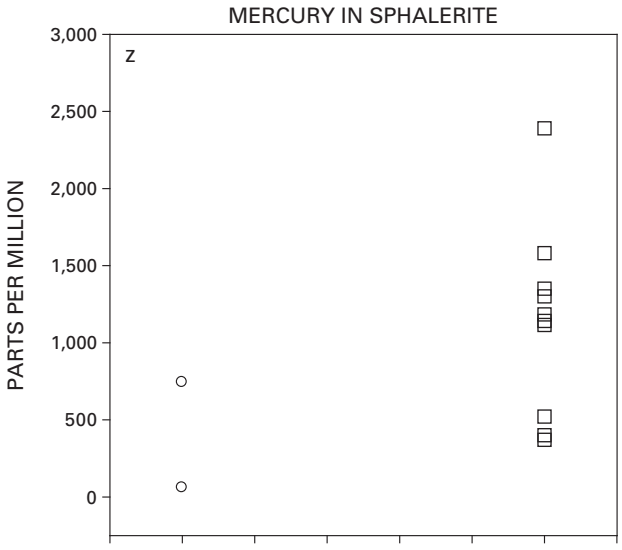
MERCURY IN SPHALERITE
z
PARTS PER MILLION
3,000
2,500
2,000
1,500
1,000
500
0

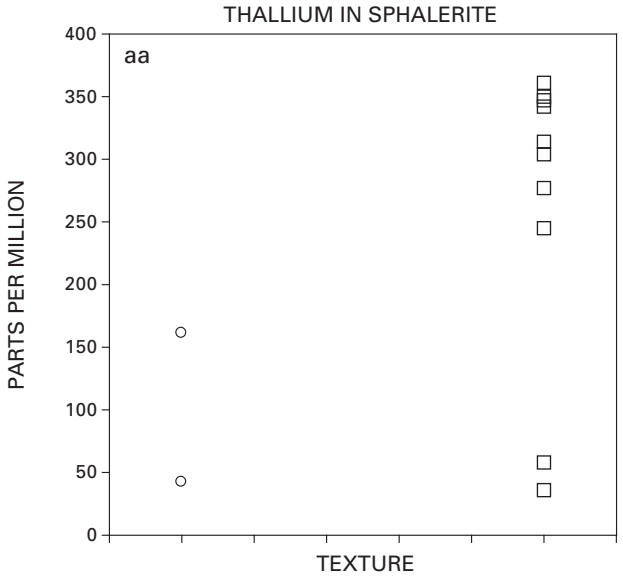
THALLIUM IN SPHALERITE
aa
PARTS PER MILLION
400
350
300
250
200
150
100
50
0
TEXTURE

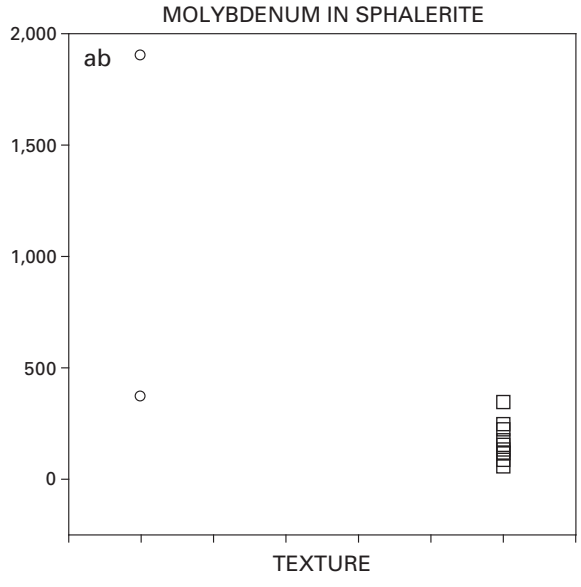
MOLYBDENUM IN SPHALERITE
ab
2,000
1,500
1,000
500
0
TEXTURE

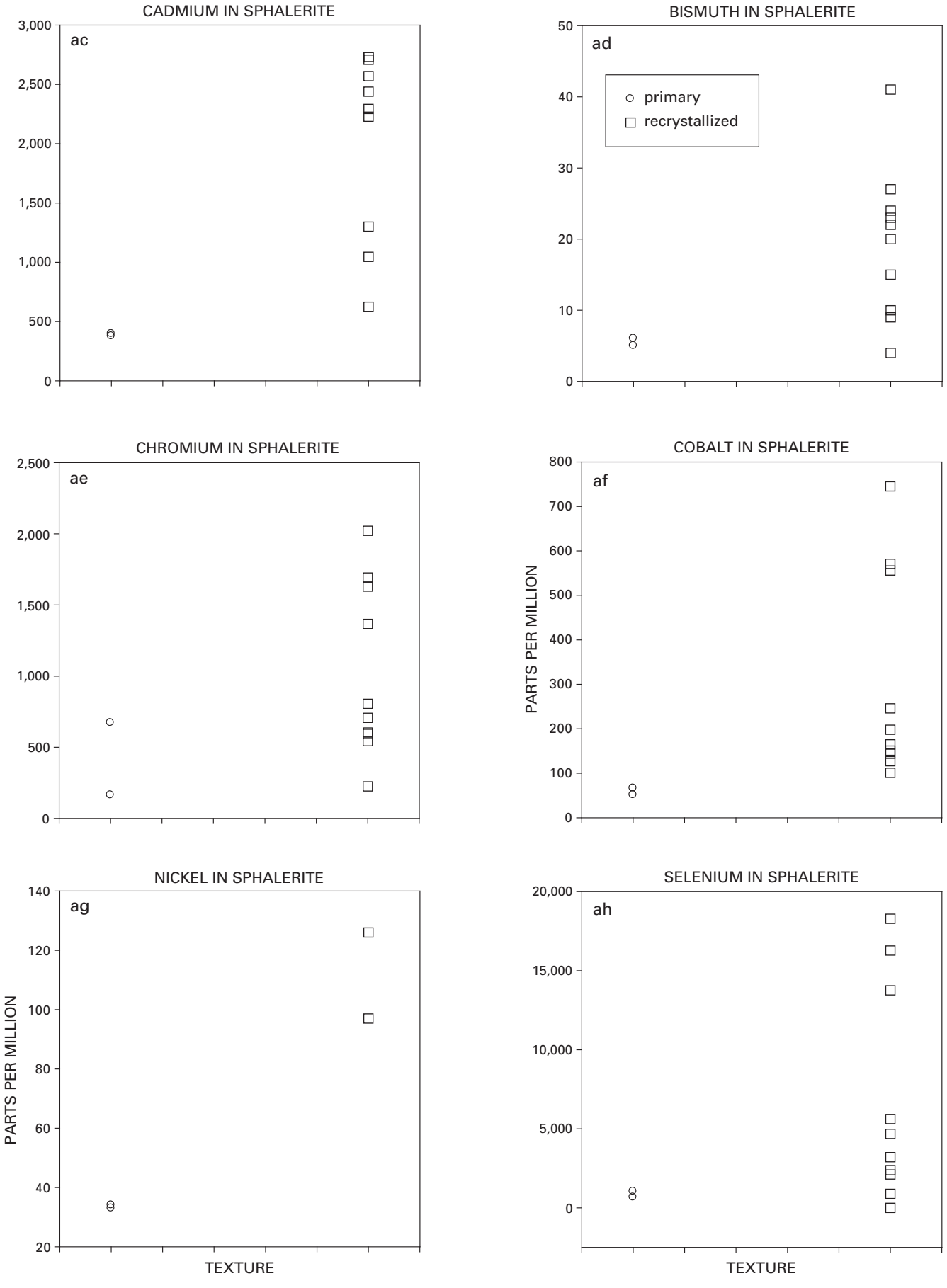
CADMIUM IN SPHALERITE
ac
3,000
2,500
2,000
1,500
1,000
500
0
BISMUTH IN SPHALERITE
ad
primary
recrystallized
50
40
30
20
10
0
CHROMIUM IN SPHALERITE
ae
2,500
2,000
1,500
1,000
500
0
COBALT IN SPHALERITE
af
PARTS PER MILLION
800
700
600
500
400
300
200
100
0
NICKEL IN SPHALERITE
ag
PARTS PER MILLION
140
120
100
80
60
40
20
TEXTURE
SELENIUM IN SPHALERITE
ah
20,000
15,000
10,000
5,000
0
TEXTURE

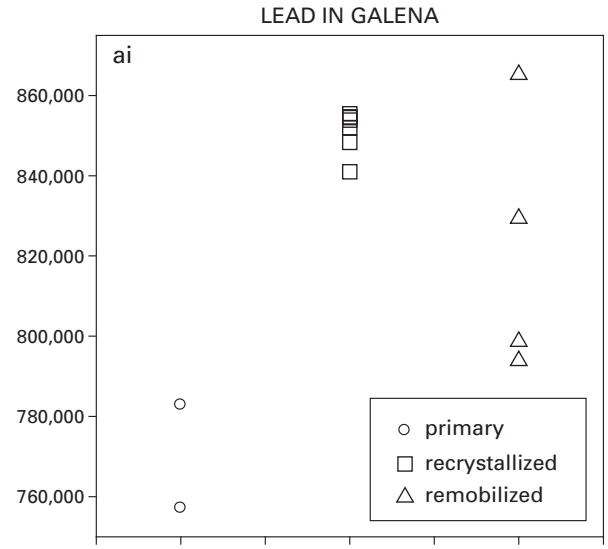
LEAD IN GALENA
ai
860,000
840,000
820,000
800,000
780,000
760,000
primary
recrystallized
remobilized

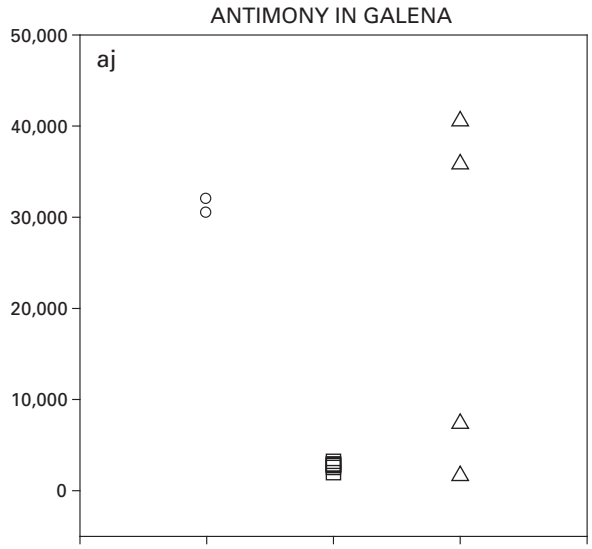
ANTIMONY IN GALENA
aj
50,000
40,000
30,000
20,000
10,000
0

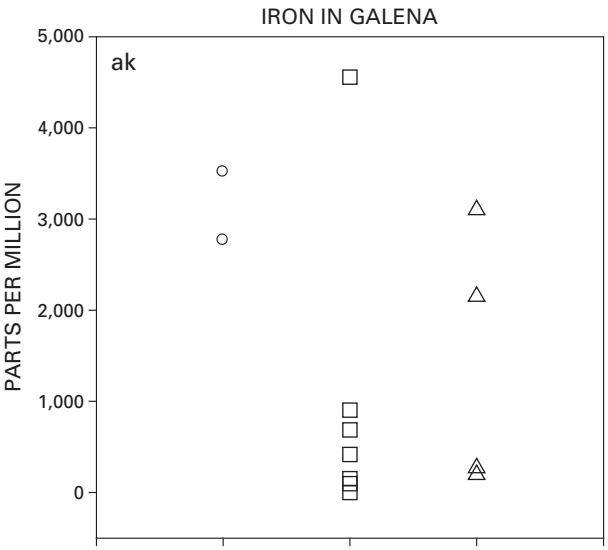
IRON IN GALENA
ak
PARTS PER MILLION
5,000
4,000
3,000
2,000
1,000
0

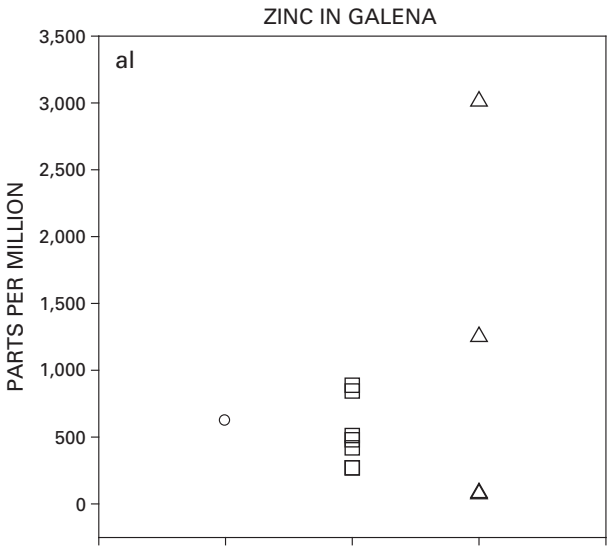
ZINC IN GALENA
al
PARTS PER MILLION
3,500
3,000
2,500
2,000
1,500
1,000
500
0

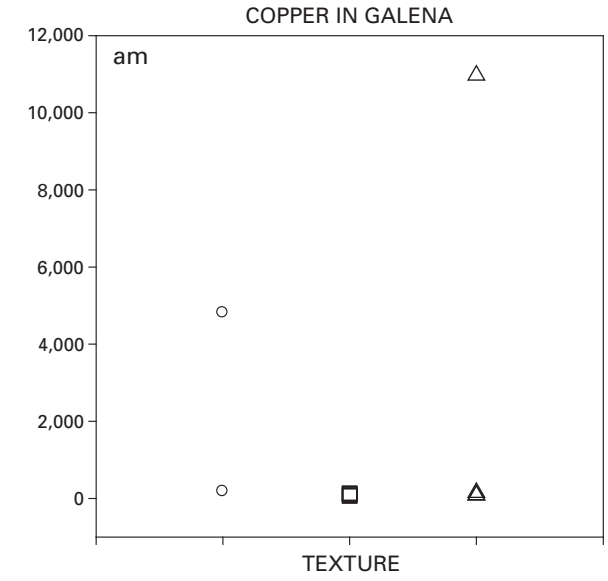
COPPER IN GALENA
am
12,000
10,000
8,000
6,000
4,000
2,000
0
TEXTURE

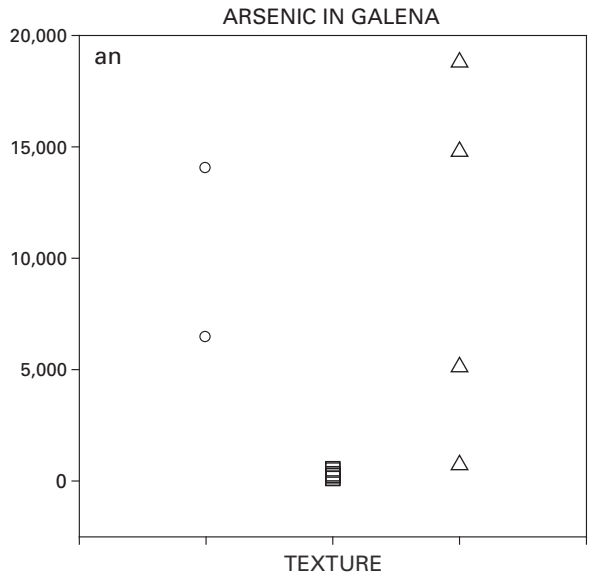
ARSENIC IN GALENA
an
20,000
15,000
10,000
5,000
0
TEXTURE

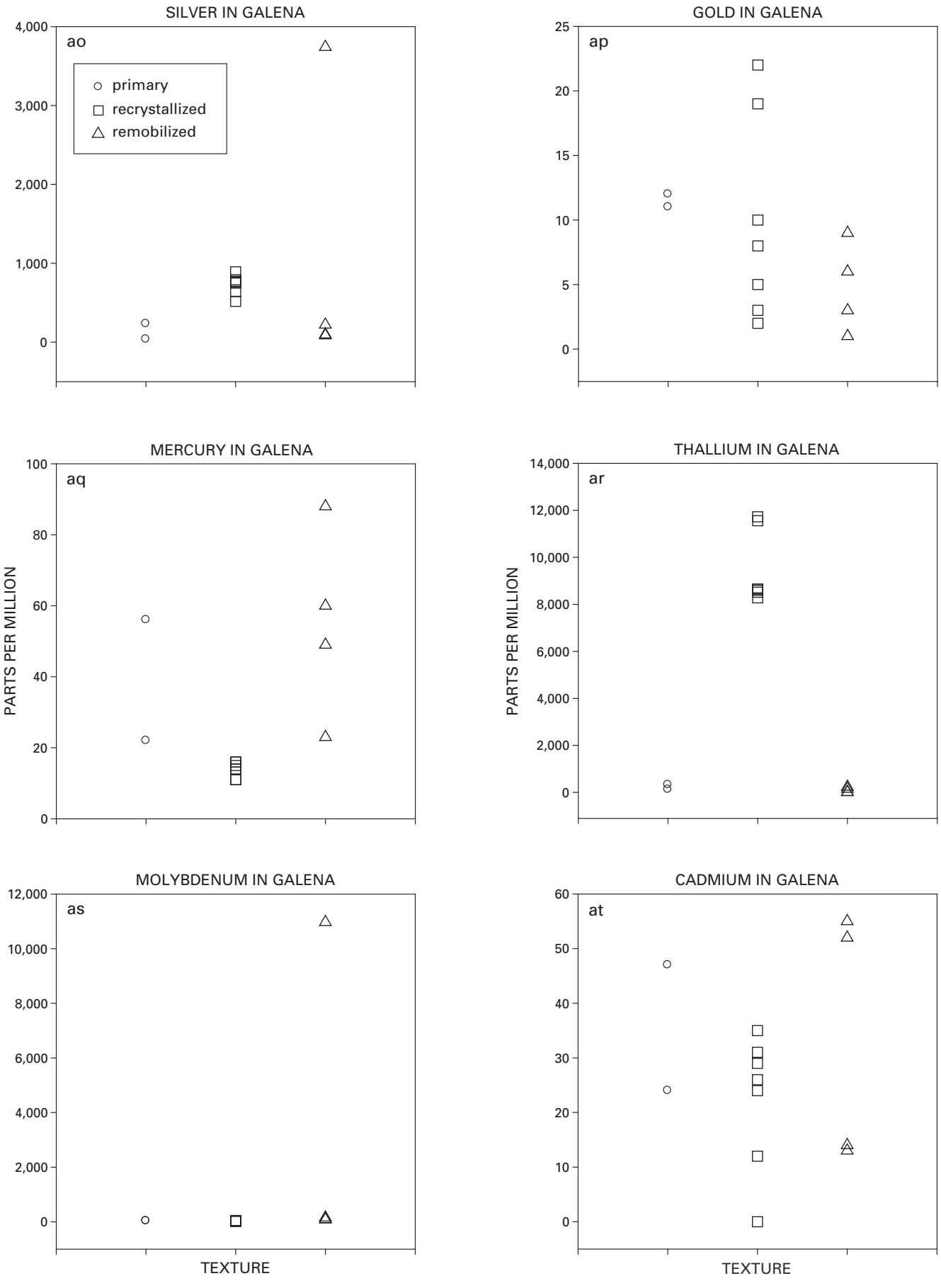
SILVER IN GALENA
ao
primary
recrystallized
remobilized
4,000
3,000
2,000
1,000
0
GOLD IN GALENA
ap
25
20
15
10
5
0
MERCURY IN GALENA
aq
PARTS PER MILLION
100
80
60
40
20
0
THALLIUM IN GALENA
ar
PARTS PER MILLION
14,000
12,000
10,000
8,000
6,000
4,000
2,000
0
MOLYBDENUM IN GALENA
as
12,000
10,000
8,000
6,000
4,000
2,000
0
TEXTURE
CADMIUM IN GALENA
at
60
50
40
30
20
10
0
TEXTURE

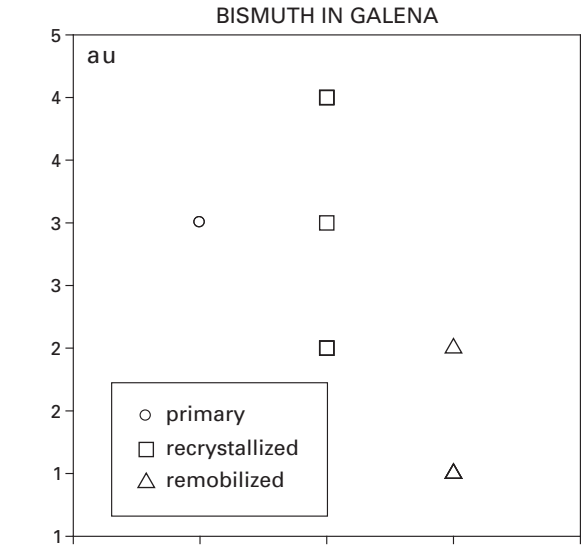
BISMUTH IN GALENA
au
5
4
4
3
3
2
2
1
1
primary
recrystallized
remobilized

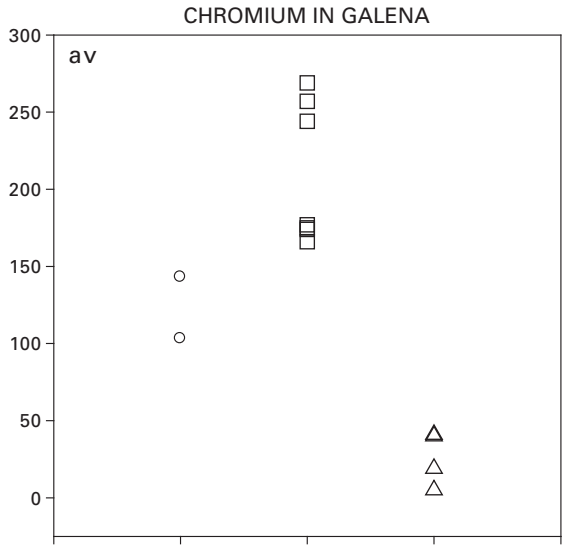
CHROMIUM IN GALENA
av
300
250
200
150
100
50
0

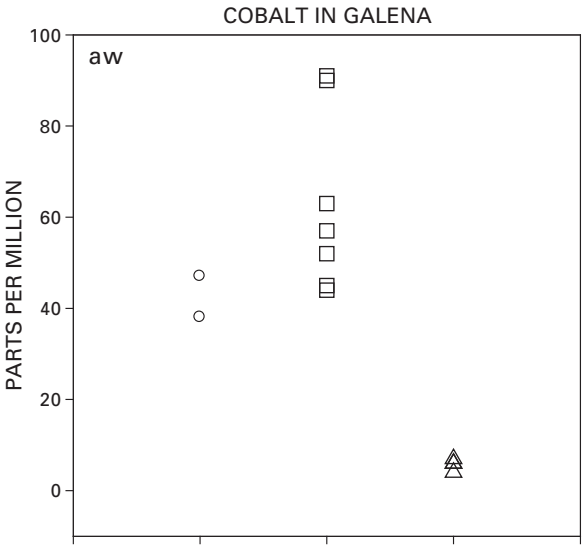
COBALT IN GALENA
aw
100
80
60
40
20
0
PARTS PER MILLION

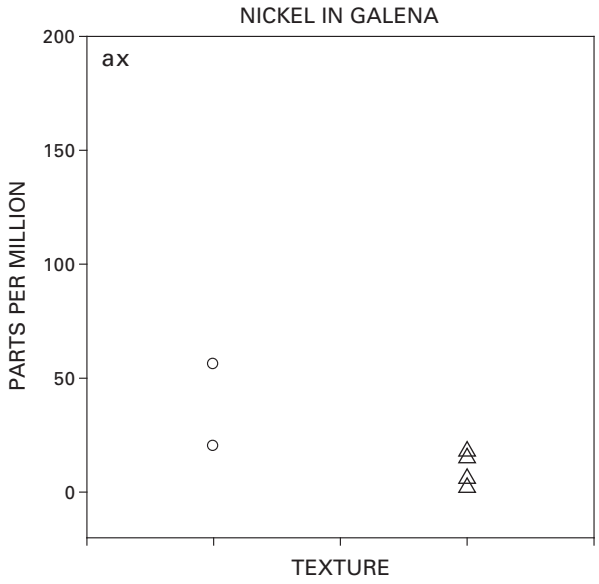
NICKEL IN GALENA
ax
200
150
100
50
0
PARTS PER MILLION
TEXTURE

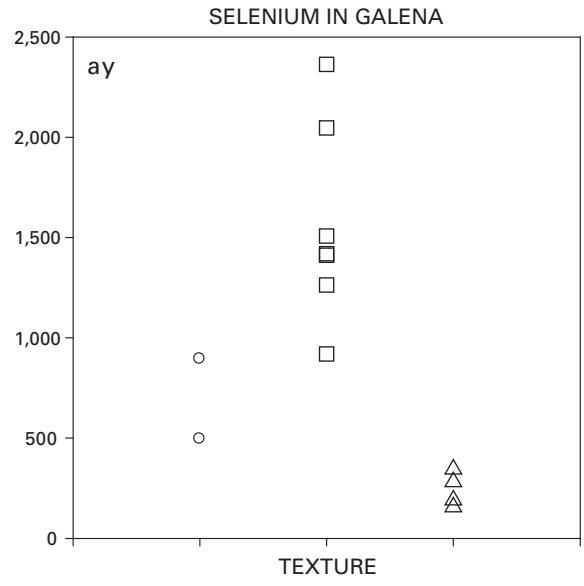
SELENIUM IN GALENA
ay
2,500
2,000
1,500
1,000
500
0
TEXTURE

Discussion

There are a number of mineralogical, textural, and geochemical features of the ores as described herein that bear directly on elucidating the genetic processes of formation leading to the Greens Creek deposit and its subsequent modification during regional deformation. We will concentrate first on characteristics of the primary ores and whether their textures and geochemistry yield useful information regarding their origin. We will then discuss the subsequent deformation of the ores and whether specific textures are indicative of the timing or physical parameters of the deformation event. Finally, we will look at the nature and the extent of both solid- and liquid-state remobilization of minerals and metals in the ores and the effect of remobilization on the distribution and grade of the ores.

Pyrite provides the most complete textural record of mineral formation and subsequent modification due to its ubiquity in all ores and host rocks throughout the deposit and as the hardest ore mineral, as indicated by its resistance to texture-obliterating plastic deformation. The paragenetically earliest pyrites have framboidal and colloform banded textures with layers of sphalerite, galena, tetrahedrite, and probably other complex lead-antimony sulfides, and dendritic textures. These textures are preserved in relatively undeformed blocks of massive pyritic ore or in clasts within blocks of MFP that display abundant evidence of brittle failure and cataclasis. Similar textures are commonly preserved in ancient massive sulfide deposits and are usually referred to as primary depositional textures that are taken as evidence of ore deposition on or near the sea floor as a result of rapid cooling and mixing of a hydrothermal fluid with cold seawater (Leitch, 1981; Eldridge and others, 1983; Yui, 1983; McClay, 1991; Craig and Vokes, 1992; Gaspar and Pinto, 1993; Larocque and Hodgson, 1995; Hannington and others, 1999). Numerous observations of identical textures forming in active sea-floor systems worldwide (Graham and others, 1988; Koski and others, 1988, 1994; Paradis and others, 1988; Binns and others, 1993; Halbach and others, 1993; Duckworth and others, 1995; Knott and others, 1995; Krasnov and others, 1995) would seem to confirm the sea-floor origin of such textures.

Detailed studies of active systems, however, indicate that a substrate is necessary upon which such primary textures form by replacement of amorphous silica and cementation of porosity. Two likely substrates include a biotic framework of tubeworms and filamentous bacteria (Knott and others, 1995; Juniper and others, 1992) or a porous boxwork of silica-anhydrite-barite formed by early low-temperature venting of fluids (Haymon, 1983). Once a substrate is established, sulfide mound growth occurs within this substrate initially by constructional growth of spheroidal, colloform, and dendritic pyrite with lesser sphalerite and galena, and then by replacement of the early colloform textures by euhedral forms. Growth of the sulfide body proceeds by high-temperature replacement of previously formed lower temperature phases and outward metal displacement or "zone refinement." Even the earliest formed sulfides in most active sea-floor massive sulfides form by replacement processes and rapidly evolve to exhibit euhedral mineral textures. Therefore, the earliest mineral textures at Greens Creek likely represent formation beneath the sediment/water interface.

An additional feature of the primary mineral textures at Greens Creek indicates that the hanging-wall shales were being deposited early in the ore-forming process. We note that the majority of the primary-textured pyrite that has survived metamorphism exhibits polyframboidal and spongy pyrite textures. These textures suggest that large masses of MFP were formed by coalescence of framboids and infilling of porosity by precipitation of additional pyrite. Because true framboids are generally thought of as products of early iron sulfide diagenesis in sediments, their presence as the major precursor to spongy-textured massive pyrite indicates the shales were in place and undergoing early diagenesis during the main-stage ore-forming event. True framboids are distinguished from the colloform- and spheroidal-textured sulfide grains commonly seen in both modern and ancient massive sulfides by their characteristic raspberrylike appearance. They typically consist of spherical aggregates, 5–40 mm in size, of 0.2–5-mm pyrite crystallites. Crystallites exhibit ordered or disordered packing with intercrystallite spaces left void or infilled with later sulfides, quartz, and(or) carbonate (England and Ostwald, 1993). The presence of abundant framboids in all Greens Creek ores with relict primary texture is consistent with the sulfur, carbon, and oxygen isotope data that support the origin of the main stage ores by biogenic sulfate reduction in and beneath an accumulating shale cap (chaps. 8, 10).

Direct evidence of widespread replacement of shales by sulfide minerals is generally lacking. This may indicate that growth of main stage ore happened primarily at the phyllite/argillite contact or by inflation of a previously formed silica-barite-sulfide framework, as is often indicated for actively forming systems today (Haymon, 1983; Paradis and others, 1988; Binns and others, 1993; Petersen and others, 2000). Another possibility is that we do not have the undisturbed mesoscale exposures necessary to observe sulfide replacement fronts in the hanging-wall shales at the margins of the orebodies. In general the ore/hanging-wall contact is sharp, but in many places the sulfide content of the argillite is gradational over several meters. The ore/hanging-wall contact is commonly a zone of strong deformation due to the tendency for the shales to accommodate strain and the usual superposition of the shales against the ductile massive base-metal-rich ores. The MFBs at this contact are generally tectonically banded with near-complete destruction of primary textures, and the ore/argillite contact can be a slip surface exhibiting graphite-rich, polished gouge. Thus, direct observational evidence for sulfide replacement of argillites is inconclusive.

We suggest, based largely on ore stratigraphic and geochemical considerations, that the earliest mineral precipitation at Greens Creek was exhalative, silica-barite-carbonate-rich material that acted as the substrate within which the later,

main-stage massive sulfide grew. Discontinuous massive and debris-flow carbonate units in the immediate footwall exhibit both nodular-colloform pyrite and late dolomite cement textures that are indicative of diagenetic and epigenetic formation in fractures and dissolution cavities. These features, reminiscent of mineral textures common in Mississippi Valley-type (MVT) deposits (Leach and Sangster, 1993), demonstrate that hydrothermal fluids traversed through the carbonates on route to the site of ore formation. Primary textures similar to those observed in the MFPs are occasionally preserved in the more competent WSIs and support the idea that growth of main-stage mineralization occurred primarily by sulfide replacement of the white ores. Additionally, the association of occasional grains of free gold and electrum and elevated precious metal grades within these WSIs supports the suggestion that the early fluids were hydrogen sulfide and precious metal rich and base metal poor. The absence of well-developed WCAs and WBAs directly beneath proximal accumulations of WSI and MFP and the presence of these barite-carbonate-rich white ores beneath and lateral to massive sulfide ores in distal portions of the mine further indicates that main-stage ore transgressed and obliterated much of the early white ores. The less competent WCAs and especially the WBAs usually do not preserve evidence of primary mineral textures.

Several features suggest that as main-stage massive sulfide mineralization progressed, the Greens Creek system went through a process of zone refinement as described in many ancient and modern VMS systems (Eldridge and others, 1983; Goldfarb and others, 1983; Huston and Large, 1989; Large and others, 1989; Hannington and others, 1986; Petersen and others, 2000). Most compelling is the typical pattern of metal zonation observed at Greens Creek. Where the complete ore stratigraphy is present, metal zonation progresses from proximal copper-gold-arsenic rich, to zinc-lead-silver rich, to more lead, silver, and gold-enriched zinc-lead-silver ores at the margins. Such a pattern is identical to that expected due to selective remobilization of metals by a hydrothermal fluid from the interior of a growing sulfide accumulation, transport of metals toward the margins of the accumulation, and reprecipitation along a temperature-solubility gradient (Huston and Large, 1989). Thus, despite considerable subsequent remobilization of metals and deformation of the ores as a result of the Cretaceous metamorphism, we believe Greens Creek preserves an original mineral and metal zonation that is attributable to early sulfide replacement and zone refining within a growing sulfide accumulation.

A more circumstantial feature indicative of zone refinement is indicated by early replacement textures within proximal, primary-textured ores. In the proximal copper-rich ores of the Northwest West orebody, chalcopyrite has been found replacing pyrite within concentrically banded spheroids and colloform pyrite-sphalerite-galena-rich structures (fig. 5*G*). Close examination shows that chalcopyrite cuts across banding and engulfs remnants of other sulfide minerals, demonstrating that the paragenetic order of chalcopyrite succeeds the primary-textured sulfides. Similar observations have been used to establish the paragenetic position of chalcopyrite in the undeformed ores of the Kuroko deposits (Eldridge and others, 1983). Also, in one instance, framboidal-textured crystallites of chalcopyrite occur within a pyrite matrix that is surrounded by dolomite (fig. 10*C*). This sample may represent a rare case of primary chalcopyrite framboids. However, if all modern framboids are composed of pyrite (England and Ostwald, 1993), then this occurrence demonstrates replacement of pyrite by chalcopyrite. Replacement must have occurred prior to metamorphism and probably during the zone-refining stage.

Euhedral arsenian pyrite and arsenopyrite crystals in proximal MFPs (figs. 7*A–F*) appear to be another textural feature that occurs as a secondary modification of primary ores prior to metamorphism. When present, arsenian pyrite is always in spatial association with primary-textured pyritic ores and tends to be concentrated along the margins of, or in passageways through, areas of massive sulfide where original porosity would have been greatest. It always exhibits unstrained subhedral to euhedral shapes, does not show a preferred orientation, and is generally clean and free of inclusions of other minerals. Elevated nickel, arsenic, and gold contents of the arsenian pyrite suggest a high-temperature metal association (for example, note similarity to the high-temperature metal assemblage at Kidd Creek in Hannington and others, 1999) as does the generally proximal position of these arsenic-rich pyritic ores and their close association to chalcopyrite-rich MFPs with elevated copper-gold contents. Thus, arsenian pyrite appears to have formed in the high-temperature proximal areas of the deposit by replacement of trace-element-rich, primary-textured pyrite. Though we cannot demonstrate conclusively that arsenian pyrite is not a product of metamorphic remobilization of constituents out of the primary ores, the lack of (1) strained crystals, (2) location in pressure shadows, or (3) evidence of solution creep, suggests formation after the primary ores in areas unaffected by metamorphism. Additionally, the observation that some of the most ^{34}S-depleted sulfur isotope values are from arsenian pyrite-rich ores (see chap. 10) is consistent with formation when supply of isotopically light sulfur from the hanging wall was at a maximum, presumably during main-stage ore formation. The extreme $\delta^{34}S$ depletion of the arsenic-rich ores also demonstrates the lack of a homogenized sulfur isotope signature that might be expected of a sulfide produced as a result of metamorphic remobilization and further demonstrates the association of light sulfur with the main-stage massive sulfides (chap. 10). Koski and others (1994) document the formation of arsenopyrite-lollingite “fronts” during zone refining of black smoker chimneys in the Escanaba Trough.

One of the most interesting textural features of the primary-textured ores is the abundance of pyrite framboids, polyframboids (rogenpyrite), nodules, and a variety of spheroidal and atoll-shaped structures that appear to be modifications of originally framboidal grains. Collectively, these features provide strong evidence for the concurrence of main-stage ore formation at Greens Creek with the accumulation and early diagenetic history of the hanging-wall sediments. Examination of polished thin sections provides evidence for a complete textural evolution from early

framboidal and colloform features, through intermediate stages where coalescence of atoll-shaped and spheroidal aggregates occurs, to a final spongy-textured pyrite stage with abundant inclusions of other ore and gangue minerals. Such an origin and evolutionary process has been described by England and Ostwald (1993) for syngenetic and vein-type massive sulfides of the Lachlan Fold Belt of Eastern Australia. Several points emphasized in their work have significance for the origin of such textures at Greens Creek. First, they conclude that the presence of framboids and subsequently derived atoll structures is indicative of early diagenetic processes in anoxic sediments. Second, they suggest that the recrystallization and crystal growth of polyframboid aggregates and the subsequent development of atoll structures requires the presence of a gel-like substance such as colloidal silica, chalcopyrite gel, or other base-metal-sulfide gels through which iron and sulfur can diffuse to the framboidal growth centers. If England and Ostwald (1993) are correct, the presence of framboid-derived textures at Greens Creek constitutes additional compelling evidence for our suggestion that the main-stage ores formed predominantly during and after deposition of the hanging wall, that is, during early diagenesis. If a gel-like medium is required for the diffusion of iron and sulfur into polyframboid aggregates to create atolls and spongy-textured massive pyrite, this implies that diffusion of other metals also may occur at this time and has important implications for the zone refinement process. Simply based on mineralogical and textural observations, the process of framboid agglomeration, coalescence, and recrystallization described herein appears to result in a migration of base metals out of the predominantly pyritic masses. This results in spongy pyritic masses with elevated copper, arsenic, and gold and a spatial association with euhedral arsenian pyrite, which we previously suggested is a product of zone refinement. It seems reasonable that the zone-refinement process would be facilitated if the process occurred within a growing sulfide accumulation that was partially colloidal gel and partially a crystalline silica-sulfide framework, and by the presence of unlithified sediments. Perhaps the presence and coalescence of framboid-derived textures at Greens Creek and other massive sulfide deposits represent textural evidence of a zone-refinement process and link the timing of ore formation to early diagenesis of the enclosing sediments.

In the massive sulfide ores studied by England and Ostwald (1993), chalcopyrite was the major phase associated with the more evolved framboid-derived pyrite textures, leading these workers to suggest chalcopyrite gel was the primary diffusion media. We note that at Greens Creek chalcopyrite only rarely occurs in association with framboid-derived structures and then only as a clearly replacive and(or) infilling phase. However, in all cases where atoll-shaped grains occur, they are associated with other base-metal sulfides such as sphalerite, galena, tetrahedrite, and probably other more complex lead-antimony sulfides. The association of atolls with base-metal-sulfide matrix is consistent with the suggestion of England and Ostwald (1993) that the presence of a gel-like diffusion media is required for the growth of more texturally evolved pyrite structures.

We also note the abundant documentation of the zone-refinement process in chimney structures on the modern sea floor (Graham and others, 1988; Paradis and others, 1988; Krasnov and others, 1995; Duckworth and others, 1995; Knott and others, 1995; Petersen and others, 2000). Many of these chimneys occur in nonsedimented settings or project well above any sediment cover. Clearly these examples demonstrate that early diagenetic processes in enclosing sediments are not a requirement for zone refinement to occur. However, these do not invalidate the notion that zone refinement may be enhanced by the presence of gel sulfides in the porous framework of the chimneys.

Also, we note that although spherical, framboidlike textures are described in the modern sea-floor sulfide literature and that true framboids have been documented from a wide variety of massive sulfide deposit types, including veins, and VMS deposits not associated with sediments (Leitch, 1981; Eldridge and others, 1983; England and Ostwald, 1993; Hannington and others, 1999), they are far more ubiquitous in deposits associated with sediments such as MVT, SEDEX lead-zinc, and sedimentary copper deposits (Schouten, 1946; Croxford and Jephcott, 1972; Chen, 1978; Leach and Sangster, 1993; Large and Walcher, 1999). A literature search also indicates that, while spheroidal and colloform textures are common in modern massive sulfides, true framboids are described only from sediment-covered sites (Koski and others, 1988, 1994; Peter and Scott, 1988). We suggest that true framboids are relatively uncommon in nonsediment-associated modern and ancient massive sulfide deposits and that when present, they indicate early diagenetic mineral formation. The presence of framboid-derived textures at Greens Creek and in numerous other, more typical VMS deposits suggests that early diagenetic ore formation may be more common than has been previously recognized. The presence of true framboid-derived textures is not common in most VMS and is ubiquitous in SEDEX (sedimentary exhalative) deposits, reflecting the diagenetic origin of most of the latter.

While the textures described above are striking and provide us with information regarding the earliest events at Greens Creek through possibly late diagenetic modifications to the ores, they represent only about 30 percent of the deposit and are skewed heavily toward features in pyritic ores. Most of the deposit shows the effects of Cretaceous metamorphism and polyphase deformation that was destructive to primary ore textures. In general, sulfide textures in the metamorphosed ores are characterized by cataclasis, annealing recrystallization, pressure solution, and solution creep that are consistent with lower greenschist facies dynamic metamorphism (Cox, 1987; Gilligan and Marshall, 1987; Marshall and Gilligan, 1987). Intramineral translocation and diffusional features such as dislocation glide, kinking, twinning, nabbarro-herring creep, and coble creep, indicative of deformation at higher metamorphic grades, are absent or have not been observed. None of the various etching techniques useful for elucidating such textures were used during the course of this study.

As previously mentioned, pyrite, due to its hardness, exhibits the greatest range of mineral textures. The most obvious and widespread pyrite texture that can be attributed to deformation of the deposit is the abundant instances of cataclasis exhibited by the more competent MFP ores. Especially where gangue silica content is high, large blocks of MFP have acted as deformation-resistant buttresses around which the softer ores and host rocks have flowed. When deformation does occur, it is usually manifested by brittle failure, resulting in a cataclastic breccia composed of angular, primary-textured pyrite clasts in a matrix of smaller pyrite fragments and ductile sulfides. In cases where deformation has shattered and transposed the MFP enough to impose a fabric, pyrite clasts of widely varying size become strung out in cataclastic trails. Clasts in these strings commonly exhibit pressure shadows filled with galena, tetrahedrite, chalcopyrite, and gangue minerals. In cases where the primary-textured fragments are precious metal enriched, pressure shadows can be occupied by native gold, electrum, pyrargyrite, and other exotic secondary silver minerals. Another brittle failure texture commonly seen in association with cataclastically deformed pyritic ores is intragranular extension microfractures in pyrite crystals that also become filled by secondary remobilized phases.

The other dominant texture present in pyrite as well as in base-metal sulfides is annealing recrystallization. As with the gradational development described above for the production of spongy pyrite, the annealing recrystallization produced a spectrum of textures. In incipient stages, the texture is characterized by inclusion-free areas in otherwise spongy-textured pyrite masses. Intermediate stages are characterized by masses of relatively clean, inclusion-free pyrite with subhedral grain boundaries. When other minerals are present, they occur within the clean pyrite as rounded, irregular inclusions or as fillings within extensional microfractures. We also have observed more advanced stages of framboid-derived atoll-shaped structures as described by England and Ostwald (1993). Relict rounded shapes within otherwise clean, monomineralic pyrite (figs. 6*B*, 10*E*) are common, as are euhedral-crystal-shaped sphalerite-, galena-, or tetrahedrite-filled growth zones (atolls) within subhedral to euhedral pyrite grains (figs. 6*J*, *K*; 10*D*, *G*). The presence of such textures in ores that show evidence of progressive metamorphism seems to confirm the suggestion of England and Ostwald (1993) that additional heat energy beyond that supplied during diagenesis is required to develop advanced atoll-shaped textures in sulfides. In their most advanced textural state, fully annealed pyritic ores exhibit the typical close-packed polygonal grain-boundary shapes (foam texture) commonly seen in higher grade metamorphosed massive sulfides. At this stage of deformation the pyritic ores are monomineralic with the exception of remobilized minerals that occupy late veinlets and extension microfractures (figs. 6*F*, 10*H*).

With the exception of the minor amounts of sphalerite, galena, tetrahedrite, and chalcopyrite that appear as bands, infillings, and matrix in the primary-textured ores, 95 percent of these minerals exhibit either recrystallization or remobilization textures. Of the base-metal sulfides, only sphalerite displays subhedral to euhedral crystal development, probably as a result of annealing recrystallization. When present, subhedral to euhedral crystals of sphalerite (fig. 6*L*, *M*) occur usually in a galena matrix or in a mixed base-metal-rich assemblage of annealed (?) sphalerite-galena-tetrahedrite-(pyrite). In extremely high grade zinc-rich MFBs (fig. 3*C*), nearly monomineralic aggregates of sphalerite have formed that exhibit rounded and bulging grain boundaries with anhedral galena. The prominence of recrystallization, as opposed to ductile flow, as a major process in Greens Creek ores is difficult to assess. The near universal absence of the characteristic triangular cleavage pits common to unstrained galena may be indicative of widespread recrystallization.

The complete absence of euhedral or even subhedral crystal shapes of tetrahedrite, chalcopyrite, and in most cases galena suggests that their occurrence in Greens Creek ores is largely the result of either physical (solid state) or chemical (fluid state) remobilization. The ubiquitous occurrence of these three minerals in extension microfractures and in pressure shadows of harder grains supports this contention. In well-banded MFBs it appears as though the primary means of mineral layer segregation is by ductile flow of the softer sulfides. Similarly, some fractures appear to have ductile sulfides injected into the open space. In such cases, quartz, dolomite, or other gangue minerals do not accompany the physically remobilized phases.

Instances of fluid-state remobilization over distances of millimeters to several meters are much more prevalent and easier to document. In such cases, grains of tetrahedrite, galena, chalcopyrite, and especially pyrargyrite and other exotic silver minerals clearly occupy veinlets (figs. 6*Q*, *R*; 5*A*) and veins that cut the massive ores. Fluid-state remobilization also appears to cause remobilization and concentration of free gold and electrum into late quartz veins and silica-flooded WSIs.

Overall, the process of metamorphic recrystallization and micro- to mesoscale remobilization of primary-textured ores has a visible (fig. 10*I*) as well as geochemical cleaning effect. As determined by LA–ICP–MS analyses, the relatively uniform low-level concentrations of trace elements in the primary-textured ores is consistent with redistribution of trace elements into predictable mineral phases based on free energy considerations. Specific trace elements are selectively partitioned into specific secondary mineral phases based on the size of the trace-element cations that are expelled from the trace-element-rich and poorly ordered primary ores into the appropriate-sized lattices of new phases. Thus, recrystallized sphalerite has high cadmium and mercury content but very low antimony and silver content, whereas remobilized tetrahedrite displays the opposite relationship. This metamorphic cleaning of primary ore and remobilization of metals into new mineral assemblages is a feature that has been documented at other massive sulfide deposits in metamorphic terranes (for example, the Sulitjelma deposit, Norway, Cook, 1996; nickel deposits of the Yilgarn craton, Australia, McQueen, 1987; Marshall and others, 2000).

Conclusions

The mineralogy, mineral textures, and mineral geochemical relationships at Greens Creek present the relatively unusual case of a trace-element-rich polymetallic massive sulfide deposit that has been subjected to partial metamorphic modification at low to moderate grade. The resulting array of textures spans the range from pristine primary features that provide insight into the genetic origins of the deposit through completely recrystallized and remobilized metamorphic features that provide an excellent opportunity to document the textural and chemical evolution of the deposit during its subsequent diagenetic and metamorphic history.

We believe that textures preserved in the primary ores exhibit an overwhelming preponderance of features attributable to formation of main-stage sulfide mineralization during early diagenesis of the accumulating hanging-wall sediments. These framboidal, colloform, and nodular pyrite textures also appear to preserve an early phase of coalescence and replacement, possibly enhanced by colloidal base-metal-sulfide gels, that marks the textural development of zone refinement in the growing sulfide accumulation. Subsequently, these same textures were modified to varying degrees by at least two periods of deformation related to the Cretaceous dynamic metamorphism that affected the region. This resulted in the continued development of more advanced atoll-shaped textures at the expense of polyframboid aggregates and spongy-textured pyrite. Progressive metamorphism of most of the ores resulted in recrystallization and remobilization of minerals and trace elements. The major effect of metamorphism was mineralogical cleaning of the ores resulting in redistribution and local upgrading of specific metals into predictable and more stoichiometrically ordered minerals.

References Cited

Binns, R.A., Scott, S.D., Bogdanov, Y.A., Lisitzin, A.P., Gordeev, V.V., Gurvich, E.G., Finlayson, E.J., Boyd, T., Dotter, L.E., Wheller, G.E., and Muravyev, K.G., 1993, Hydrothermal oxide and gold-rich sulfate deposits of Franklin Seamount, western Woodlark basin, Papua New Guinea: Economic Geology, v. 88, p. 2122–2153.

Blackburn, W.H., and Dennen, W.H., 1997, Encyclopedia of mineral names: The Canadian Mineralogist, Special Publication 1, 360 p.

Brew, D.A., Ford, A.B., and Himmelberg, G.R., 1989, Evolution of the western part of the Coast plutonic-metamorphic complex, southeastern Alaska, U.S.A.—A summary, *in* Daly, S.R., Cliff, R.A., and Yardley, B.W., eds., Evolution of metamorphic belts: London, Blackwell, Geological Society Special Publication 43, p. 447–451.

Brew, D.A., Himmelberg, G.R., Loney, R.A., and Ford, A.B., 1992, Distribution and characteristics of metamorphic belts in the southeastern Alaska part of the North American Cordillera: Journal of Metamorphic Geology, v. 10, p. 465–482.

Butler, I.B., and Nesbitt, R.W., 1999, Trace element distributions in the chalcopyrite wall of a black smoker chimney—Insights from laser ablation inductively coupled plasma mass spectrometry (LA–ICP–MS): Earth and Planetary Science Letters, v. 167, p. 335–345.

Chen, T.T., 1978, Colloform and framboidal pyrite from the Caribou deposit, New Brunswick: Canadian Mineralogist, v. 16, p. 9–15.

Cook, N.J., 1996, Mineralogy of the sulphide deposits at Sulitjelma, northern Norway: Ore Geology Reviews, v. 11, p. 303–338.

Cox, S.F., 1987, Flow mechanisms in sulphide minerals: Ore Geology Reviews, v. 2, p. 133–171.

Craig, J.R., and Vokes, F.M., 1992, Ore mineralogy of the Appalachian-Caledonian stratabound sulfide deposits: Ore Geology Reviews, v. 7, p. 77–123.

Croxford, N.J.W., and Jephcott, S., 1972, The McArthur River lead-zinc-silver deposit, NT, *in* Newcastle Conference 1972, Proceedings: Parkville, Victoria, Australasian Institute of Mining and Metallurgy, p. 1–27.

Duckworth, R.C., Knott, R., Fallick, A.E., Rickard, D., Murton, B.J., and Van Dover, C., 1995, Mineralogy and sulphur isotope geochemistry of the Broken Spur sulphides, 29°N, Mid-Atlantic Ridge, *in* Parson, L.M., Walker, C.L., and Dixon, D.R., eds., Hydrothermal vents and processes: Geological Society Special Publication no. 87, p. 175–189.

Dusel-Bacon, Cynthia, 1994, Metamorphic history of Alaska, *in* Plafker, G., and Berg, H.C., eds., The geology of Alaska: Boulder, Colorado, Geological Society of America, v. G1, p. 495–533.

Eldridge, S.E., Barton, P.B., Jr., and Ohmoto, H., 1983, Mineral textures and their bearing on formation of the Kuroko orebodies: Economic Geology Monograph 5, p. 241–281.

England, B.M., and Ostwald, J., 1993, Framboid-derived structures in some Tasman fold belt base-metal sulphide deposits, New South Wales, Australia: Ore Geology Reviews, v. 7, p. 381–412.

Gaspar, O.C., and Pinto, A., 1993, Neves-Corvo, a Kuroko type deposit in the Iberian Pyrite Belt: Resource Geology Special Issue, no. 17, p. 249–262.

Gilligan, L.B., and Marshall, B., 1987, Textural evidence for remobilization in metamorphic environments: Ore Geology Reviews, v. 2, p. 205–229.

Goldfarb, M.S., Converse, D.R., Holland, H.D., and Edmond, J.M., 1983, The genesis of hot springs deposits on the East Pacific Rise, 21ºN: Economic Geology Monograph 5, p. 184–197.

Graham, U.M., Bluth, G.J., and Ohmoto, H., 1988, Sulfide-sulfate chimneys on the East Pacific Rise, 11º and 13ºN latitudes, part I—Mineralogy and paragenesis: Canadian Mineralogist, v. 26, p. 487–504.

Guo, Xun, and Lichte, F.E., 1995, Analysis of rocks, soils, and sediments for the chalcophile elements by laser ablation–inductively coupled plasma mass spectrometry: Analyst, v. 120, p. 2707–2711.

Halbach, Peter, Pracejus, B., and Marten, A., 1993, Geology and mineralogy of massive sulfide ores from the central Okinawa trough, Japan: Economic Geology, v. 88, p. 2210–2225.

Hannington, M.D., Bleeker, W., and Kjarsgaard, I., 1999, Sulfide mineralogy, geochemistry, and ore genesis of the Kidd Creek deposit—Part I. North, Central, and South orebodies: Economic Geology Monograph 10, p. 163–224.

Hannington, M.D., Peter, J.M., and Scott, S.D., 1986, Gold in sea-floor polymetallic sulfide deposits: Economic Geology, v. 81, p. 1867–1883.

Hawksworth, M.A., and Meinert, L.D., 1990, Alteration and fluid inclusion study of the Groundhog mine vein system, Central mining district, New Mexico: Economic Geology, v. 85, p. 1825–1839.

Haymon, R.M., 1983, Growth history of hydrothermal black smoker chimneys: Nature, v. 301, p. 695–698.

Himmelberg, G.R., Brew, D.A., and Ford, A.B., 1994, Petrologic characterization of pelitic schists in the western metamorphic belt, Coast plutonic-metamorphic complex, near Juneau, southeastern Alaska: U.S. Geological Survey Bulletin 2074, 18 p.

Himmelberg, G.R., Brew, D.A., and Ford, A.B., 1995, Low-grade, M_1 metamorphism of the Douglas Island Volcanics, western metamorphic belt near Juneau, Alaska, *in* Schiffman, P., and Day, H.W., eds., Low-grade metamorphism of mafic rocks: Boulder, Colorado, Geological Society of America Special Paper 296, p. 51–66.

Huston, D.L., and Large, R.R., 1989, A chemical model for the concentration of gold in volcanogenic massive sulphide deposits: Ore Geology Reviews, v. 4, p. 171–200.

Juniper, S.K., Jonasson, I.R., Tunnicliffe, V., and Southward, A.J., 1992, Influence of a tube-building polychaete on hydrothermal chimney mineralization: Geology, v. 20, p. 895–898.

Knott, Richard, Fallick, A.E., Rickard, D., and Backer, H., 1995, Mineralogy and sulfur isotope characteristics of a massive sulfide boulder, Galapagos Rift, 58°55'W, *in* Parson, L.M., Walker, C.L., and Dixon, D.R., eds., Hydrothermal vents and processes: Geological Society Special Publication no. 87, p. 207–222.

Koski, R.A., Benninger, L.M., Zierenberg, R.A., and Jonasson, I.R., 1994, Chapter 16, Composition and growth history of hydrothermal deposits in Escanaba Trough, southern Gorda Ridge, *in* Morton, J.L., Zierenberg, R.A., and Reiss, C.A., eds., Geologic hydrothermal and biologic studies at Escanaba Trough, Gorda Ridge, offshore northern California: U.S. Geological Survey Bulletin 2022, p. 293–324.

Koski, R.A., Shanks, W.C. III, Bohrson, W.A., and Oscarson, R.L., 1988, The composition of massive sulfide deposits from the sediment-covered floor of Escanaba Trough, Gorda Ridge—Implications for depositional processes: Canadian Mineralogist, v. 26, p. 655–673.

Krasnov, S.G., Cherkashev, G.A., Stepanova, T.V., Batuyev, B.N., Krotov, A.G., Malin, B.V., Maslov, M.N., Markov, V.F., Poroshina, I.M., Samovarov, M.S., Ashadze, A.M., Lazareva, L.I., and Ermolayev, I.K., 1995, Detailed geological studies of hydrothermal fields in the North Atlantic, *in* Parson, L.M., Walker, C.L., and Dixon, D.R., eds., Hydrothermal vents and processes: Geological Society Special Publication no. 87, p. 43–64.

Large, Duncan, and Walcher, E., 1999, The Rammelsberg Cu-Zn-Pb-Ba deposit, Germany—An example of sediment-hosted, massive sulfide mineralization: Mineralium Deposita, v. 34, p. 522–538.

Large, R.R., Huston, D.L., McGoldrick, P.J., and Ruxton, P.A., 1989, Gold distribution and genesis in Australian volcanogenic massive sulfide deposits and their significance for gold transport models: Economic Geology Monograph 6, p. 520–536.

Larocque, A.C.L., and Hodgson, C.J., 1995, Effects of greenschist-facies metamorphism and related deformation on the Mobrun massive sulfide deposit, Quebec, Canada: Mineralium Deposita, v. 30, p. 439–448.

Lathram, E.H., Pomeroy, J.S., Berg, H.C., and Loney, R.A., 1965, Reconnaissance geology of Admiralty Island, Alaska: U.S. Geological Survey Bulletin 1181–R, 48 p.

Leach, D.L., and Sangster, D.F., 1993, Mississippi Valley-type lead-zinc deposits, *in* Kirkham, R.V., Sinclair, W.D., Thorpe, R.I., and Duke, J.M., eds., Mineral deposit modeling: Geological Association of Canada, Special Paper 40, p. 289–314.

Leitch, C.H.B., 1981, Mineralogy and textures of the Lahanos and Kizilkaya massive sulfide deposits, northeastern Turkey, and their similarity to Kuroko ores: Mineralium Deposita, v. 16, p. 241–257.

Loney, R.A., 1964, Stratigraphy and petrography of the Pybus-Gambier area, Admiralty Island, Alaska: U.S. Geological Survey Bulletin 1178, 103 p.

Ludden, J.N., Feng, R., Gauthier, G., Stix, J., Shi, L., Francis, D., Machado, N., and Wu, G., 1995, Applications of LAM–ICP–MS analysis to minerals: Canadian Mineralogist, v. 33, p. 419–434.

Marshall, Brian, and Gilligan, L.B., 1987, An introduction to remobilization—Information from ore-body geometry and experimental considerations: Ore Geology Reviews, v. 2, p. 87–131.

Marshall, Brian, Vokes, F.M., and Larocque, A.C.L., 2000, Chapter 2, Regional metamorphic remobilization—Upgrading and formation of ore deposits, *in* Spry, P.G., Marshall, B., and Vokes, F.M., eds., Metamorphosed and metamorphogenic ore deposits: Reviews in Economic Geology, v. 11, p. 19–38.

McClay, K.R., 1991, Deformation of stratiform Zn-Pb (-barite) deposits in the northern Canadian cordillera: Ore Geology Reviews, v. 6, p. 435–462.

McQueen, K.G., 1987, Deformation and remobilization in some western Australian nickel ores: Ore Geology Reviews, v. 2, p. 269–286.

Norman, M.D., Pearson, N.J., Sharma, A., and Griffin, W.L., 1996, Quantitative analysis of trace elements in geological materials by laser ablation ICPMS—Instrument operating conditions and calibration values of NIST glasses: Geostandards Newsletter, v. 20, p. 247–261.

Paradis, Suzanne, Jonasson, I.R., Le Cheminant, G.M., and Watkinson, D.H., 1988, Two zinc-rich chimneys from the Plume site, southern Juan de Fuca Ridge: Canadian Mineralogist, v. 26, p. 637–654.

Peter, J.M., and Scott, S.D., 1988, Mineralogy, composition, and fluid-inclusion microthermometry of seafloor hydrothermal deposits in the Southern Trough of Guaymas Basin, Gulf of California: Canadian Mineralogist, v. 26, p. 567–587.

Petersen, Sven, Herzig, P.M., and Hannington, M.D., 2000, Third dimension of a presently forming VMS deposit, TAG hydrothermal mound, mid-Atlantic ridge, 26°N: Mineralium Deposita, v. 35, p. 233–259.

Ridley, W.I., 2000, The ICP–MS laser microprobe—A new geochemical tool: Trends in Geochemistry, v. 1, p. 1–14.

Ridley, W.I., and Lichte, F.E., 1998, Chapter 11, Major, trace, and ultratrace element analysis by laser ablation ICP–MS, *in* McKibben, M.A., Shanks III, W.C., and Ridley, W.I., eds., Application of microanalytical techniques to understanding mineralizing processes: Reviews in Economic Geology, v. 7, p. 199–215.

Schouten, Cornelius, 1946, The role of sulphur bacteria in the formation of the so-called sedimentary copper ores and pyritic orebodies: Economic Geology, v. 41, p. 517–538.

Shibuya, E.K., Sarkis, J.E.S., Enzweiler, J., Jorge, A.P.S., and Figueiredo, A.G., 1998, Determination of platinum group elements and gold in geologic materials using an ultraviolet laser ablation high-resolution inductively coupled plasma mass spectrometric technique: Journal of Analytical Atomic Spectrometry, v. 13, p. 941–944.

Viets, J.G., Leach, D.L., Lichte, F.E., Hopkins, R.T., Gent, C.A., and Powell, J.W., 1996, Paragenetic and minor- and trace-element studies of Mississippi Valley-type ore deposits of the Cracow-Silesia district, southern Poland: Prace Panstwowego Instytutu Geologicznego, v. 154, p. 51–71.

Watling, R.J., Herbert, H.K., and Abell, I.D., 1995, The application of laser ablation–inductively coupled plasma–mass spectrometry (LA–ICP–MS) to the analysis of selected sulphide minerals: Chemical Geology, v. 124, p. 67–81.

Yui, Shunzo, 1983, Textures of some Japanese Besshi-type ores and their implications for Kuroko deposits: Economic Geology Monograph 5, p. 231–240.